



UNIVERSITÀ DEGLI STUDI DI MILANO
SCUOLA DI DOTTORATO
FISICA, ASTROFISICA E FISICA APPLICATA
CORSO DI DOTTORATO DI RICERCA IN
FISICA, ASTROFISICA E FISICA APPLICATA
CICLO XXVIII

Test of the isospin symmetry via Giant Dipole Resonance γ decay

Settore fisico disciplinare FIS/04

Tesi di Dottorato di:

Simone Ceruti

Coordinatore

Prof. Marco Bersanelli

Supervisore

Prof. Franco Camera

Academic year 2014-2015

Commission of the final examination:

External Referee: Prof. Nasser Kalantar

External Member: Prof. Muhsin Harakeh

Final examination:

Date 28/01/2016

Università degli Studi di Milano, Dipartimento di Fisica, Milano, Italy

a P

a B

Contents

1	Isospin symmetry in nuclear physics	5
1.1	Compound nucleus reaction	5
1.1.1	CN formation	6
1.1.2	CN decay	9
1.2	Giant Dipole Resonance	10
1.3	CN statistical GDR γ -decay	15
1.4	Isospin formalism	21
1.4.1	Charge invariance of nuclear interaction	22
1.4.2	mirror nuclei	23
1.5	isospin and electromagnetic transitions	23
1.6	Isospin mixing	26
1.6.1	Isospin Mixing in the ground state	27
1.6.2	Isospin mixing in the IAS	31
1.6.3	Isospin Mixing at low and high excitation energy	31
1.6.4	Isospin mixing parametrizations in compound nuclei	33
1.6.5	Isospin mixing temperature dependence	35
1.6.6	Isospin mixing: experimental methods and recent results	36
1.7	Isospin mixing beyond nuclear structure: The CKM matrix	40
1.8	isospin mixing: from finite to zero temperature	41

2	Experimental setup: description	45
2.1	The experiment	45
2.2	AGATA Demonstrator	46
2.2.1	AGATA geometry	47
2.2.2	Segmented detectors	48
2.2.3	Digital electronics and Pulse Shape Analysis (PSA)	50
2.2.4	Tracking algorithm	53
2.2.5	AGATA Demonstrator performances	55
2.3	LaBr ₃ :Ce	59
2.3.1	LaBr ₃ :Ce performances	60
2.4	Data AcQuisition (DAQ) system	64
2.4.1	Trigger conditions and event selection	65
3	Experimental setup: data analysis	69
3.1	AGATA Demonstrator	69
3.1.1	Time resolution	70
3.1.2	Energy resolution and linearity	72
3.2	HECTOR ⁺	77
3.2.1	Time resolution	77
3.2.2	Energy resolution and linearity	78
3.3	Multiplicity response	82
3.4	HECTOR ⁺ response function	87
4	Results and discussion I	89
4.1	Kinematics of reaction	89
4.2	CN particle decay	93
4.2.1	Neutron emission	93
4.2.2	Residues population	97
4.3	High-energy spectra	101
5	Results and discussion II	109
5.1	Isospin in the statistical model	109
5.2	Data analysis	110
5.3	Fit results	111
5.4	Coulomb spreading width Γ^\downarrow in ⁸⁰ Zr	116
5.5	Isospin mixing in ⁸⁰ Zr at T = 2 MeV	117

5.6	Isospin mixing in ^{80}Zr at $T=0$	119
5.7	δ_C in ^{80}Zr	122
	Conclusions and outlook	124
	A Papers	127
	Bibliography	129

Introduction

In Nature, symmetries help us to describe a complex physical system in a simple way and to better understand its behavior. Indeed, symmetries are strongly related to conservation laws which, in quantum mechanics, translate into good quantum number to describe the system. The search for symmetries is a fundamental goal in all fields in physics. At the same time, the possible breaking of a symmetry can open the gates for new and unexpected scenarios.

In a nuclear system many symmetries were identified. One of these is the *isospin symmetry*, which plays a key role in nuclear structure and nuclear reaction.

The isospin symmetry was introduced by Heisenberg in 1932 to describe the experimental evidence of the charge independence of the nuclear interaction. In the isospin formalism neutrons and protons are considered as different states of a unique particle, the nucleon, with a value of $1/2$ or $-1/2$ of the projection I_z of the isospin operator I .

A nucleus has a well defined value of $I_z = (N-Z)/2$, while I , according to quantum mechanics rules, can assume values ranging between $|(N-Z)|/2 \leq I \leq (N+Z)/2$. The nuclear ground state corresponds to the lower value of isospin $I = I_z$. Therefore, for self-conjugate nuclei the isospin ground state is $I = 0$.

This symmetry, which can be viewed as a rotational invariance in isospin space, implies that the nuclear Hamiltonian commutes with the total isospin operator I and thus the nuclear states can be labelled by the isospin quantum number. The isospin quantum number has an important role also in nuclear reaction, because it is a quantity which must be conserved. Indeed, reactions that do not conserve isospin are strongly inhibited.

In the atomic nuclei, the presence of the Coulomb interaction between protons breaks this symmetry and induces a mixing between nuclear states with different isospin values. In particular the stronger mixing is between states with a difference in isospin equal to one ($\Delta I = 1$). In this situation it is impossible to assign to a nuclear state a unique value of the isospin. This effect increases with the number of protons in the nucleus.

The knowledge of the isospin mixing is a fundamental quantity needed both to explain the properties of the isobaric analogue state (IAS) and for its connection with the test of the unitarity of the Cabibbo-Kobayashi-Maskawa matrix (CKM). In fact, the most precise value of the first term of the CKM matrix V_{ud} is extracted from the ft values of $0^+ \rightarrow 0^+$ super-allowed Fermi β decays with several small corrections. One of these corrections, called δ_C , depends on the isospin-mixing probability.

The breaking of isospin symmetry can be observed through decays which would be inhibited by selection rules. This is the case of the electric dipole transition (i.e. E1 transition) from self-conjugate nuclei in a $I=0$ configuration. To fully exploit this property, one should go in the region of the Giant Dipole Resonance (GDR), where most of the E1 strength is concentrated. This approach has been employed to measure the isospin mixing in nuclei at finite temperature T , formed in fusion evaporation reactions. In this type of experiments the use of self-conjugate projectile and target nuclei ensures the population of a compound nucleus (CN) with $I=0$. The hindrance of the GDR gamma decay can be measured and thus the mixing amplitude deduced. A partial restoration of the isospin symmetry is expected at high temperature due to the decreasing of CN lifetime for particle decay.

In the work of A. Corsi et al. [68], the isospin mixing was investigated at the $N = Z = 40$ value, namely in ^{80}Zr , at $T = 3$ MeV, while previous works concern CN with smaller $N = Z$ values only. This is the heaviest $N = Z$ nucleus that is possible to form using a fusion reaction with stable beam and target. The work on ^{80}Zr of Ref. [68] showed that by using the latest prediction of the isospin mixing value (based on EDF models [49]) together with the expression giving the T dependence of the isospin mixing [52], one finds a good agreement with the measured value at $T = 3$ MeV. This finding indicates that if one has an additional experimental point at another temperature one could deduce, from the combined analysis of the data, the value at $T = 0$ (with associated error bar). The additional point has to be at temperature lower than 3 MeV in order to check the predicted trend of the temperature dependence of the isospin mixing.

In this Thesis we report on a new study addressing the problem of isospin mixing in ^{80}Zr , for which, for the first time, the different residual nuclei were also measured. The

aim of the Thesis is to make a combined analysis of this new datum for isospin mixing at $T \approx 2$ MeV with the previous one at $T \approx 3$ MeV, in order to :

- test experimentally the trend of the temperature dependence of the isospin mixing;
- extract for the first time the value of the isospin mixing for $Z = 40$ at zero temperature;
- extract, for the first time, the isospin mixing correction δ_C necessary to obtain the correct ft value of super-allowed Fermi transitions.

The experiment was performed at the Laboratori Nazionali di Legnaro of the Istituto Nazionale di Fisica Nucleare (INFN, Italy) employing ion beams from the TANDEM accelerator complex. Two fusion reactions were used: one symmetric in target and projectile, forming the compound nucleus in the isospin $I=0$ channel, the other forming a very similar compound nucleus with $I \neq 0$, used in the analysis as reference. In particular, the used reactions are $^{40}\text{Ca} + ^{40}\text{Ca}$ at $E_{\text{beam}} = 136$ MeV ($I = 0$ channel) leading to the compound nucleus ^{80}Zr at $E^* = 54$ MeV and the $^{37}\text{Cl} + ^{44}\text{Ca}$ at $E_{\text{beam}} = 95$ MeV ($I \neq 0$ channel) leading to ^{81}Rb at $E^* = 54$ MeV.

Isospin symmetry in nuclear physics

In this chapter the main aspects concerning the isospin symmetry in nuclear physics are presented. In particular, the effects of the breaking of this symmetry and how they can be measured are described. Moreover, in order to have a clear dissertation of the physics case, a general overview about the fusion reaction process and the Giant Dipole Resonance is also reported.

1.1 Compound nucleus reaction

When two nuclear systems collapse forming a highly excited compound system, this process is called *Fusion Reaction*. The "new" nuclear system (the so-called *Compound Nucleus* (CN)) has too much excitation energy to be stable, but it lives sufficiently long for sharing its excitation energy uniformly among all its constituent nucleons (Fig.1.1 and all figures hereafter). The typical lifetime of the CN is greater than the orbital period of a nucleon, 10^{-22} . This requires that the mean free path of the projectile in the nucleus is much shorter than the nuclear radius. Later, the CN decays via particle emission (n, p, α or γ).

The foundations of the theory of compound nucleus reactions were laid by Niels Bohr in 1936 ([1,2]) and in next years by Bethe, Weisskopf and Ewing ([3–5]), which developed the evaporation theory. Later, Hauser and Feshbach ([6,7]) developed the quantum-mechanic formalism to describe the system.

Several review papers are present in the literature that describes the formal development of the compound nucleus theory ([8,9]). In this thesis, a brief description of the compound nucleus reaction is reported.

1.1.1 CN formation

The formation and the one-step decay of the compound nucleus can be written schematically as:



where R is the residual nucleus after the decay of the particle r .

The maximum excitation energy (E_{CN}^*), in the center of mass frame, given to the system by the fusion reaction is provided by the formula:

$$E_{CN}^* = E_{cm} + Q \quad (1.2)$$

where Q is the Q -value of the reaction, while E_{cm} is the kinetic energy in the center of mass of the incoming ion:

$$E_{cm} = E_{lab} \frac{M_t}{M_p + M_t} \quad (1.3)$$

E_{lab} is the kinetic energy in the laboratory frame of the projectile nucleus and M_p is its nuclear mass, while M_t is the nuclear mass of the target. E_{cm} must be larger than the repulsive interaction originated from the Coulomb interaction and the centrifugal potential:

$$E_{cm} > \frac{Z_1 Z_2 e^2}{R_c} + \frac{\hbar^2 j(j+1)}{2\mu R_c} \quad (1.4)$$

where Z_1 and Z_2 are the charge of the target and the projectile, R_c is the Coulomb barrier radius, j is the angular momentum of the system and μ is the reduced mass.

The energy sharing is so complete that the system decay is completely independent on its formation. This is the key assumption of the *Bohr-independence hypothesis*: the compound nucleus decay depends only on its excitation energy, angular momentum and parity, but not on how it is formed.

The CN is formed at high excitation energy and thus the energy distance between two levels becomes smaller than their decay width ($\Gamma \gg \Delta E$). In this situation, a microscopic discrete description of the nuclear states is no more convenient and it is useful to describe the CN using a continuum density of levels ρ . According to Bethe's Fermi-gas formula the level density can be written as:

$$\rho(E^*) \approx \frac{e^{2\sqrt{aE^*}}}{\sqrt{48E^*}} \quad (1.5)$$

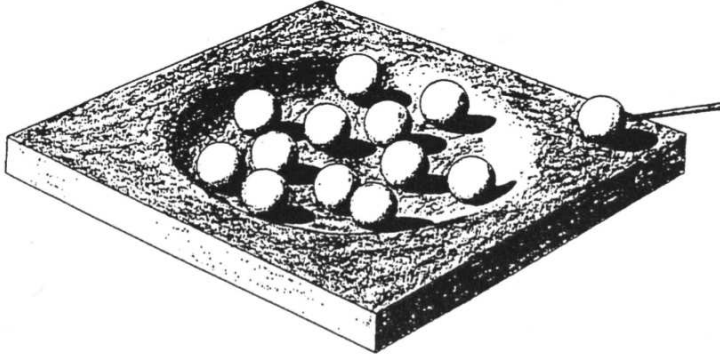


Figure 1.1: Famous picture which represents the Bohr's wooden toy model of the compound nucleus. The incident nucleon carries kinetic energy (as indicated by the billiard cue), collides with the nucleons in the target and shares its energy with many nucleons [1].

where a is the level density parameter $a = A/[7 - 10] \text{ MeV}^{-1}$ (see in Fig.1.2 the measured mass dependence [10]).

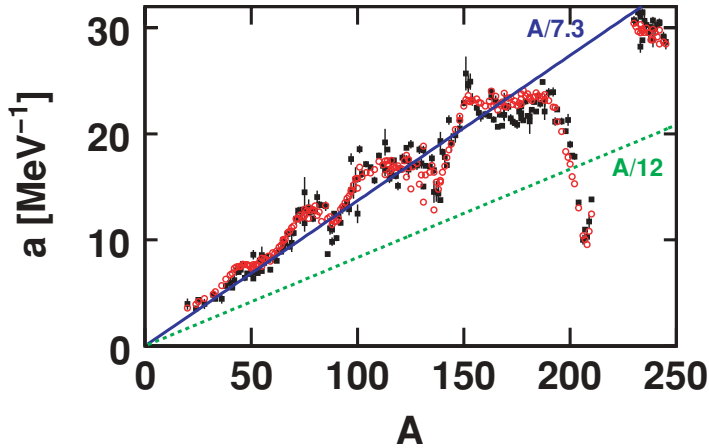


Figure 1.2: Mass dependence of level-density parameters. Experimental points from neutron-resonance experiments are shown as the solid square data points. The blue line is the linear interpolation of the data in comparison with another trend (green line). The red dots were obtained with a more sophisticated model taking into account shell effect for the single nucleus [10].

Thanks to the Bohr-independence hypothesis and the high density of states, the CN structure and decay can be described using a statistical approach: all the degrees of freedom of the system are in equilibrium and thus there is an equal probability distribution of all states with the same quantum number (momentum J , parity π) and excitation energy (E^*). In addition, the detailed balance is valid: the transition matrix element associated to the reaction $a + b \rightarrow CN$ is the same as the decay process $CN \rightarrow a + b$.

As reported in Ref. [11], the probability to find a nucleus in a state k at an energy E_k , momentum J_k and parity π_k can be defined as

$$p_k = \frac{\delta(E_k - E^*)\delta(J_k - J)\delta(\pi_k - \pi)}{\rho(E^*)} \quad (1.6)$$

where $\rho(E^*)$ is the density of states. This probability is called micro-canonical. The nuclear level density can be written using the entropy S of the system:

$$\rho = \rho_0 \exp(S(E^*)) \quad (1.7)$$

In analogy with a classical system in thermodynamical equilibrium, it is possible to introduce the concept of nuclear temperature:

$$T = \left(\frac{dS}{dE^*}\right)^{-1} = \left(\frac{1}{\rho} \frac{d\rho}{dE^*}\right)^{-1} \quad (1.8)$$

It is worth to note that in general, a statistical description of a physical system is allowed in the limit of a large number of particles which constitute the system. Therefore, the analogy between the nuclear system (particles ≈ 100) and a classic gas (particles $\approx 10^{23}$) could be considered too simple if not completely wrong. The reason of the success in the statistical description of the compound nucleus is the large number of states: as example, one obtains using Eq.1.5 for a nucleus with $A = 100$ and $E^* = 50$ MeV that there are 10^{17} states).

From Eq. 1.8 and Eq. 1.5 one can write the relation between T and E^* :

$$E^* = aT^2 \quad (1.9)$$

The Bohr independence hypothesis has implications that can be tested experimentally. It is possible, for instance, to form the same compound nucleus in different ways checking that the particles emitted are identical. The energy distributions of these particles can be calculated and compared with the experiment, as well as their angular distributions. In the continuum, the energy distributions are expected to have the Maxwellian

form (as in the classical gas) and the angular distributions are expected to be symmetric about 90° ([12,13]). Anyway, as the energy of the projectile increase, the hypothesis that the particle emission takes place after the statistical equilibrium is less valid. Indeed, there is an increasing likelihood that particles are emitted before the statistical equilibrium this is the pre-equilibrium process ([14,15]).

1.1.2 CN decay

The compound nucleus decay can be described successfully using the statistical approach proposed by Hauser and Feshbach ([6,7]), which takes into account explicitly the spin degree of freedom. The key assumption of this formalism is that all nuclear degrees of freedom have reached a statistical equilibrium before the cooling process. The compound nucleus fusion cross section σ_{fus} depends on the total angular momentum of the system (J):

$$\sigma_{fus}(J) = \sum_J \pi \lambda^2 \frac{2J+1}{1 + \exp(\frac{J-J_0}{d})} \quad (1.10)$$

The quantity J_0 is the angular momentum cut-off and it can be constrained from the fusion cross section. This is either measured, constrained from systematics, or obtained from the Bass model [16] with a good accuracy. d is the diffuseness and it can vary from 2 to $10 \hbar$.

The partial decay width of a CN of excitation energy E^* and spin J_{CN} for the evaporation of particle i is written as:

$$\Gamma_i(E^*, J_{CN}) = \frac{1}{2\pi \rho_{CN}(E^*, J_{CN})} \int d\epsilon \sum_{J_d=0}^{\infty} \sum_{|J_{CN}-J_d|}^{J_{CN}+J_d} \quad (1.11)$$

$$\sum_{l=|J-S_i|}^{J+S_i} T_l(\epsilon) \rho_d(E^* - B_i - \epsilon) \quad (1.12)$$

where J_d is the spin of the daughter nucleus; S_i , J , and l , are the spin, total, and orbital angular momenta of the evaporated particle; ϵ and B_i are its kinetic and separation energies; T_l is its transmission coefficient or barrier penetration factor; and ρ_d and ρ_{CN} are the level densities of the daughter and CN, respectively.

In the case of γ decay the transmission coefficient is calculated as ([17]):

$$T_l(E_\gamma) = \xi_l E_\gamma^{2l+1} \quad (1.13)$$

Where ξ is a constant value which can be estimated from the strengths of transitions between low-lying states in the mass region of interest or from the Weisskopf single-particle estimate.

The CN decay can be divided in two main phases. After the compound system formation, the excitation energy is higher than the nuclear binding energy (≈ 8 MeV) and hence the CN loses energy emitting particles. In general, the neutron emission is favourite because this particle does not have to cross the Coulomb barrier. In this phase, the neutron decay is in competition with high-energy γ -decay coming from the de-excitation of the Giant Resonances (typically with a branching ratio $\frac{P_\gamma}{P_n} \approx 10^{-3}$). In the second part of the CN decay the excitation energy is below the particle-emission threshold and thus the nucleus can decay only via quadrupole γ transitions along to the Yrast line (see the representation in Fig. 1.3).

1.2 Giant Dipole Resonance

The Giant Resonances (GR) are a nuclear excitation modes which played a key role in the study of nuclear structure for their connection with the bulk properties of the nuclear matter [18].

The IsoVector Giant Dipole Resonance (IVGDR), where protons oscillate against neutrons [19,20], is one of the more studied resonance in the past. Its centroid is related to the nuclear mass, while the width is related to different damping mechanisms [11,18].

The IVGDR can be observed in photo-absorption experiments using a gamma beam around 15 MeV. The photo-absorption cross section displayed clearly a resonant behaviour (see Fig.1.4) [21]. Because of the energy of the gamma projectile ($\hbar\omega_\gamma \approx 15$ MeV), the corresponding wavelength ($\lambda_\gamma \approx 100$ fm) is larger than nuclear radius ($R = 5 - 7$ fm). Therefore, the nucleus as a whole fill a constant electric field E . As a consequence protons move in the direction of E , while neutrons move in opposite direction to keep the center of mass at rest and to conserve momentum. On the other hand, The attractive nuclear force acts as a restoring force which reverses the motion of the neutrons and protons.

The shape obtained in these (γ,n) experiments can be well reproduced using a Lorentzian curve:

$$\sigma(E) = \frac{\sigma_0}{1 + [(E^2 - E_0^2)^2 / E^2 \Gamma^2]} \quad (1.14)$$

where E_0 and σ_0 are the position and the cross section of the centroid respectively, while Γ is the width of the distribution.

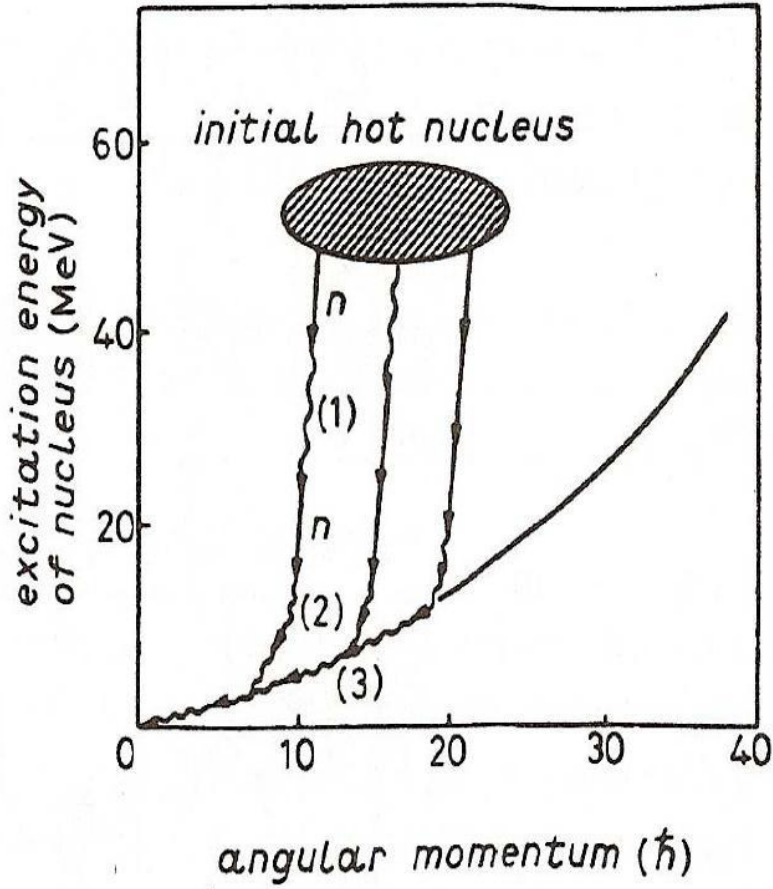


Figure 1.3: Schematic representation of the CN de-excitation. Giant Dipole Resonance radiation, indicated by (1), is emitted in competition with neutrons, indicated by n. (2) indicates the quadrupole γ ray emitted in final steps of the decay.

The excitation energy of the GDR (E_{GDR}) is , in the case of medium-heavy nuclei, well described by the formula:

$$E_{GDR} = 31.2A^{-1/3} + 20.6A^{-1/6} \text{ MeV} \quad (1.15)$$

where A is the nucleus mass number.

The integrated strength of the GDR (S_{GDR}) can be estimated using the classic Thomas-Reiche-Kuhn energy-weighted sum rule:

$$S_{GDR} = \int_{E_{min}}^{E_{max}} \sigma_{\gamma}^{abs} dE = \frac{60NZ}{A} \text{ MeV mb} \quad (1.16)$$

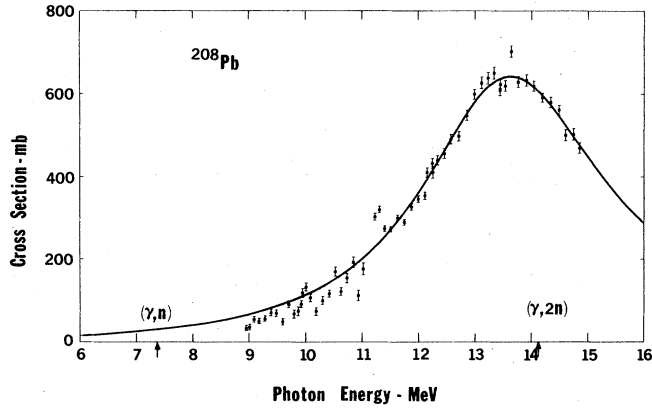


Figure 1.4: photo-neutron cross section for the nucleus ^{208}Pb [21].

IVGDR state exhausts 100% of the energy weighted sum rule for a electric dipole operator and, in general, the IVGDR γ decay is characterized by the emission of an electric dipole photon.

The width of the resonance (Γ_{GDR}) in the nuclear ground state can be described microscopically as a sum of two contributes

$$\Gamma_{GDR} = \Gamma^{\uparrow} + \Gamma^{\downarrow} \quad (1.17)$$

where Γ^{\uparrow} is the escape width of particle evaporation while Γ^{\downarrow} is the spreading width arising from the coupling with $2p-2h, 3p-3h, \dots$ configurations. The latter term is the larger contribution to the GDR width. Γ_{GDR} can vary from about 4 to 8 MeV. The narrowest width is observed in double magic nuclei. For nuclei with a stable axial deformation, the photo-neutron cross section is split in two parts, corresponding to a IVGDR vibration along or perpendicular to the symmetry axis (see Fig. 1.6) [22].

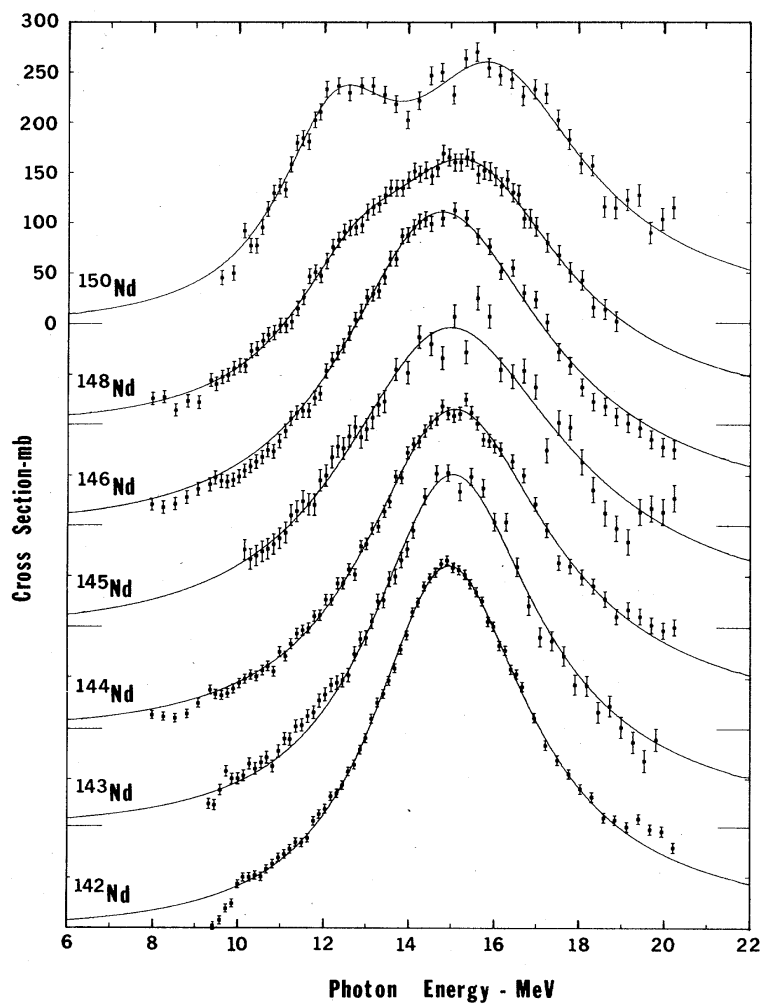


Figure 1.5: photo neutron cross section for the isotopic chain of Nd [21].

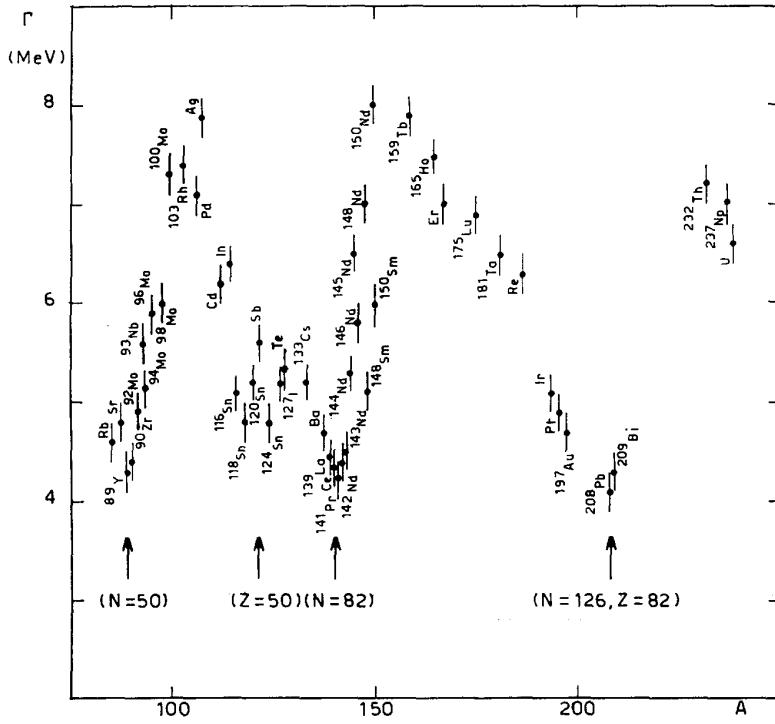


Figure 1.6: Width of the IVGDR along to the mass number A [22].

1.3 CN statistical GDR γ -decay

In 1951 David Brik suggested that a giant resonance state can be built on each nuclear state and the properties of a such resonance do not depend on microscopic structure of the nucleus but only on its bulk properties. This is the so-called the *Brink-Axel hypothesis* [23, 24]. As a consequence, in a compound nucleus in thermal equilibrium there is a nonzero probability to have populated an IVGDR built on an excited state, which can decay emitting an electric dipole γ ray (i.e. E1). The first experimental evidence of a IVGDR in excited state was found in 1981 by Newton et al. [25]; indeed, they found a change in the slope of the intensity curve in the region of the resonance energy (between 10 - 20 MeV) (see Fig.1.7).

Following the idea of Bring and Axel, the GDR was investigate intensely in the past years in hot compound nuclei (CN) at different excitation energy (E^*), angular momentum (J) and temperature (T) [11, 26–29]. It was found that, although the centroid is rather constant with the nucleus excitation energy, the width increases with both temperature and angular momentum. The main reason is the increase of the average deformation of the nucleus because of the thermal shape fluctuations and angular momentum (see Fig.1.9) [30, 31].

As explained before, the statistical description of CN decay is based on the assumption that all the degrees of freedom have reached statistical equilibrium before the cooling process (decay) and that the detailed balance is valid. Assuming the Axel-Brink hypothesis, one can write the γ -decay width Γ_γ as

$$\frac{d\Gamma_\gamma(E_\gamma)}{dE_\gamma} \sim \frac{\rho(E^* = E_{fin})}{\rho(E^* = E_{in})} \sigma_{abs}(E_\gamma) = \sigma_{abs}(E_\gamma) \exp(-E_\gamma/T) \quad (1.18)$$

where σ_{abs} is the absorption cross section at $T = 0$, which has the Lorentzian shape of Eq.1.14. If the excitation energy is above the neutron separation energy, the GDR γ -decay is in competition with the neutron emissions. Typically the ratio between the γ decay and the neutron decay is $\approx 10^{-3}$. Since the CN in thermal equilibrium, the neutron emission cross section can be parametrized using a Maxwell-Boltzman distribution:

$$\sigma_n \approx T^2 \exp(E_n - B_n)/T \approx T^2 \exp(-B_n/T) \quad (1.19)$$

where B_n is the neutron binding energy. The ratio between Γ_n and Γ_γ is:

$$\frac{\Gamma_\gamma}{\Gamma_n} \propto \exp((E_n - E_\gamma)/T) \quad (1.20)$$

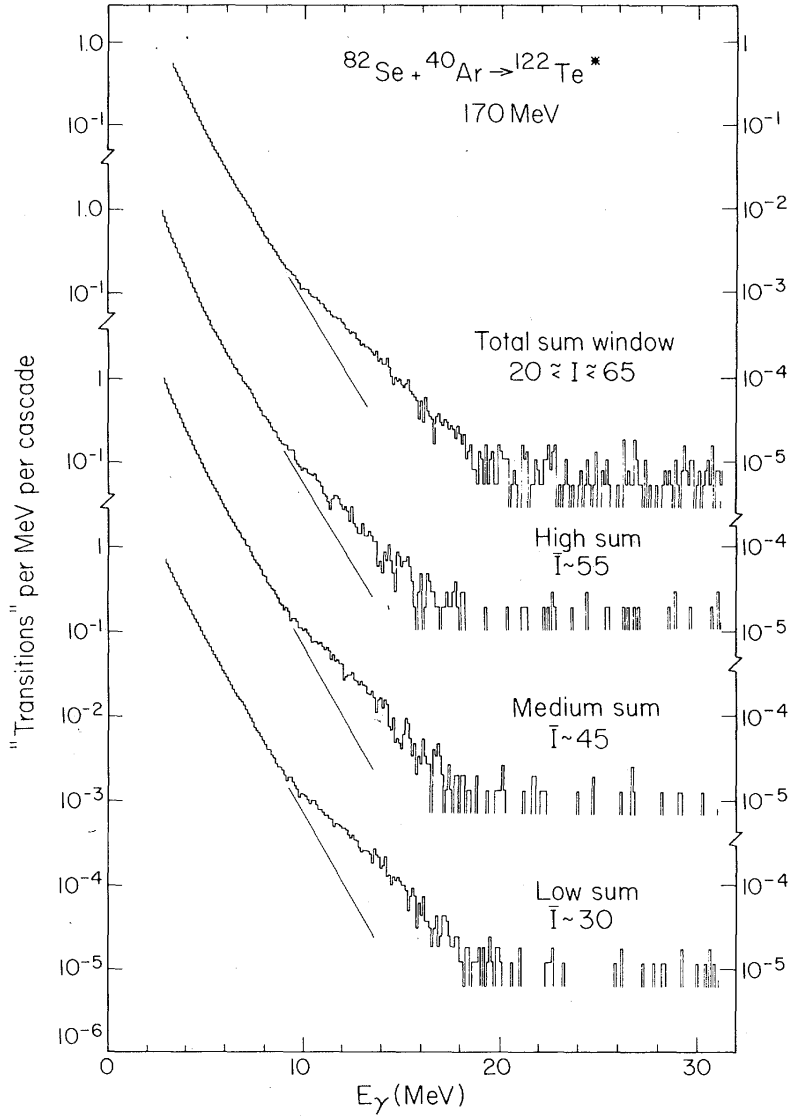


Figure 1.7: γ -rat spectra measured for different angular momentum in the fusion reaction $^{82}\text{Se} + ^{40}\text{Ar} \rightarrow ^{122}\text{Te}^*$. It is clearly visible the resonance structure for energy above 10 MeV [25].

where E_n is the total energy carry out by a neutron (kinetic energy plus binding energy). Since E_n is approximately equal to $2T$, the probability for the emission of a γ ray with $E_\gamma > B_n + 2T$ increases with T (see Eq.1.20). As consequence, the high energy γ -ray of the IVGDR is emitted preferably at high temperature and thus in the first-step decay. On the other hand, for $E_\gamma < B_n + 2T$ the γ -decay probability increases as T decreases. Consequently the γ rays are emitted in the end of the cascade decay. The

different contributions to the total γ -ray spectrum at different temperature are shown in Fig.1.8.

The total width Γ of the GDR built on a CN is sensitively larger than the one obtained in a photo-absorption experiment and it increases with the nuclear temperature [32] and the Angular momentum (J) [31,33].

This observation is not in contrast with the Brink-Axel hypothesis, indeed the increase of the width can be explained with the fact that the nucleus experiences a continuous range of deformations and space orientations as described by the Thermal Fluctuation Model (TFM). Each deformation is parametrized using the coordinates (β, γ) and the probability to found the nucleus is a certain deformation is:

$$P(\beta, \gamma) \sim \exp(-F(T, \beta, \gamma)/T) \quad (1.21)$$

where F is the free energy of the system. the resulting GDR strength function is a weighted superposition of many Lorentzian distributions associated to a deformation:

$$\sigma(E) = \int \sum_{k=1}^3 \sigma_k(E, \beta, \gamma) P(T, \beta, \gamma) \beta^4 |\sin(3\gamma)| d\beta d\gamma \quad (1.22)$$

Studying the thermal effects, one finds that the β_{eq} , corresponding to the minimum of the total free energy, can be sensitively different to the average value $\langle \beta(J, T, A) \rangle$, defined as:

$$\langle \beta(J, T, A) \rangle \approx \int \beta P(T, \beta, \gamma) \beta^4 |\sin(3\gamma)| d\beta d\gamma \sin \theta \quad (1.23)$$

A linear relation between the average nuclear deformation $\langle \beta(J, T, A) \rangle$ and the increase of the FWHM of the Lorentzian distribution used to reproduce the GDR spectrum has been proposed in [33] and plotted in Fig.1.9.

In addition, with increasing angular momentum, the nucleus tends to undergo oblate flattening due to centrifugal effects. the equilibrium deformation, β_{eq} , increases rapidly with angular momentum, and as a consequence, the total GDR strength function undergoes a further splitting, which increases the FWHM.

Studying the available experimental data Kusnezov et al. [31] obtained a phenomenological formula to describe the global dependence of the GDR width on temperature, spin, and mass:

$$\begin{aligned}\Gamma(T, J, A) &= \Gamma(T, J=0, A) \left[L\left(\frac{J}{A^{5/6}}\right) \right]^{4/[(T/T_0) + 3]} \\ \Gamma(T, J=0, A) &= \Gamma_0(A) + c(A) \ln(1 + T/T_0)\end{aligned}\quad (1.24)$$

where Γ_0 is usually extracted from the measured ground state GDR, $T_0 = 1$ MeV, $c(A) \approx 6.45 - A/100$ and the function $L(\xi = \frac{J}{A^{5/6}})$ can be written as $L(\xi) = 1 + 1.8[1 + e^{(1.3-\xi)/0.2}]^{-1}$. In Fig. 1.10 the comparison between experimental data and theoretical calculation is shown [31].

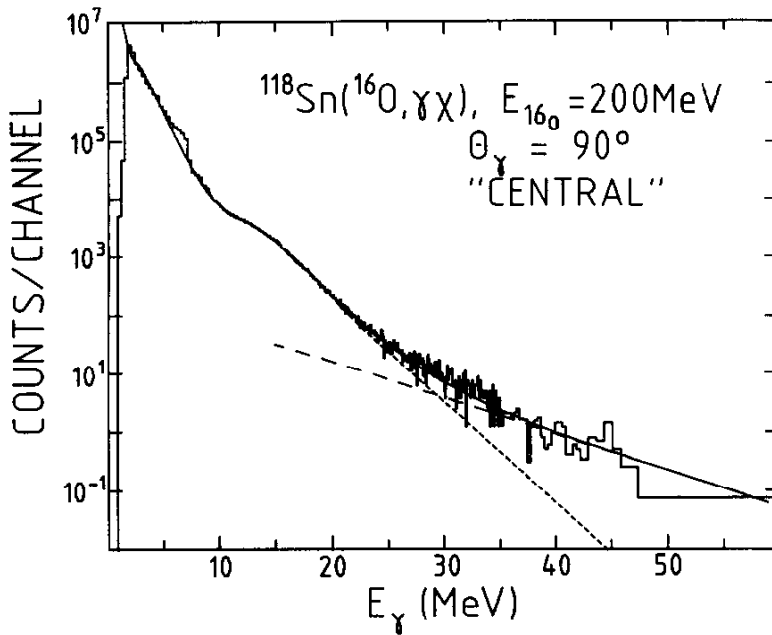


Figure 1.8: typical γ -ray spectrum obtained from a fusion evaporation reaction ($^{16}\text{O} + ^{118}\text{Sn}$) [34]. The full line is a fit to the data, the dashed line is the bremsstrahlung contribution while the dotted line is the CN decay.

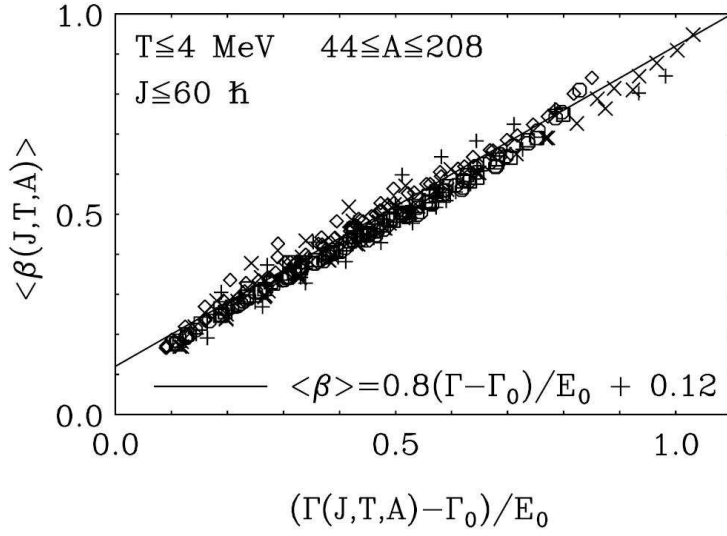


Figure 1.9: Linear relation between average nuclear deformation $\langle \beta(J, T, A) \rangle$ and GDR width $\Gamma(J, T, A)$ (continuous line) [31].

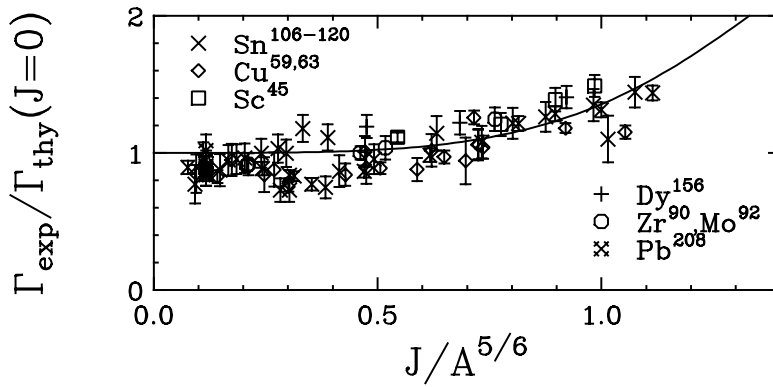


Figure 1.10: Angular momentum dependence of the GDR width. The line is the theoretical calculation obtained using Eq. 1.25. Taken from Ref. [31]

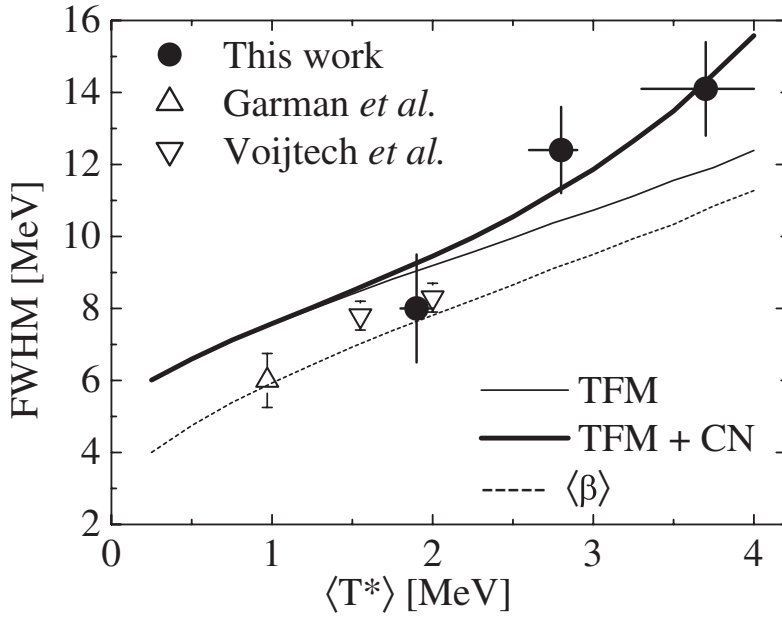


Figure 1.11: Comparison between measured and calculated GDR widths as a function of the effective nuclear temperature T . The data are taken at $J = 45 \hbar$ (filled dots), $J = 8-16 \hbar$ (up-pointing triangle), $J = 23-27 \hbar$ (down-pointing triangle). The thin (thick) continuous line shows TFM calculations without (with) CN decay width, while the dashed line shows the average deformation $\langle \beta \rangle$ calculated with TFM. Taken from [32].

1.4 Isospin formalism

In Nature, symmetries help us to describe a complex physical system in a simple way and to understand better its behaviour. Indeed, symmetries are strongly related to conservation laws which, in quantum mechanics, translate into good quantum number to describe the system. Therefore, the search for a symmetry it is a fundamental goal in all fields in physics. At the same time, the study of the breaking of a symmetry is very important because it can open the gates for new and unexpected scenarios.

In a nuclear system many symmetries are identified. One of these is the *isospin symmetry*, which plays a key role in nuclear structure and nuclear nuclear reaction.

The isospin symmetry was introduced by Heisenberg in 1932 [37] to describe the identical behaviour of neutrons and protons in a nuclear field. It means that neutrons and protons can be considered as different quantum states of the same particle, the *nucleon*. The Heisenberg's idea was born from the observation that in nucleus does not exist only the protons ($m_p = 938.272 \text{ MeV}/c^2$), but also another no-charge particle, the neutron, with a very similar mass ($m_n = 939.566 \text{ MeV}/c^2$). The isospin symmetry implies the charge invariance of the nuclear interaction.

A new coordinate is needed to distinguish neutrons and protons, the *isospin* (or *isobaric spin*) I [38], which was formally introduced in analogy with the spin (this is the reason of the similar name). A nucleon has isospin $I = 1/2$, the two nucleons are labelled with the third component I_3 of the isospin operator:

$$|p\rangle \equiv |I = \frac{1}{2}, I_3 = +\frac{1}{2}\rangle \quad |n\rangle \equiv |I = \frac{1}{2}, I_3 = -\frac{1}{2}\rangle \quad (1.25)$$

A similar case is the situation of two particles with different spin projection m_s : in absence of a magnetic field \mathbf{B} they have the same energy, but if \mathbf{B} is present they exhibit different energy depending on the orientation of m_s .

The concept of isospin can be extended to the nucleus as a whole: the total isospin is the sum of the single nucleon contribution:

$$I = \sum_{i=1}^A I(i) \quad (1.26)$$

where A is the mass number of the nucleus. Also the charge operator Q can be expressed using the isospin quantum number:

$$Q = e(1/2 - I_0) \quad (1.27)$$

1.4.1 Charge invariance of nuclear interaction

The assumption that the attractive nuclear force is independent of the charge of the individual nucleons (or equivalently that the isospin symmetry exists) can be divided in two separated ideas: i) The first idea is that the nuclear interaction is charge symmetric, which requires that the interaction between neutron-neutron (nn) and proton-proton (pp, neglecting the Coulomb interaction effect) is the same; ii) the second idea is that the nuclear interaction is charge independent, which means that not only nn and pp interactions are equal, but also np interaction.

As any assumption in physics, it important to test experimentally these ideas. A very powerful test for studying the nature of the nuclear interaction is a low-energy scattering experiment between different pairs of nucleons (nn,pp,np). The scattering length obtained are reported in the Table.1.1. the values related to pp scattering were corrected by Coulomb interaction effect. The data are similar, but not compatible between each others. The differences can be interpreted as a charge not symmetric and not independent component of the nuclear interaction. Many theoretical works were made to describe this difference ([39–41] and the references therein). For instance, the difference between nn(pp) and np scattering length can be explained partially with the presence of an "exchange" process, which is impossible to distinguish from the direct process [?]. Of course, the difference in mass between n and p ($\Delta M \approx 2$ MeV [42] neutron is about 0.14% heavier) is one of the origin of the charge-independence breaking.

It is worth to be noted that these data are related to a free-nucleon interaction and not to a effective-nuclear interaction in nuclear medium. Although, these symmetries are weakly broken, in the nuclear behaviour the isospin symmetry can be considered a good "approximated" symmetry [43,44].

	a [fm]	r[fm]
pp	-17.3 ± 0.4	2.794 ± 0.015
nn	-18.9 ± 0.4	2.84 ± 0.03
np	-23.74 ± 0.02	2.73 ± 0.03

Table 1.1: Scattering length (a) and effective range (r) obtained in low-energy scattering experiment. the pp values were corrected by taking into account the Coulomb interaction effect. Data taken from Ref. [41].

1.4.2 mirror nuclei

Formally, In the isospin space charge independence of the nuclear force implies that the nuclear Hamiltonian H commutes with the third component of the isospin operator:

$$[H, \mathbf{I}_0] = 0 \quad (1.28)$$

and also with the square of the isospin operator:

$$[H, \mathbf{I}^2] = 0 \quad (1.29)$$

Therefore the nuclear wave-function does not change if one replaces a neutron by protons or vice versa. A clear indication of the presence of the isospin symmetry in nuclear medium is the comparison of the level schemes of two *mirror* nuclei [44,45]. These nuclei are characterized for having the same number of mass A , but with the number of neutrons and protons exchanges. Therefore, within the isospin formalism these two nuclei are completely identical. For instance, the partial level scheme of ^{67}Se ($N = 33, Z = 34$) and ^{67}As ($N = 34, Z = 33$) are shown in Fig.1.12. The spectra, as well as the properties of various states, are very similar to each other and this is an evidence of the charge independence of nuclear force. The differences between the corresponding levels of the two spectra may be attributed to the Coulomb interaction [46,47](the so-called Coulomb Energy Distance, CED).

1.5 isospin and electromagnetic transitions

The isospin is not a physical observable which can be measured in an experiment. Thus, if one wants to test the isospin invariance, it important to find an observable sensitive to the isospin. The Electromagnetic transition is an example.

Starting from the Fermi's golden rule and following Ref. [48], it is possible to write the width of an electromagnetic transition between two nuclear states a and b :

$$\Gamma_\gamma(L) = 8\pi k \sum_{M, M_b} |\langle J_b M_b; I_b I_{3b} | H(L, M) | J_a M_a; I_a I_{3a} \rangle|^2 \quad (1.30)$$

where H is the general electromagnetic Hamiltonian defined as:

$$H(L, M) = \frac{1}{c} \int \mathbf{j}_N(\mathbf{r}) \cdot \mathbf{A}_{LM}^*(\mathbf{r}) d\tau \quad (1.31)$$

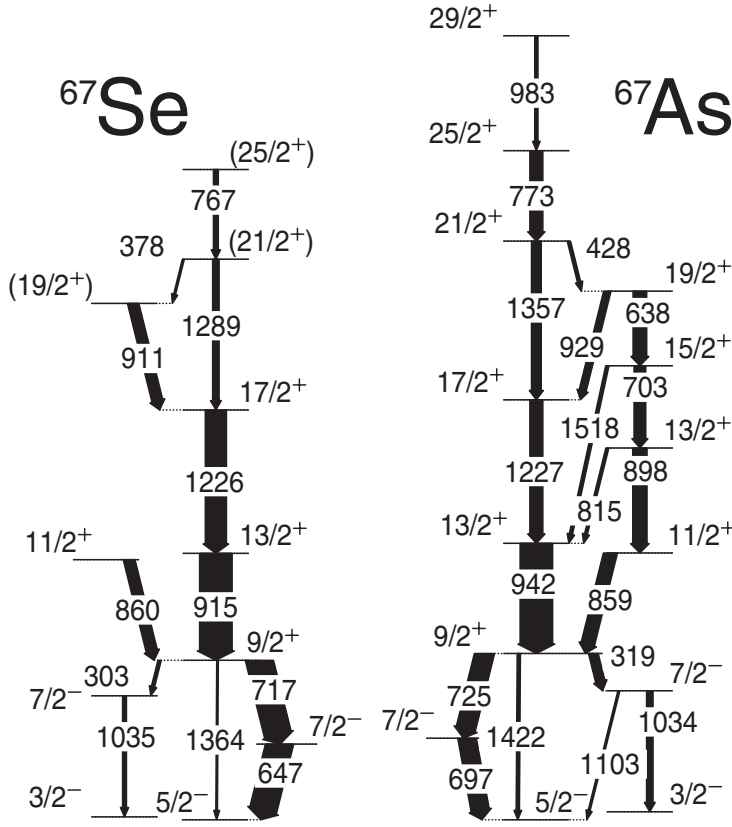


Figure 1.12: Partial level schemes for (left) ^{67}Se and (right) ^{67}As determined from the experimental data. The energy labels are given in keV and the widths of the arrows are proportional to the relative intensities of the γ rays. [45]

\mathbf{j}_N and \mathbf{A}_{LM}^* are the the nuclear current density and the electromagnetic vector potential respectively. \mathbf{j}_N can be expressed in the isospin formalism as:

$$\mathbf{j}_N(\mathbf{r}) = \frac{1}{2}e \sum_j (1 - 2I_3^{(j)}) \left[\frac{\mathbf{p}_j}{2M_p} \delta(\mathbf{r} - \mathbf{r}_j) + \delta(\mathbf{r} - \mathbf{r}_j) \frac{\mathbf{p}_j}{2M_p} \right] \quad (1.32)$$

$$+ \frac{1}{2}c \left(\frac{e\hbar}{2M_p c} \right) \sum_j [\mu_+ + \mu_- 2I_3^{(j)}] \nabla \times \boldsymbol{\sigma}_j \delta(\mathbf{r} - \mathbf{r}_j) \quad (1.33)$$

where $\mu_+ = \mu_n + \mu_p$ and $\mu_- = \mu_n - \mu_p$ (μ_n and μ_p are the neutron and proton nuclear magnetic moments. According the isospin dependence, Eq. 1.33 can be divided in two terms: an isoscalar term \mathbf{j}_N^0 , independent of I_3 , and an isovector term, linearly dependent on I_3 .

$$\mathbf{j}_N^0(\mathbf{r}) = \frac{1}{2}e \sum_j \left[\frac{\mathbf{P}_j}{2M_p} \delta(\mathbf{r} - \mathbf{r}_j) + \delta(\mathbf{r} - \mathbf{r}_j) \frac{\mathbf{P}_j}{2M_p} \right] \quad (1.34)$$

$$+ \frac{1}{2}c\mu_+ \left(\frac{e\hbar}{2M_p c} \right) \sum_j \nabla \times \boldsymbol{\sigma}_j \delta(\mathbf{r} - \mathbf{r}_j) \quad (1.35)$$

$$\mathbf{j}_N^1(\mathbf{r}) = -\frac{1}{2}e \sum_j 2I_3^{(j)} \left[\frac{\mathbf{P}_j}{2M_p} \delta(\mathbf{r} - \mathbf{r}_j) + \delta(\mathbf{r} - \mathbf{r}_j) \frac{\mathbf{P}_j}{2M_p} \right] \quad (1.36)$$

$$+ \frac{1}{2}c\mu_- \left(\frac{e\hbar}{2M_p c} \right) \sum_j 2I_3^{(j)} \nabla \times \boldsymbol{\sigma}_j \delta(\mathbf{r} - \mathbf{r}_j) \quad (1.37)$$

As a consequence, even the Hamiltonian in Eq. 1.30 can be splitted in two parts $H = H^0 + H^1$, where H^0 is the isoscalar interaction and H^1 the isovector interaction. In order to understand the isospin properties of an electromagnetic transition, it is useful at this point to rewrite Eq. 1.30 extracting the I_3 dependence with the Wigner-Eckhart theorem. This implies:

$$\langle J_b M_b; I_b I_{3b} | H_0 + H_1 | J_a M_a; I_a I_{3a} \rangle = \quad (1.38)$$

$$= (-1)^{I_b - I_{3b}} \begin{pmatrix} I_b & 0 & I_a \\ -I_{3b} & 0 & I_{3a} \end{pmatrix} \langle J_b M_b; I_b | H_0 | J_a M_a; I_a \rangle \quad (1.39)$$

$$+ (-1)^{I_b - I_{3b}} \begin{pmatrix} I_b & 1 & I_a \\ -I_{3b} & 0 & I_{3a} \end{pmatrix} \langle J_b M_b; I_b | H_1 | J_a M_a; I_a \rangle \quad (1.40)$$

From Eq. 1.40 one can easily observe that both isoscalar and isovector interaction do not vanish only if $I_{3b} = I_{3a}$. This is the first isospin selection rule: $\Delta I_3 = 0$. Physically, this means that an electromagnetic transition cannot occur between different nuclei (as expected).

From the Wigner coefficients in Eq. 1.40 it is possible to deduce another selection rule. For the isoscalar part of the Eq. 1.40 the coefficient is equal to:

$$(-1)^{I_b - I_{3b}} \begin{pmatrix} I_b & 0 & I_a \\ -I_{3b} & 0 & I_{3a} \end{pmatrix} = (2I_a + 1)^{-1/2} \delta_{I_b I_a} \quad (1.41)$$

This implies that the isoscalar part vanishes except if $I_a = I_b$. For the isovector term, where $I_b = I_a + 1$ ($I_b = I_a - 1, I_a, I_a + 1$) the Wigner coefficient is equal to:

$$(-1)^{I_b - I_{3b}} \begin{pmatrix} I_b & 1 & I_a \\ -I_{3b} & 0 & I_{3a} \end{pmatrix} = (-1)^{I_b - I_a} \left[\frac{I_a^2 - I_3^2}{I_+ (2I_+ - 1)(2I_+ + 1)} \right]^{1/2} \quad (1.42)$$

where $I_> = \max(I_a, I_a)$. From Eq.1.44 it is possible to deduce an important rule: if $I_3 = 0$ (self conjugate nuclei) transition the isovector $\Delta I = 0$ contribution vanishes. As we will see later this fact plays an important role in E1 transition.

In the long wave approximation ($k_\gamma r \ll 1$) all terms of order $(k_\gamma r)^2$ and higher are neglected. In this situation the electric dipole operator (E1) can be simply written using the isospin formalism as:

$$H(L=1, M) \simeq \sum_j^A q_j r_j \simeq \sum_j^A \left(\frac{1}{2} - I_{3j}\right) \mathbf{r}_j = \frac{1}{2} \sum_j^A \mathbf{r}_j - \sum_j^A I_{3j} \mathbf{r}_j \quad (1.43)$$

$$= H^{I=0}(L=1, M) + H^{I=1}(L=1, M) \quad (1.44)$$

The isoscalar term $H^{I=0}$ is proportional to the center of mass coordinates ($R_{CM} = \sum_j \mathbf{r}_j$ and thus cannot induce any nuclear excitation: the matrix element of such operator vanishes). Therefore in the long-wave approximation the E1 operator is totally isovector.

The fact that E1 operator does not have any isoscalar contribution provides an important rule: a $\Delta I = 0$ E1 transition in self-conjugate nuclei is forbidden. Only $\Delta I = 1$ transition occurs. As consequence the total E1 strength is reduced.

As explained in the previous paragraph the γ decay of the GDR has an E1 character. Thus in self-conjugate nucleus the γ decay is strongly inhibited. It is worth noting that only the first step of the γ decay is inhibited. In fact, after a proton or a neutron evaporation (which is the favourite decay) a self-conjugate nucleus is no more in a $I_3 = 0$ state and thus also isovector $\Delta I = 1$ transition can occur.

1.6 Isospin mixing

The isospin symmetry was introduced neglecting in the Hamiltonian the Coulomb interaction between protons. This was reasonable because the latter is, in general, much weaker than nuclear interaction.

Nevertheless, considering the nucleus as a whole, the short-range nuclear interaction increases linearly with the number of nucleons, while the Coulomb interaction, which has a long range effect, increases quadratically with the number of protons. Consequently, the effect of Coulomb interaction becomes significant in medium-heavy proton-rich nuclei and the total interaction in the nucleus is no more charge independent, hence the isospin symmetry is broken.

To understand the effects of the Coulomb interaction in the microscopic structure of the nucleus is useful to write it in the isospin formalism:

$$V_C = \sum_{k < j} e^2 \frac{(1/2 - I_{3k})(1/2 - I_{3j})}{r_{jk}} \quad (1.45)$$

that can be decomposed in three terms in isospin space: isoscalar ($V_C^{(0)}$), isovector ($V_C^{(1)}$), isotensor ($V_C^{(2)}$):

$$\begin{aligned} V_C^{(0)} &= \sum_{k < j} \frac{1}{4} \frac{e^2}{r_{jk}} \left[1 + \frac{4}{3} \mathbf{I}^{(j)} \cdot \mathbf{I}^{(k)} \right] \\ V_C^{(1)} &= - \sum_{k < j} \frac{1}{2} \frac{e^2}{r_{jk}} [I_3^{(j)} + I_3^{(k)}] \\ V_C^{(2)} &= \sum_{k < j} \frac{1}{4} \frac{e^2}{r_{jk}} \left[4 I_3^{(j)} I_3^{(k)} - \frac{4}{3} \mathbf{I}^{(j)} \cdot \mathbf{I}^{(k)} \right] \end{aligned} \quad (1.46)$$

The isoscalar part has no relevant effects and it can be added to the isoscalar nuclear interaction. On the other hand, the isovector and isotensor part lead to isospin impurities in the wave function with $\Delta I = 1$ and $\Delta I = 2$ respectively. These impurities are responsible to the breaking of isospin symmetry. This is the so-called *isospin mixing*.

1.6.1 Isospin Mixing in the ground state

Since the Coulomb interaction remain smaller than the nuclear interaction the isospin mixing can be treated using a perturbative approach. For a nucleus in a $I = 0$ state the probability to have a $I = 1$ impurity α^2 is:

$$\alpha^2 = \sum_{I=1} \frac{|\langle I=1 | V_C^{(1)} | I=0 \rangle|^2}{(E_{I=0} - E_{I=1})^2} \quad (1.47)$$

and the ground state (*g.s.*) is a linear combination between the two isospin states.

$$|g.s.\rangle = \beta |0\rangle + \alpha |1\rangle \quad (1.48)$$

Two points are worth to be noted in Eq. 1.47: i) Because of the denominator in the formula the isospin mixing probability is important only between states close together in energy; ii) The Coulomb potential varies slowly in the nucleus (considered it as a

charged sphere) and it preserves spin and parity, so the Coulomb interaction lead to large mixing between states with the same J^π .

In brief, the isospin mixing is large only between nearby states having the same spin and parity and a large overlap between their spatial wave functions. The tensor part induce a mixing with $\Delta I = 2$ states. These states lye much higher in energy than $\Delta I = 1$ states and thus the mixing contribution of these states is smaller (due to the denominator of Eq. 1.47). For this reason the tensor part is neglected.

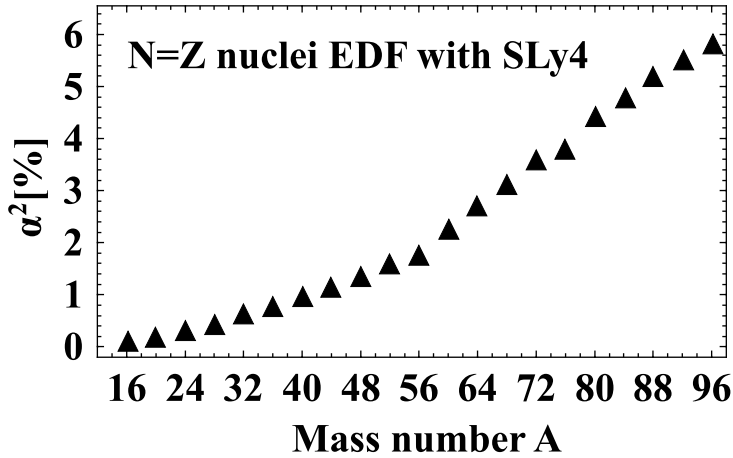


Figure 1.13: Degree of mixing α^2 in the ground states for $N = Z$ nuclei, obtained using an Energy Density Functional approach and a SLy4 nuclear interaction [49].

The knowledge of the degree of mixing in the *g.s.* gives a direct information about how much the isospin is a good quantum number for the system.

Particular effort has been made during the years to deduce, in the best possible way, the value of isospin mixing for proton-rich nuclei and the mass dependence of α^2 [49–55].

This was encouraged by the possibility to reach very exotic nuclei in the proton-rich zone of the nuclear chart, where the isospin mixing is expected to be large and not negligible. This is the case of ^{100}Sn , which is the heaviest $N = Z$ nucleus existing in the nuclear chart where the α^2 is largest.

In the past years many theoretical calculations of the isospin mixing in the ground state were performed using several approaches. In Fig.1.13 the isospin mixing mass dependence using an Energy Density Functional (EDF) approach is shown [49]. As expected, the α^2 value increases with the mass number, since the Coulomb interaction increases.

In Tab.1.2 different theoretical calculations of the isospin mxing in ^{80}Zr are given.

The values differ for the method (second column) and the effective interaction (third column) used in the calculations. the values vary between 1 - 4.5%. In Fig.1.14 each value corresponds to a different nuclear interaction used in the EDF calculations.

α^2	method	interaction	Ref.
1	analytic		[103]
3.6	HF+TDA	SG2	[54]
3.1	HF+TDA	SIII	[54]
3	HF spherical	SIII	[55]
2.5	HF deformed	SIII	[55]
3.9	HF	SIII	[53]
2.2	analytic		[53]
4.5	EDF	SLy4	[49]

Table 1.2: Available theoretical calculations of α^2 for ^{80}Zr are reported from the references listed in the last column. HF stands for Hartree-Fock, EDF for Energy Density Functionals, TDA for Tamm-Dancoff approximation. In the third column the parametrization of Skyrme interaction used is given only for non-analytic approaches.

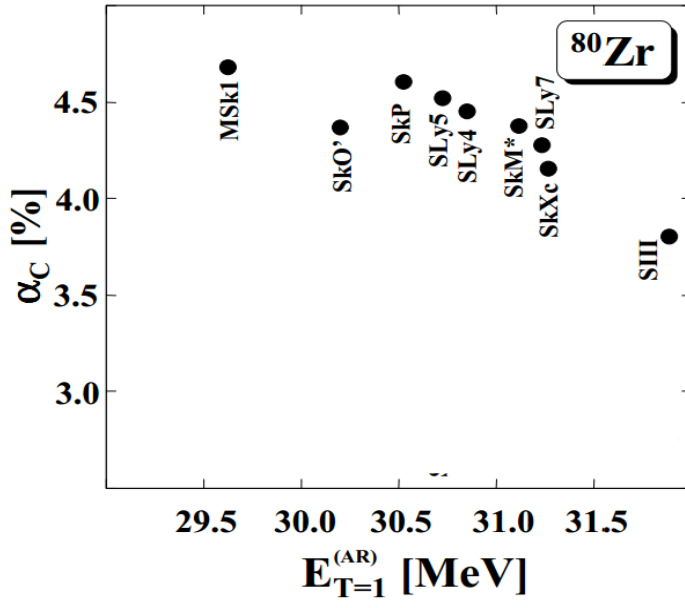


Figure 1.14: Degree of mixing in ^{80}Zr using an EDF approach with different parametrizations of the nuclear interaction [49].

1.6.2 Isospin mixing in the IAS

The Isobaric Analogue State (IAS) is a particular excited state of the nucleus, obtained exchanging a neutron with a proton. The parent nucleus $|\pi\rangle$ and the $|IAS\rangle$ have the same isospin [46]. As a consequence, this state preserves the the parent nucleus wave function and thus it has the same internal structure. This is true despite the fact that the IAS lies at higher excitation energy ~ 15 MeV due to the larger Coulomb interaction energy. Since the excitation energy of the IAS is above the particle separation energy, the IAS can decay via proton or neutron decay and thus it exhibit a width Γ (see Fig.1.15 for a schematic representation), wich can be written as:

$$\Gamma = \Gamma^\uparrow + \Gamma^\downarrow \quad (1.49)$$

The Γ^\uparrow quantity is the sum for all partial particle decay width and it is dominated by the allowed proton decay. The Γ^\downarrow quantity is the spreading width of the IAS which is dominated by the isospin-forbidden neutron decay. This quantity is generated by the isospin mixing with the IsoVector Monopole State and it is of particular interest because it is a way to study the Coulomb interaction effects in the nuclear medium [56–58]. The value of the spreading width is expected to increase with the number of protons in the nucleus because of the increase of the Coulomb interaction. This idea was confirmed by many experimental results (see Fig.1.16 and Fig.1.16).

In the mass region nearby ^{80}Zr , the Coulomb spreading width of the IAS was measured in the nucleus ^{80}Se , obtaining $\Gamma_{IAS}^\downarrow = 9.9 \pm 0.6$ keV [57].

1.6.3 Isospin Mixing at low and high excitation energy

As the excitation energy increases the levels lie close together. Using Eq.1.47, α^2 increases as the level spacing ΔE decreases. At the same time, the states acquire a finite particle decay width, as the excitation energy exceed the particle binding energy.

The Eq.1.47 is no more valid in this situation and it must be replaced with:

$$\alpha^2 = \sum_{I=1} \frac{|\langle I=1 | V_C^{(1)} | I=0 \rangle|^2}{((E_{I=0} + i\Gamma/2_{I=0}) - (E_{I=1} + i\Gamma/2_{I=1}))^2} \quad (1.50)$$

Γ is the decay width of the level. When the decay width of the levels is almost equal to their energy distance the mixing probability is maximum.

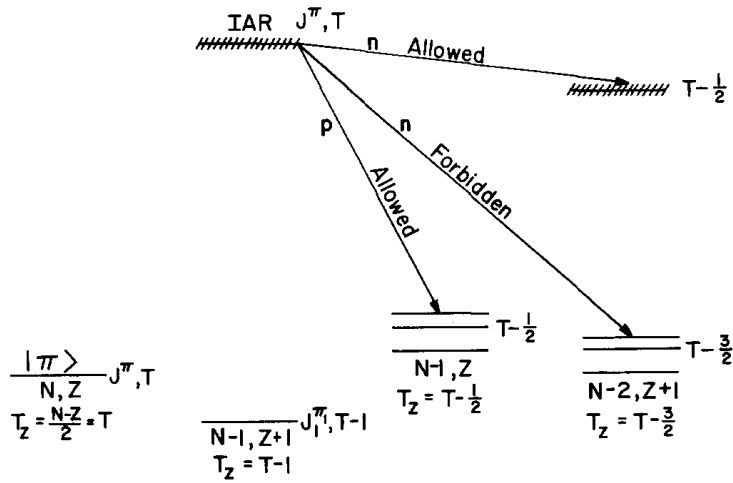


Figure 1.15: Schematic representation of the IAS particle decay. The allowed and forbidden decays are shown [46].

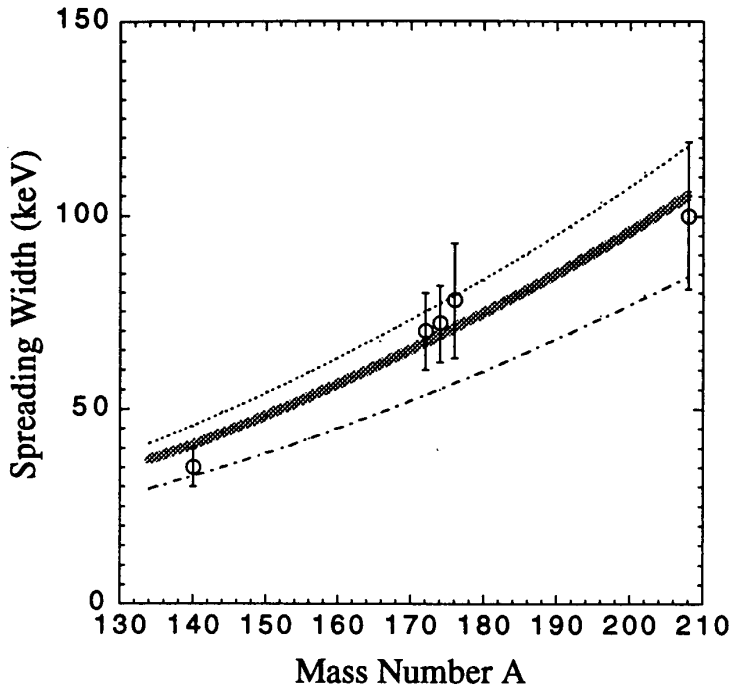


Figure 1.16: Experimental IAS spreading widths (circles) compared with theoretical calculations (lines) [58].

Wilkinson [59] and Morinaga [60] first suggested that at high excitation energy the nuclear decay width becomes so large to overwhelm the Coulomb interaction effects and restore the isospin symmetry.

This process can be viewed in a time-dependent approach where the compound nucleus is formed and it decays before the time necessary to mix the states. The mixing probability is determined by the competition between the nuclear lifetime and the Coulomb interaction time scale. The time-independent description of the isospin mixing in Eq.1.50 is no more suitable to describe this dynamical mechanism.

To understand better this point is useful to introduce a picket-fence model, which describes the dynamical competition between two effects (see Ref. [103] [62]).

Suppose to have a set of $I = 0$ levels with the same energy distance D . A state with $I = 1$ lies at an energy $E_{I=1}$ between two $I = 0$ states and a perturbation apply to the system. The perturbation connects the state with $I = 1$ with the underlie $I = 0$ states and it has a constant matrix element v . In the limit $v \ll D$, the probability to have $I = 1$ configuration per unit energy interval is given by the Breit-Wigner distribution:

$$P_{I=1}[E] = \frac{1}{2\pi} \frac{\Gamma^\downarrow}{(E_{I=1} - E)^2 + (\Gamma^\downarrow/2)^2}$$

$$\Gamma^\downarrow = \frac{2\pi v^2}{D} \quad (1.51)$$

where Γ^\downarrow is the spreading width of the $I = 1$ state. Suppose now to analyse the problem in a time dependent approach, considering that at $t = 0$ only the $I = 0$ state is populated. The probability to find the system at $I = 1$ is:

$$P(t, I = 1) = \exp\left[-\frac{\Gamma^\downarrow}{2}t - \frac{i}{\hbar}E_{I=1}t\right]^2 \quad (1.52)$$

The state $I = 1$ decay (mix) to $I = 0$ state with an exponential decay time equal to Γ^\downarrow/\hbar and this process is in competition with the natural decay of the state. In the case of isospin mixing problem Γ^\downarrow is the Coulomb spreading width associated to the Coulomb interaction time scale: if the decay width becomes much larger than the Coulomb spreading width (hence the decay is faster than the Coulomb interaction) no isospin impurities affect the decay. The isospin symmetry is restored.

1.6.4 Isospin mixing parametrizations in compound nuclei

Harney, Ritcher and Weidenmüller [61] proposed a coherent isospin mixing description in the compound nucleus, which took into account both the isospin mixing formalism

and the CN statistical behaviour.

The model, which used the S-matrix formalism, assumes no mixing in the entrance channel, before the formation of the compound nucleus. On the other hand after the CN formation isospin mixing is allowed between two classes of states $I_{<} = I_z$ and $I_{>} = I_z + 1$. The Coulomb spreading width $\Gamma_{>}^{\downarrow}$ for the state $I_{>}$ is expressed as:

$$\Gamma_{>}^{\downarrow} = 2\pi \overline{|\langle I_{<} | H_C | I_{<} \rangle|^2 \rho[I_{<}]} \quad (1.53)$$

where the Coulomb matrix element is averaged over all possible states. This model assume that the two states are centred at the same excitation energy, therefore the Coulomb matrix element is the same also for $I_{<}$ states, so that

$$\Gamma_{>}^{\downarrow} = \frac{\rho[I_{<}]}{\rho[I_{>}]}\Gamma_{<}^{\downarrow} \quad (1.54)$$

Harney, Ritcher and Weidenmüller write the isospin mixing term using a single parameter z , that is given by:

$$\begin{aligned} z &= 4\pi^2 \overline{H_C^2} \rho[T_{<}] \rho[T_{>}] = \\ &= 2\pi \Gamma_{>}^{\downarrow} \rho[T_{>}] = \\ &= 2\pi \Gamma_{<}^{\downarrow} \rho[T_{<}] \end{aligned} \quad (1.55)$$

using this equation, it is possible to derive the fraction $\alpha_{>}^2$ of states $I_{>}$ which mix with $I_{<}$ states.

$$\alpha_{>}^2 = \frac{\Gamma_{>}^{\downarrow}/\Gamma_{>}}{1 + \Gamma_{>}^{\downarrow}/\Gamma_{>} + \Gamma_{<}^{\downarrow}/\Gamma_{<}} \quad (1.56)$$

and similarly the fraction $\alpha_{<}^2$ of states $I_{<}$ which mix with $I_{>}$ states.

$$\alpha_{<}^2 = \frac{\Gamma_{<}^{\downarrow}/\Gamma_{<}}{1 + \Gamma_{<}^{\downarrow}/\Gamma_{<} + \Gamma_{>}^{\downarrow}/\Gamma_{>}} \quad (1.57)$$

where $\Gamma_{>(<)}$ is the total decay width of the states $I_{>(<)}$. For small mixing the Eq. 1.57 is reduced to $\Gamma_{<}^{\downarrow}/\Gamma_{<} = \tau_{CN}/\tau_{mix}$ and confirms the Wilkinson's hypothesis that the mixing at finite excitation energy depends only on the competition between the mixing and the CN decay. For intermediate value of the mixing it is necessary include the terms in the denominator $\Gamma_{<(>)}^{\downarrow}/\Gamma_{<(>)}$, which take into account also the probability that $I_{<(>)}$ states mix back to $I_{>(<)}$

Many theoretical works proposed the idea that the $\Gamma_{\downarrow}^{\downarrow}$ obtained in a statistical reaction could be the same as the spreading width measured with the IAS. The reason is that both quantities are originated by the isospin mixing effects with the IsoVector Monopole State. This idea was supported by many experimental results, as shown in Fig.5.5.

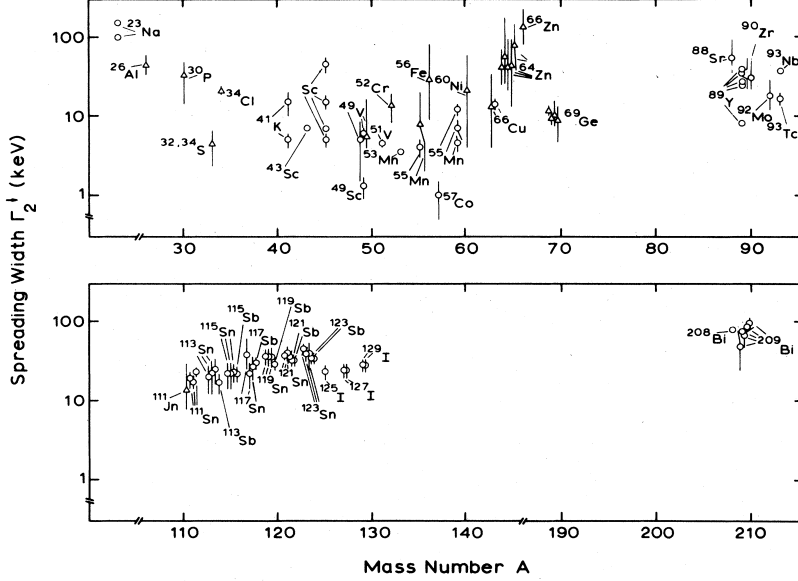


Figure 1.17: Experimental spreading width obtained from the IAS (circles) and statistical reactions (triangles) [61].

1.6.5 Isospin mixing temperature dependence

The problem of the isospin symmetry restoration at high excitation energy was treated by Sagawa, Colò and Bortignon [52] using a microscopic model. The model is based on the Feshbach projection method and provide the isospin mixing temperature dependence through its relation with the spreading width of the IAS. Indeed, the authors assume that the Coulomb spreading width of a CN it is the same of the corresponding IAS, because both are originated by the isospin mixing.

The coulomb spreading width of the IAS can be expressed as:

$$\Gamma_{IAS}^{\downarrow} = (\Gamma_C^{\uparrow}(E^*) + \Gamma_M(E^*)\alpha_{T_0+1}^2(T_0 + 1)) \quad (1.58)$$

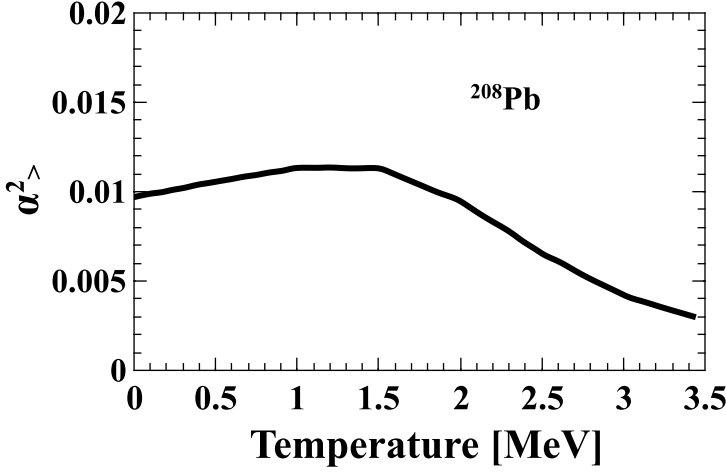


Figure 1.18: Degree of mixing α^2 in the nucleus ^{208}Pb as a function of nuclear temperature [52].

and thus the mixing probability α^2 is given by

$$\alpha_{T_0+1}^2 = \frac{1}{T_0 + 1} \frac{\Gamma_{IAS}^\downarrow}{\Gamma_C^\uparrow(E^*) + \Gamma_M(E_{IAS})} \quad (1.59)$$

where $\Gamma_C^\uparrow(E^*)$ is the compound nucleus decay width, Γ_{IAS}^\downarrow is the Coulomb spreading width of the IAS, Γ_M is the width of the Isovector Monopole Resonance (IVM) at the excitation energy of the IAS. The latter quantity it is impossible to measure experimentally and it can be considered as a parameter of the model.

$\Gamma_C^\uparrow(E^*)$ increases exponentially with the temperature ($\Gamma_{CN} \approx e^{-\Delta E/T}$, ΔE is the energy removed by the emitted particle) while the other two quantities are expected to remain constant with temperature. Nevertheless, the authors introduce a smooth linear dependence of the Γ_{IAS}^\downarrow obtaining for ^{208}Pb the trend reported in Fig.1.18. The mixing probability remains rather constant with the nuclear temperature and then decreases sharply because of the short lifetime of the nucleus.

1.6.6 Isospin mixing: experimental methods and recent results

Isospin mixing amplitude can be measured experimentally studying transitions which would be forbidden if isospin is a good quantum number. This is the case of a E1 γ decay in $N = Z$ nuclei [63–68] or a β decay in nuclei with different isospin [69]. Both transition are forbidden in the hypothesis of pure isospin states. The analysis reported in this thesis is based on the first method.

Since the E1 strength is almost exhausted by the Giant Dipole Resonance [11], this resonant state is the best state if one wants to test E1 properties as the isospin mixing. The best way to excite the GDR state in a $I = 0$ configuration is using a fusion reaction with a $N = Z$ beam and target combination. Using the formalism proposed by Harney, Richter and Weidenmüller in the statistical model used to fit the data, one can extract the isospin mixing amplitude at a certain value of excitation energy (or equivalently temperature), giving also an estimation of the Coulomb spreading width.

In principle, comparing experimental data at different excitation energy one can give a proof of Wilkinson's suggestion.

The GDR γ -decay was used for the first time by M. Harakeh [65] as test of the isospin symmetry (see Fig.1.19). In the past years the Washington University group and the Warsaw group performed experiments with the goal to verify the Wilkinson's suggestion and see clearly the isospin symmetry restoration at high temperature [64,66]. In the work of A. Corsi and Milano group [68], the isospin mixing was investigated at the $Z = N = 40$ value, namely in ^{80}Zr , at an excitation energy $E^* = 84$ MeV. In that work the Coulomb spreading width was found to be $\Gamma^\downarrow = 10 \pm 3$ keV and the mixing probability $\alpha^2 = 5\% \pm 1\%$ (see Fig.1.20).

As shown in Fig.1.21, all these experimental data show the expected mass and temperature dependence. Anyway, the validity of this comparison is limited by the errors bars and by the fact that these data are related to different nuclei in mass and in temperature. A systematic study of the same nucleus at different temperature does not exist in literature.

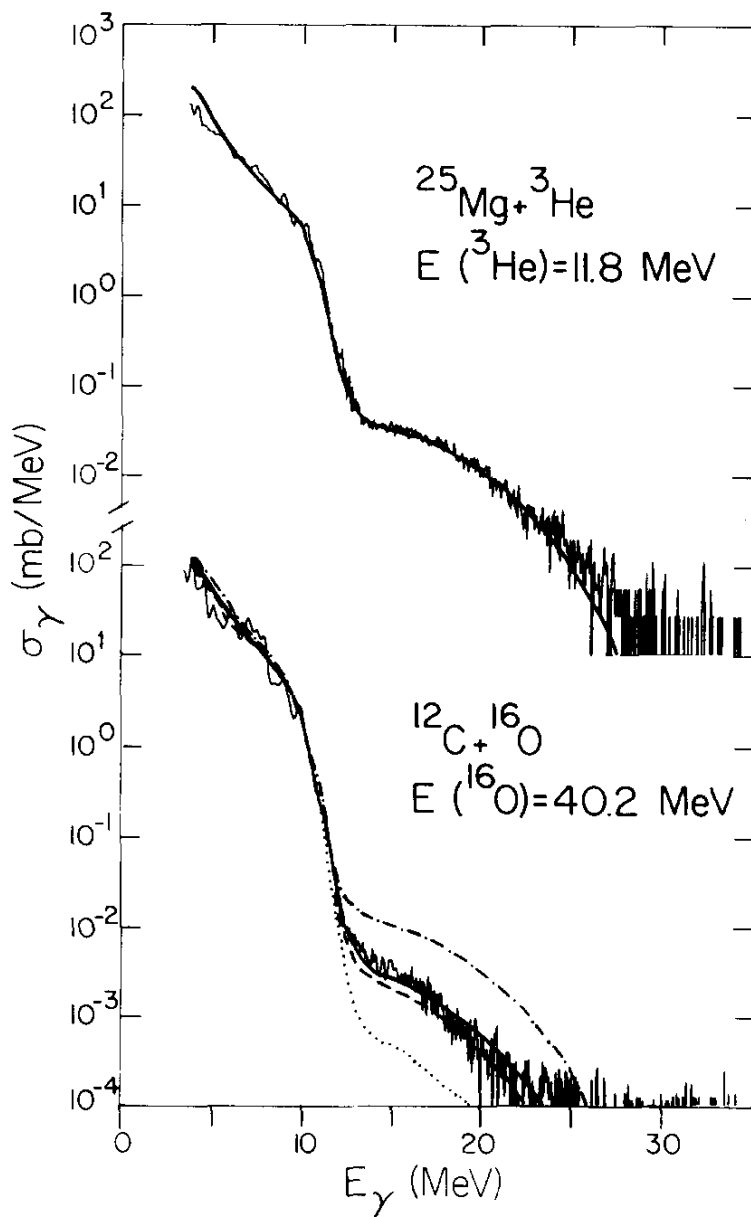


Figure 1.19: γ -ray spectra for the reactions $^{25}\text{Mg} + ^3\text{He}$ ($I \neq 0$) and $^{12}\text{C} + ^{16}\text{O}$ ($I = 0$). In the latter spectrum the effect of the isospin mixing is shown. Dot-dashed curve: full mixing. Dot curve: no mixing. Dashed curve: best fitting curve [65].

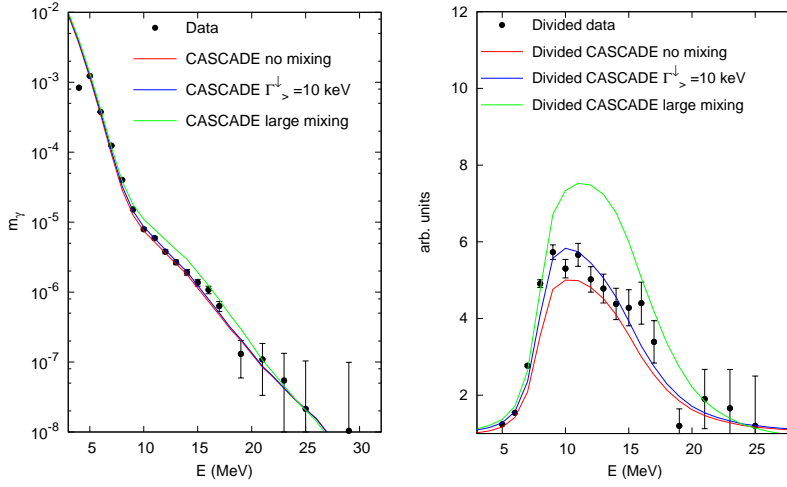


Figure 1.20: Left panel: measured γ -ray spectrum of ^{80}Zr compared with Statistical Model calculations without isospin mixing (red), with isospin mixing given by the best fitting $\Gamma_{\gamma}^{\downarrow} = 10$ keV (blue) and with a large degree of isospin mixing (green). Right panel: the same, divided by an exponential spectrum to highlight the effect of isospin mixing [68].

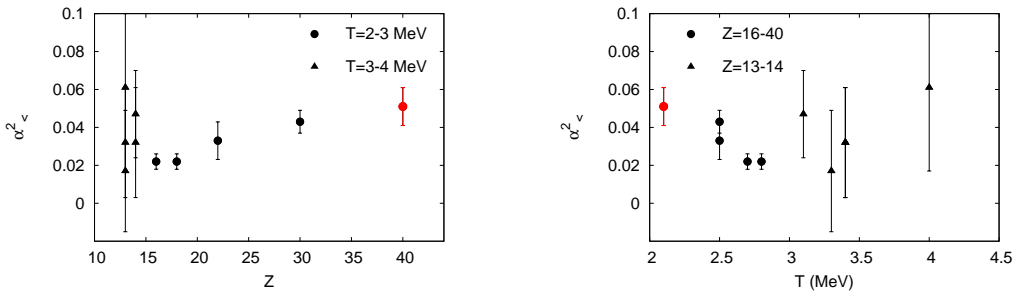


Figure 1.21: Systematics of $\alpha_{<}^2$ along to Z (left panel) and T (right panel) measured via GDR decay of the hot CN with $Z=13-14$ and $T=3-4$ MeV (triangles) and with $Z=16-40$ and $T=2-3$ MeV (dots) [68].

1.7 Isospin mixing beyond nuclear structure: The CKM matrix

In the Standard Model (SM) the Cabibbo Kobaiashi Maskawa matrix (CKM matrix) [71] contains the informations about the transitions between quarks. In the SM this matrix is hypothesised to be unitary. Testing the unitary one can provide a very important test of the validity of the SM.

The first element V_{ud} of the CKM provides the coupling between the quarks u and d , which is the basis of the β -decay transitions in nuclei. The most precise value of the V_{ud} term is obtained from the ft values of $0^+ \rightarrow 0^+$ superallowed Fermi β transition:

$$ft = \frac{K}{G_V^2 |M_F|^2} \quad (1.60)$$

where $K/(\hbar c)^6 = 2\pi^3 \hbar \ln 2 / (m_e c^2)^5 = (8120.2787 \pm 0.0011) \times 10^{-10} \text{GeV}^{-4} \text{s}$, G_V is the vector coupling constant obtained from semileptonic weak interaction and M_F is the Fermi matrix element.

All these quantities are true constant and not renormalized to another value in nuclear medium. Consequently, also ft should be nuclear independent. In practice, measuring ft values for nuclei in different mass region one realizes that this quantity change with the mass number, due to effects that are not take into account in the Eq1.60. Firstly, there are radiative corrections (δ_R) because of the emission of bremsstrahlung photons coming from emitted electrons. Secondly, the isospin is not a good quantum number and the matrix element must be corrected introducing an isospin-symmetry-breaking correction δ_C and the matrix element becomes $|M_F|^2 = |M_0|^2 (1 - \delta_C)$, where M_0 is the matrix element in the case of true symmetry. Using these corrections it is possible define a "corrected" Ft value defined as:

$$Ft \equiv ft(1 + \delta_R)(1 - \delta_C) \quad (1.61)$$

From Ft one can in principle extract the value of G_V and the value of V_{ud} , using the relation $V_{ud} = \frac{G_V}{G_F}$, where G_F is the well known weak interaction constant.

However, it is important taking many Ft values, coming from nuclei in different mass region. If they are statistically consistent one can extract the value of G_V and V_{ud} (and the associated error) from the average value of Ft . For this scope it is important to have a good estimation of the corrections, see [72, 73] and reference therein. For the isospin-symmetry-breaking correction many theoretical approaches are used to

parametrized its behaviour along to the mass number [74,75]. Unfortunately, δ_c is not a quantity directly measurable.

N. Auerbach in Ref. [76] proposed a simple analytic relation between the δ_C term and the isospin mixing probability:

$$\delta_C = 4(I + 1) \frac{V_1}{41\xi A^{2/3}} \alpha^2 \quad (1.62)$$

where $V_1 = 100$ MeV and $\xi = 3$, while α^2 is the isospin impurity in the ground state and I is the isospin of the nucleus.

In Fig.1.23 the experimental values of δ_C along to the mass number in comparison with two theoretical calculations. The experimental values were obtained using the β -decay ft [72] and the mass measurement in the case of ^{74}Rb [77]. It is worth to note that these experimental values were obtained using Eq.1.61 assuming the other known quantities and considering Ft as an adjustable parameter equal for all nuclei. This method is limited by the precision in the ft measurement (especially for short lifetime) and because it assumes valid the constance of Ft .

1.8 isospin mixing: from finite to zero temperature

As we noted before, the γ decay of the GDR it is a powerful observable when one wants to measure the isospin mixing of the nucleus, but it can provide the α^2 value only at $T > 0$. That is a clear disadvantage of our technique when one is interested in the value of the isospin mixing in the ground state for checking the effects on the nuclear structure, for the determination of the δ_c or for the comparison with the theoretical caluclations at $T = 0$. Therefore, it is very important to find a way to extrapolate the $T = 0$ starting from the GDR data at $T > 0$.

The work on ^{80}Zr of Ref. [68] shows the possibility to deduce the isospin mixing at zero temperature starting from a finite temperature value using the theoretical model described in Sec. 1.6.5, even if the analysis has some limitations because of the availability of only one data point. From that work, the need for, at least, an additional experimental point is evidenced to provide a more stringent test to model predictions [49].

In this thesis a new study addressing the problem of isospin mixing in ^{80}Zr is reported. The goals of this work is to determine the isospin mixing value at $T = 0$, using a combined analysis of the new and existing data and to extract, for the first time, the isospin mixing correction δ_C in $Z = 40$ nucleus necessary to obtain the correct ft value of super-allowed Fermi transitions.

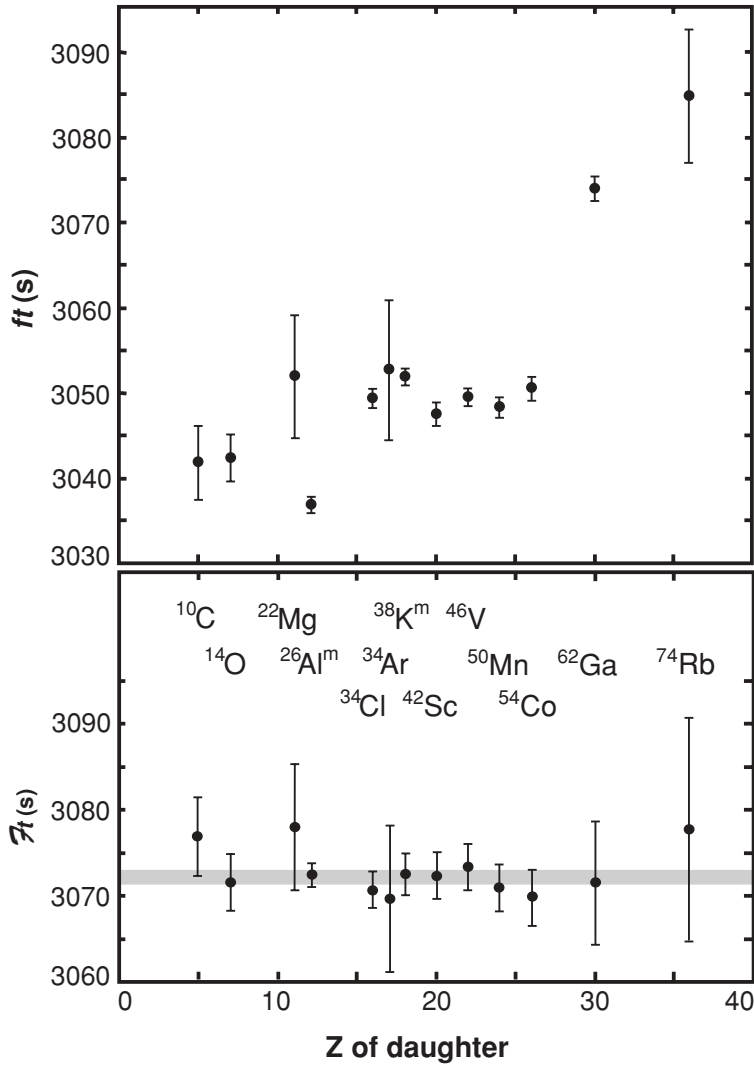


Figure 1.22: The uncorrected ft values for the twelve best known superallowed decays (top panel), compared with the same results after application of δ_R , δ_C and δ_{NS} correction terms. The grey band in the bottom panel is the average Ft value, including its uncertainty.

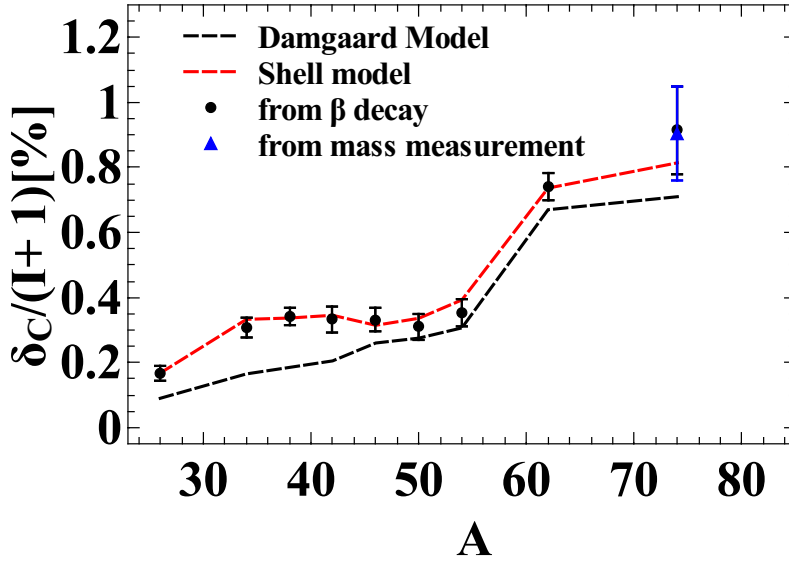


Figure 1.23: The isospin mixing correction δ_C as a function of the nuclear mass number. The dashed black line is the prediction from the Damgaard model [78], while the red line is a shell model with Saxon-Woods radial wave function prediction [79]. Black circles are the experimental points extracted from β decay as reported in Ref. [72], the blue triangle is the value obtained from the mass measurement in Ref. [77].

Experimental setup: description

The experiment was performed at the Laboratori Nazionali di Legnaro (LNL), Italy, during May 2011. The experimental setup was composed by an array of segmented HPGe, called AGATA (Advanced GAMMA Tracking Array) Demonstrator, coupled with an array of large volume LaBr₃:Ce detectors, called HECTOR⁺ (see Fig.2.1). This apparatus was used to measure the γ radiation emitted by the compound nuclei ^{80}Zr and ^{81}Rb . These nuclei were formed using a fusion reaction. In this chapter the main features of the used reactions and the used experimental setup are presented.

2.1 The experiment

In the first phase of the experiment, the ^{81}Rb nucleus was formed using a beam of ^{37}Cl ($E_{beam} \approx 95$ MeV, $I_{beam} \approx 3$ pA) with a target of ^{44}Ca (0.5 mg/cm²). This phase was ~ 70 hours long. In the second phase, the ^{80}Zr nucleus was formed using a beam of ^{40}Ca ($E_{beam} \approx 136$ MeV, $I_{beam} \approx 3.5$ pA) with a target of ^{40}Ca (0.5 mg/cm²). This phase was ~ 110 hours long. In Tab.4.2 the main characteristics of the reaction are summarized.

reaction	E_{lab} (MeV)	I_{beam} [pA]	E_{loss} (MeV)	t ($\mu\text{g}/\text{cm}^2$)	σ (mb)
$^{40}\text{Ca} + ^{40}\text{Ca}$	136	3.5	7	500	500
$^{37}\text{Cl} + ^{44}\text{Ca}$	95	3	6	500	250

Table 2.1: E_{lab} is the energy of the incoming beam, I_{beam} is the beam current, E_{loss} is the energy loss in the target of thickness t , calculated with LISE++ code [81]. σ is the fusion cross section calculated with PACE4 [80].

The ion beams were provided by the TANDEM tandem linear accelerator complex.



Figure 2.1: Picture of the experimental setup used in the experiment analysed in this work. 7 $\text{LaBr}_3\text{:Ce}$ and 4 triple clusters of the AGATA Demonstrator are visible.

2.2 AGATA Demonstrator

AGATA is an European project aimed to the development of a 4π segmented-HPGe detector for the γ -ray detection [82–86]. This new detector is based on the principle of the γ -ray tracking [84], namely the reconstruction the sequence of interactions of the single γ -ray in the crystal, which makes possible to achieve a good suppression of the Compton background, without using a detected ancillary. As a consequence a good efficiency and high peak to total ratio (P/T) are obtained. In the experiment described in this thesis AGATA Demonstrator was composed by 4 triple clusters of HPGe crystals for a total of 12 crystals and it was place at 155 cm from the target.

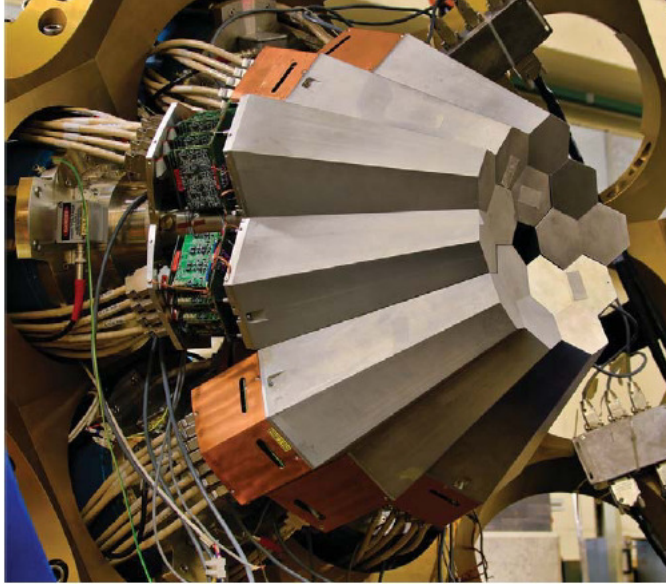


Figure 2.2: Picture of the AGATA Demonstrator at LNL. Taken from [83]

2.2.1 AGATA geometry

The geometrical structure of AGATA was studied with the goal of maximizing the solid angle covered by the array and, at the same time, minimizing development and maintenance cost. As discussed in more detail in Ref. [85], GEANT4 simulations were used to decide the best performing configuration, here only the main features are reported. The AGATA geometry is based on the geodesic tiling of a sphere with 12 regular pentagons and 180 irregular hexagons with three different shapes (see Fig.2.3). The detectors are grouped in 60 identical triple-clusters, each containing a "red", a "green", and a "blue" crystal arranged in one cryostat (see Fig.2.3).

In the standard configuration, the inner radius of the array is 23.5 cm. The full sphere has a total solid angle covered by HPGe material close to 80% and the photo-peak efficiency is as high as 50% for individual 1 MeV γ rays.

In Table 2.2 the AGATA photo-peak efficiency and the peak to total ratio (P/T) are given in comparison with an hypothetical sphere of HPGe material and the EUROBALL array [87], which was the previous array composed by HPGe detectors. Although a realistic detector can achieve only about 50% of the performance of the ideal sphere of HPGe, the efficiency gain of AGATA respect to EUROBALL is evident. Even in the case of experiment with high γ -ray multiplicity, one obtains a good efficiency and P/T.

Array	# crystals	$\varepsilon_{ph}(\%)$	$\varepsilon_{ph}(\%)$	P/T(%)	P/T(%)
		($M_\gamma=1$)	($M_\gamma=30$)	($M_\gamma=1$)	($M_\gamma=30$)
EUROBALL	239	9	6	56	37
AGATA	180	38	24	53	44
HPGe sphere	1	65	36	58	60

Table 2.2: Estimated performances of AGATA at $E_\gamma = 1$ MeV, compared to those of an ideal shell of HPGe and those of EUROBALL; ε_{ph} is the photo-peak efficiency and P/T is the peak to total ratio. These quantities were calculated taking into account the number of γ -rays emitted in coincidence (i.e γ -ray multiplicity, M_γ). Taken from [84].

Another important aspect of the AGATA array is its capability to identify the direction of the incident γ -ray, with a precision close to 1° . This provides an improvement for the energy resolution for the radiation emitted by recoiling nuclei, which is affected by the Doppler effect.

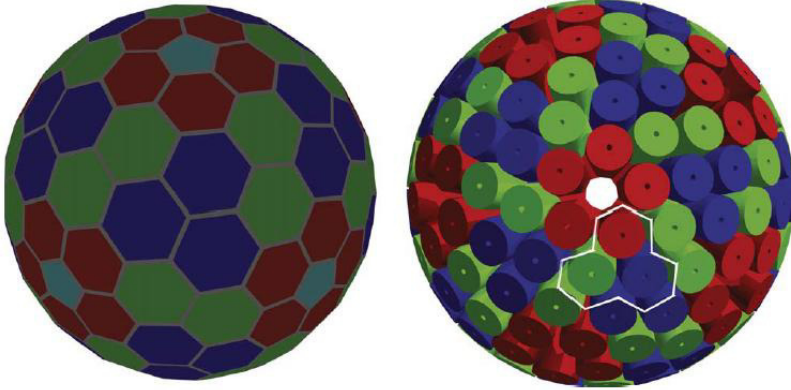


Figure 2.3: Computer aided design images of the tiling of the sphere (left) and the 180 crystal configuration (right). The cryostats and the detector encapsulation are not shown. Taken from [83]

2.2.2 Segmented detectors

In order to achieve a large tracking efficiency, one should have a 5 mm precision in the determination of 1 MeV γ -ray interaction point in the crystal. This corresponds to an effective granularity that is impossible to obtain with a physical segmentation of the crystal. However, using an electronic segmentation and using a Pulse Shape Algorithm

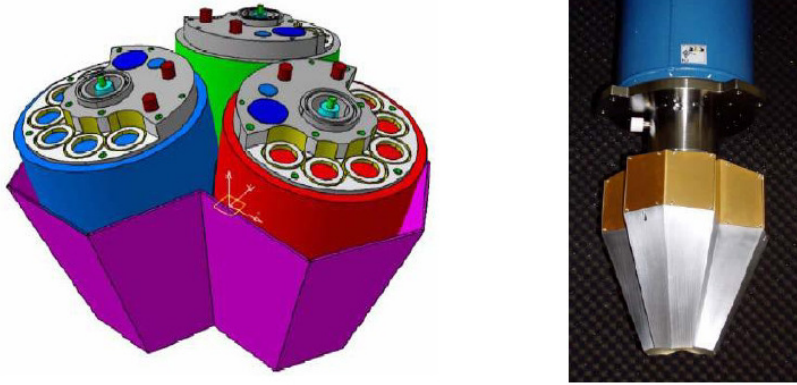


Figure 2.4: On the left, picture of an AGATA triple cluster. On the right, a triple cluster of the AGATA Demonstrator

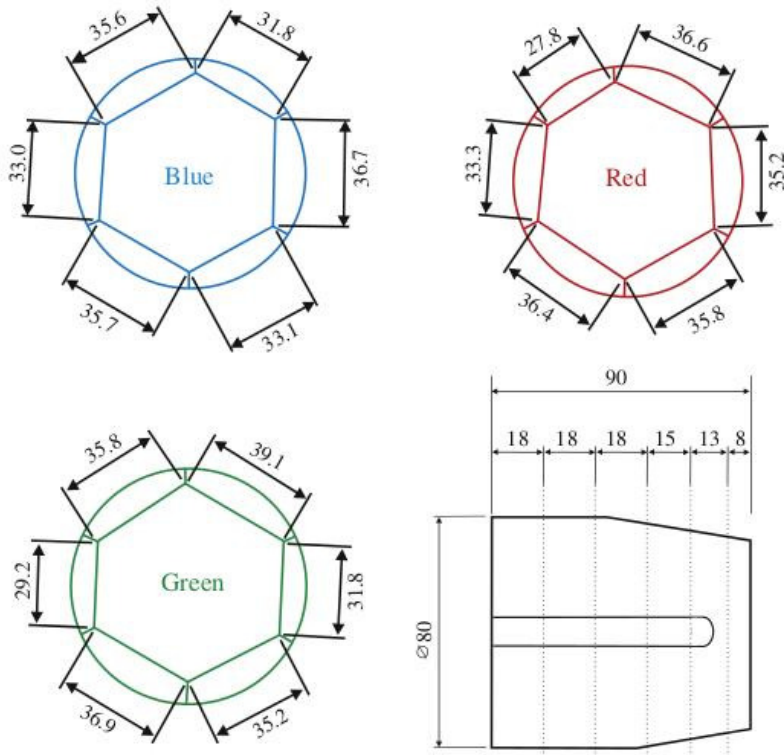
method (PSA), it is possible to achieve this accuracy.

The AGATA detector is composed by HPGe crystals in a semi-coaxial geometry, divided in 36 segments. The crystals are 90 mm long and with a diameter of 80 mm; the weight of a single crystal is around 2 kg. All crystals are *n*-type semi-conductors with an impurity concentration of around $0.4 - 1.8 \cdot 10^{10} \text{ cm}^{-3}$.

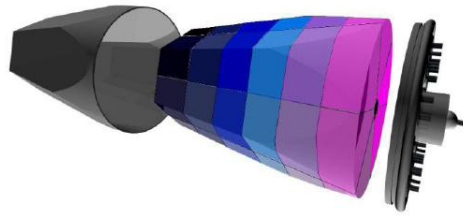
The crystals are encapsulated hermetically in a alloy capsule (with a thickness of 0.8 mm). The sector-wise segmentation goes through the middle of each hexagonal side, the longitudinal segmentation forms rings of varying thickness, optimised for a uniform distribution of the gamma-ray interactions. Because of their complexity and the need of packing them very close to each other, these detectors use the encapsulation technology developed for the clusters of EUROBALL.

In the single crystal there are 37 wires (36 for the segments + 1 central contact) passing very close to each other (the segment thickness is $\sim 2\text{cm}$, see Fig.2.5), therefore a good electrostatic shielding is necessary for each channel. The central contact, which is used to apply the low voltage signal in the crystal has a ceramic shielding.

As already noted, the AGATA array is organized in triple clusters. All three crystals of a cluster are placed in a unique cryostat cooled at a temperature of 90 K with a liquid nitrogen system. The pre-amplifiers for all segment and core signals are also cooled to 130 K; even though the power dissipated by each pre-amplifier is rather small, the sum of all 111 channels in a triple-cluster builds up to $\approx 2.3 \text{ W}$.



(a) crystal geometry



(b) segmented crystal

Figure 2.5: Drawing of the three AGATA crystal geometries. The AGATA triple cluster detector combines the three different crystal shapes. The side view (lower right) shows the position of the segmentation lines. All dimensions are given in mm. (For interpretation of the references to colour in this figure legend, the reader is referred to the web version of this article.) Taken from [83]

2.2.3 Digital electronics and Pulse Shape Analysis (PSA)

The electronic signal generated by a γ ray that interacts in the crystal has a shape that depends on the interaction position. Therefore, in principle, one can extract positional

informations studying the shape of the acquired signals. This is the core idea of the Pulse Shape Analysis (PSA) technique.

The Pulse Shape Analysis technique requires that the shape of each signal in the detector is recorded and processed digitally. Therefore, for each crystal, 37 signals (36 segments + central electrode) are digitalised at 100 MHz after the pre-amplifier by a fast ADC. The digitalized signal provide all informations (energy, time and position) about the interaction of each γ ray. Digital processing allows to use filters that have no analogic counterpart such as the Moving Window Deconvolution algorithm [88], which allows to reconstruct the original charge collection by removing the effect of the pre-amplifier response. A good energy resolution can be achieved with shorter shaping time; in this way the array is able to sustain a counting rate per detector 5 times higher than the "traditional" apparatuses (50 kHz per detector instead of 10 kHz).

As explain above, the tracking algorithm need a precise position information of the interacting γ -ray (maximum 5 mm). The PSA techniques provide the requested precision.

In general, the PSA technique is based on the comparison between the digitalized signals and a reference sample of signals. Each signal of the sample corresponds to a defined interaction point. For AGATA, the PSA has 37 signals ($S_j(E, t)$) as input, coming from each segment of the crystal. Since the detector response is linear, $S_j(E, t)$ can be written as a superposition of signals corresponding to a single interaction $S_j(x_i, y_i, z_i, t)$, weighted on the deposited energy in the crystal E_i :

$$S_j(E, t) = \sum_{i=1}^N E_i S_j(x_i, y_i, z_i, t) \quad (2.1)$$

where N is the number of interaction points in the segment and E_i is the total deposited energy in the segment. If $N = 1$ the equation is reduced to

$$S_j(E, t) = E S_j(x_i, y_i, z_i, t) \quad (2.2)$$

The solution of this equation provides the position (x_i, y_i, z_i) , which reproduce better the detected signal.

In order to achieve the request precision, the PSA is apply not only in the segment where the interaction took place, but also to the adjacent ones where a transient signal is generated. In Fig.2.6, the shapes acquired in different segments of the crystals (blue lines) are comparing with the reference signals (red line).

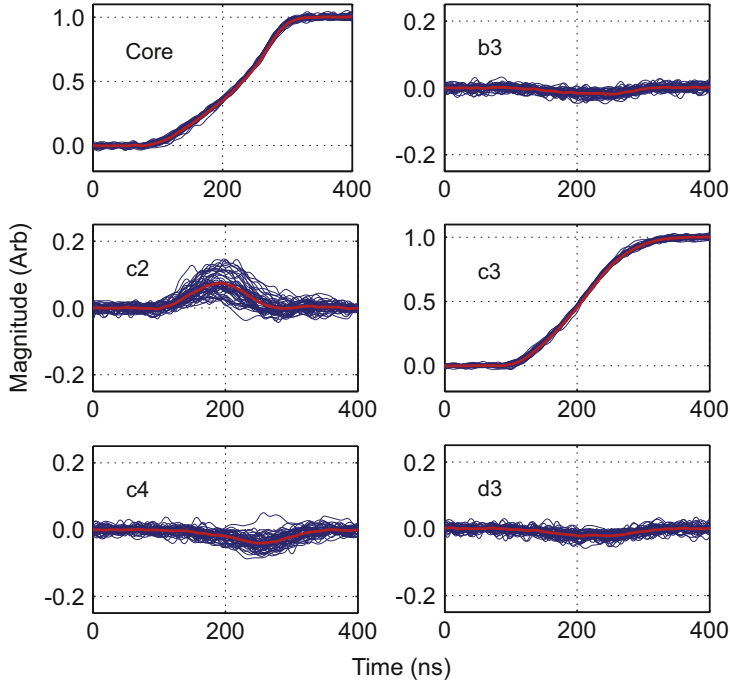


Figure 2.6: Average (thick red line) and all constituent (thin blue lines) pulse shapes for a typical interaction in segment c3. The signal induced in the core and in the close segments b3, c2, c4 and d3 are also shown. Taken from [83].

It is worth to be noted that the PSA efficiency depends strongly on the quality of the reference sample. Up to now, a precise experimental sample is not available. However, using the PSA in AGATA one can have 1 deg precision in the interaction point. Such a precision allows a good Doppler correction.

Thanks to the position resolution, a precise Doppler correction can be made. Indeed, the limit of the Doppler correction is the uncertainty in the position determination that originates a width broadening of the peak in the energy spectrum (the so-called Doppler broadening). The performance of AGATA Demonstrator for the Doppler correction was tested at 15.1 MeV, with a in-flight γ ray, coming from the reaction $d(^{11}\text{B}, n\gamma)^{12}\text{C}$ [89]. An energy resolution of about 119 keV was obtained after Doppler correction. It is worth to be noted that the energy resolution obtained is worst than the expected trend (see Fig.2.10); the reason is that the 15.1 MeV γ ray is emitted in flight.

In Fig.2.7 is shown the in-flight γ -ray energy spectrum without the Doppler correction (dots), with the Doppler correction and considering the center of the crystal as po-

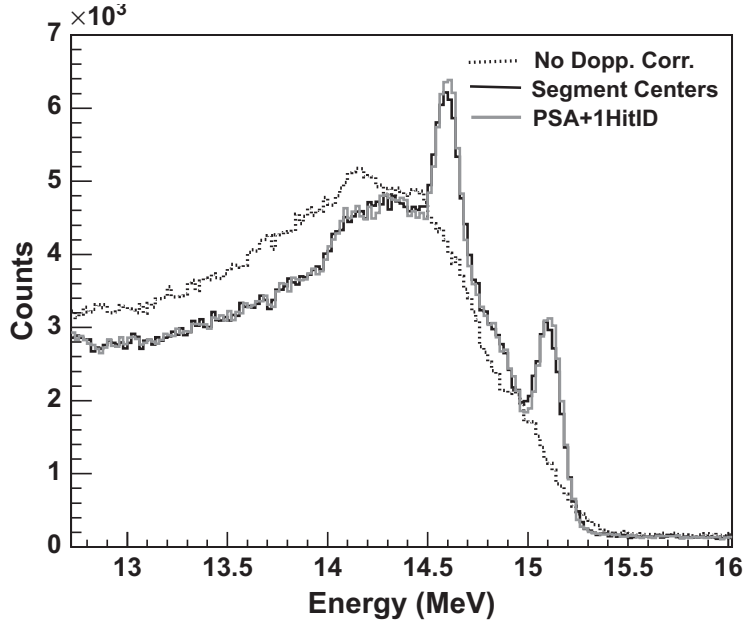


Figure 2.7: Gamma-ray spectra acquired during the in-beam test, displayed in the region around 15MeV. The spectrum without Doppler correction (dashed black line) is compared to: (i) the spectrum obtained using only the central position of segments (thin black line) and (ii) the spectrum obtained using the (thin gray line). Taken from [89]

sition (black line) and, finally, considering the position obtained with a PSA technique (red line).

2.2.4 Tracking algorithm

The γ radiation interacts in the material in three different modes [90], as illustrated in Fig 2.13:

- photo-electric effect: the radiation is completely adsorbed by the material in a single hit. This is the dominant process up to 0.3 MeV.
- Compton effect: the radiation loses a part of its energy and it scatters in a precise direction. This is the dominant process in a energy range between 0.3 - 3 MeV.
- Pair production: Owing to the interaction with the atomic nucleus of the material, the γ ray annihilates in a pair e^-/e^+ . e^+ annihilates emitting two γ rays of 511 keV in opposite direction. This the dominant process for energy grater than 3 MeV.

Since the γ -ray interaction is a stochastic process, a γ ray has a certain probability to interact in a material with one of these three processes. The probability, depends mainly on the γ -ray energy and the charge of the material Z .

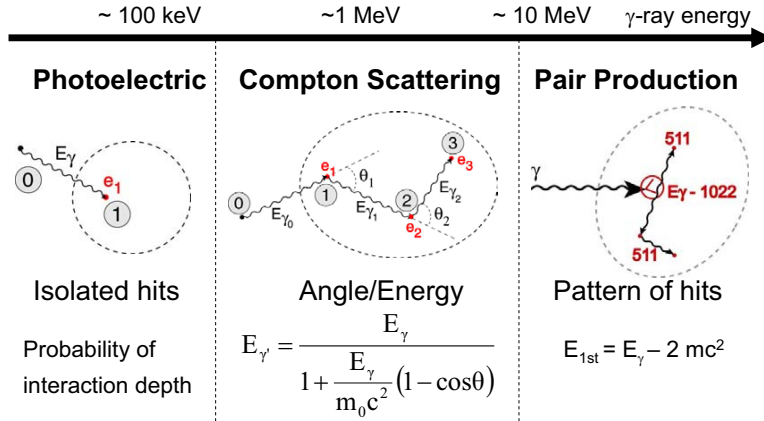


Figure 2.8: The relevant γ -ray interaction mechanisms and the features exploited by the tracking algorithms. Taken from [84].

Typically, the distance between two consecutive interactions from the same γ ray is around 1 cm or less. The time resolution of the detector is some ns, therefore all consecutive interactions are simultaneous for the detector.

The scope of the tracking algorithm is to reorganize temporally the interactions and to reconstruct the γ -ray path in the crystal. Two main typologies of algorithms exist: *tracking forward* [84] and *backtracking* [91].

In the *tracking forward* algorithm the first step is the identification of clusters of interaction points that may belong to a single γ -ray. Looking at the forward peaking of Compton scattering cross-section, clusters are identified as a set of interaction points with an angular distance $\leq \theta_0$ between each other (link algorithm) or with respect to a given point (leader algorithm). Secondly, each cluster is evaluated to determine whether it contains all the interaction points belonging to a single gamma-ray with the following criteria:

- Do the interaction points satisfy the Compton scattering formula? In this case, the tracking algorithm uses the angle-energy relation of Compton scattering to determine the most likely scattering sequence from the position and energy of the interaction points. The cluster is defined good using a χ square procedure.

- If the cluster is composed by a single interaction point, does the energy satisfy photoelectric conditions? The algorithm evaluates if the mean free path of the radiation with the deposited energy is compatible with a photoelectric process. A monte-Carlo approach is used to decide if to consider the interaction point as an actual photoelectric event or if to discard it as an isolated Compton scattering event.
- Do the interaction points correspond to a pair production event? If there are two gamma-rays of energy equal to 511 keV and an interaction point in the middle with energy greater than 1022 keV, the three energies are summed and considered as a single gamma-ray.

This technique allows a reconstruction of the total energy deposited in the crystal for a γ -ray and it is an alternative to the standard Add-Back technique

The clusters which do not satisfy any of the above criteria are rejected, thus improving the P/T (peak to total) ratio of the spectra without the need for Compton suppression shields. If a large solid angle is covered with segmented germanium detectors, the combination of PSA and gamma-ray tracking allows for a very high photo-peak efficiency together with a good P/T ratio.

The backtracking algorithm is based on the fact that the photoelectric energy deposition is almost independent from the incident energy and is peaked around 100-250 keV; it assumes that the interaction points within a given deposited energy interval $E_{min} \leq E_i \leq E_{max}$ are the last interaction (in time) of a fully absorbed gamma-ray; the algorithm then finds the closest interaction to the photoelectric one, it computes the scattering angle using the incident and the scattered energies and, finally, it searches for the other previous interactions along this direction; such process is iterated until the direction points directly to the target. This algorithm, however, was found to be less efficient and showed a worse P/T in the reconstructed spectra, and therefore it was not used for our analysis.

2.2.5 AGATA Demonstrator performances

The energy resolution is one of the main features of any HPGe detector. The response of AGATA was tested in an energy range between 2 and 9 MeV using an Am-Be-Fe source, as reported in Ref. [89]. In Fig.2.10, the energy resolution is plotted and one can see that the experimental data follow the expected $E^{-1/2}$ trend (indicated by the black dashed line). The FWHM of the highest-energy gamma line (i.e. 9297.8 keV) is 6.1 keV in the

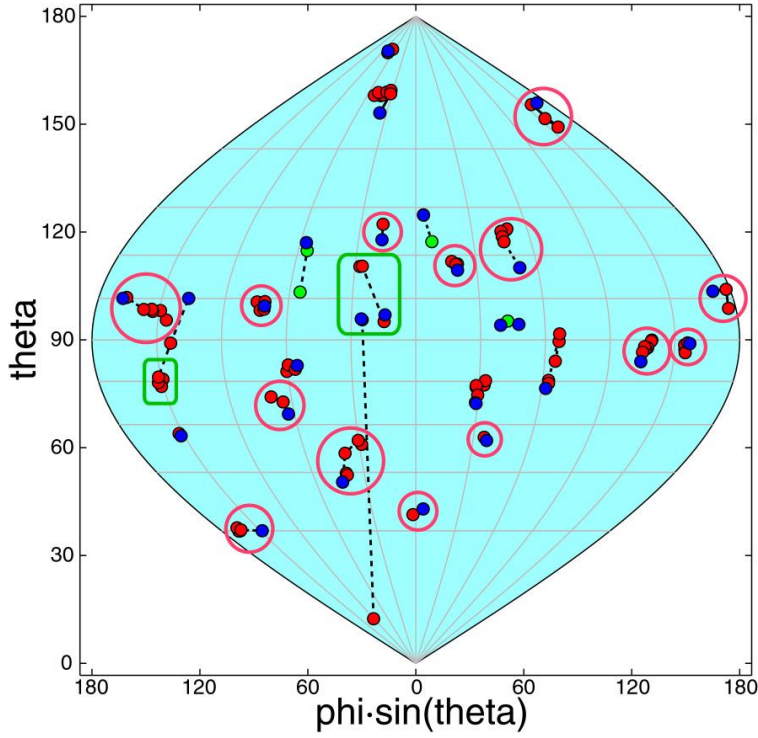


Figure 2.9: Plot of all interaction points in a 4π HPGe shell from a simulated event with 30 gammas of 1.3 MeV; red circles represent clusters which are identify as belonging to a single gamma-ray, while green squares represent clusters that are discarded by the tracking

case of the single crystal with the best performances, and 7.6 keV using an Add-Back procedure. Another important feature of a HPGe detector is the linearity of its response along to the deposited energy. Percent deviation of the experimental data from tabulated energies is reported in Fig.2.10 as a function of γ -ray energy. The deviation is defined as the difference between measured and tabulated energy divided by measured energy. As expected data corresponding to gamma rays emitted in-flight show larger error bars. It is found that the total deviations from ideal linearity are lower than 0.1% in the energy range 2 – 15 MeV.

The other fundamental property of a detector is the efficiency in the detection process. The detector efficiency is defined as the total photo-peak absorption probability over the 4π solid angle. In the experiment the efficiency can depend on many factors: the energy of the γ -ray detected, the distance of the detector, the number of γ -ray emitted in the reaction (i.e. γ -ray multiplicity), the recoil nucleus velocity and, in the case

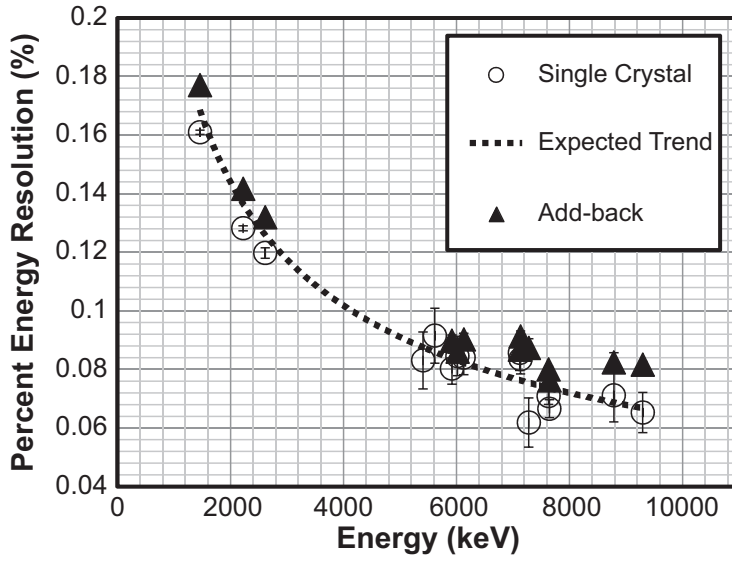


Figure 2.10: Relative energy resolution of the AGATA detectors is given for the Am–Be–Fe source data. The data for the best performing single detector are shown by empty black circles. The black triangles represent instead the energy resolution for the add-back procedure, performed among all crystals that fired in each event. The experimental data follow the expected $E^{1/2}$ trend (indicated by the dashed black line). Taken from [89].

of AGATA Demonstrator, the tracking algorithm. The reference position of AGATA Demonstrator is placed at 23.5 cm from the target, The simulated photo-peak efficiency as a function of the shift towards the geometrical centre and the γ -ray multiplicity is shown in Fig.2.12 [85].

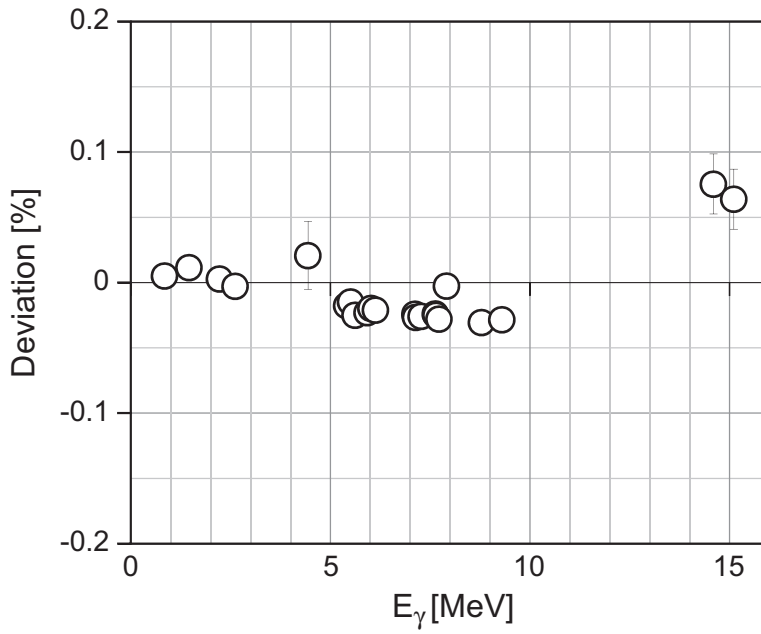


Figure 2.11: Deviation of the measured energies from the tabulated energy for each gamma line of the Am-Be-Fe source and for the 4.4 and 15.1 MeV gammas from the in-beam test. Taken from [89].

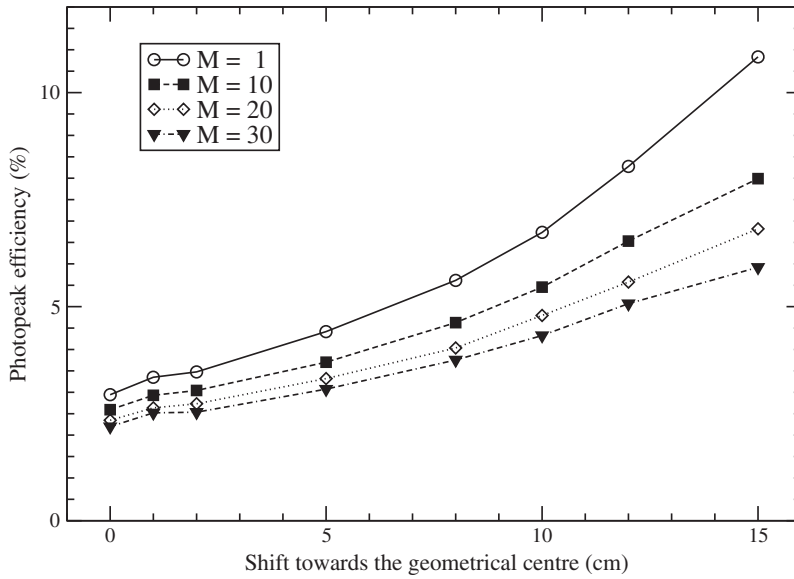


Figure 2.12: Photo-peak efficiency of the AGATA Demonstrator for 1 MeV photons emitted from a point source at rest. Taken from [85]

2.3 LaBr₃:Ce

The Cerium doped Lanthanum bromide (LaBr₃:Ce) crystal is an inorganic scintillator, made available to the scientific community only few years ago. The excellent properties of this new material has generated a large interest in the scientific community. Indeed, thanks to very good intrinsic time (< 1 ns), energy resolution ($\approx 3\%$ at 661 keV) and the good detection efficiency, LaBr₃:Ce detectors can provide at the same time clean spectroscopic information from a few ten keV up to tens of MeV and an excellent time resolution which allows a good timing measurement and an efficient γ -n discrimination. Moreover, thanks to the availability of crystals in volumes larger than 1000 cc, a LaBr₃:Ce-based array can operate as an extremely efficient setup in γ -ray experiments, as the study of Giant Resonance states or experiments with radioactive beams. The main intrinsic features of LaBr₃:Ce scintillators are summarized in Tab.2.3 and compared with those of other scintillators (see also Fig.2.13).

The properties of LaBr₃:Ce were largely investigated in the recent years. An intense R&D activity was conducted in Milano group to test the crystal performances and to find the best possible detector configuration (photo-tube, read-out electronics, acquisition system, etc..) [92,93].

In the experiment described in this thesis 6 large LaBr₃:Ce (3.5'' x 8'') and 1 smaller LaBr₃:Ce (3'' x 3'') were used and placed at 25 cm from the target.

Scintillator	Light Yield (10 ³ fotoni/MeV)	Decay Times(ns)	Density(g/cm ³)
NaI:Tl	38	250	3.67
LaCl ₃ :Ce	49	28	3.85
LaBr ₃ :Ce	63	16	5.08
BaF ₂	1.8	0.7	4.88
BGO	9	300	7.13

Table 2.3: Comparison between the properties of some scintillators used in nuclear physics. Light Yield is the number of photons emitted per MeV deposited in the crystal, which is related to the energy resolution of the detector. Decay Time is the time needed to emit photons and it is related to the time resolution.

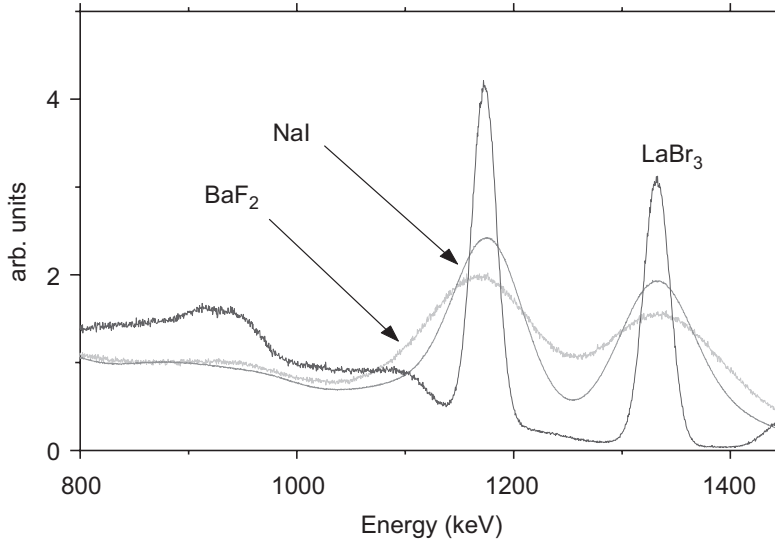


Figure 2.13: Comparison of the ^{60}Co energy spectrum measured with the $1'' \times 1''$ $\text{LaBr}_3\text{:Ce}$ with those measured with a NaI and with a BaF_2 detector. Taken from [92].

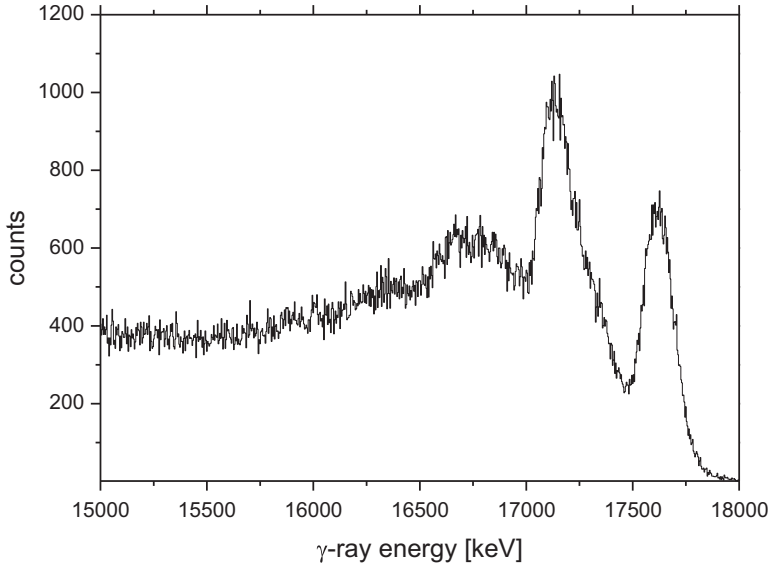


Figure 2.14: The energy spectrum measured at the ATOMKI Institute with a 17.6 MeV mono-chromatic γ rays. Taken from [93].

2.3.1 $\text{LaBr}_3\text{:Ce}$ performances

The energy response of a large volume LaBr_3 detector was investigated from few keV up to 20 MeV [93]. The energy resolution is a crucial factor in case of high-energy γ -ray

measurements and LaBr₃:Ce allows to have a clear separation of the full energy peak and the first escape peak up to 20 - 30 MeV (see Fig.2.14).

In Figure is plotted the energy resolution of a detector as a function of the γ -ray energy, using a digital acquisition system. As shown in Fig.2.15, the energy resolution trend deviates from the standard $E^{-1/2}$ curve (dashed line), showing that the energy resolution saturates in the detection of high-energy γ rays. The solid curve take into account even the saturation phenomenon, introducing another term in the standard formula for the energy resolution:

$$ER = \sqrt{a + bE + cE^2} \quad (2.3)$$

The a term represents the noise contribution unrelated to the measured energy, b is the contribution for the statistical noise while c is the saturation term.

The absolute full energy peak efficiency of the γ -ray detection was investigated with a ⁶⁰Co source (two γ -rays in coincidence), using the 'sum peak' technique. This method provide the absolute photo-peak efficiency at 1173 keV and 1332 keV. The results are in very good agreement with those obtained using the simulation code GEANT3. In Fig.2.16 the comparison between the experimental data and the simulation is shown.

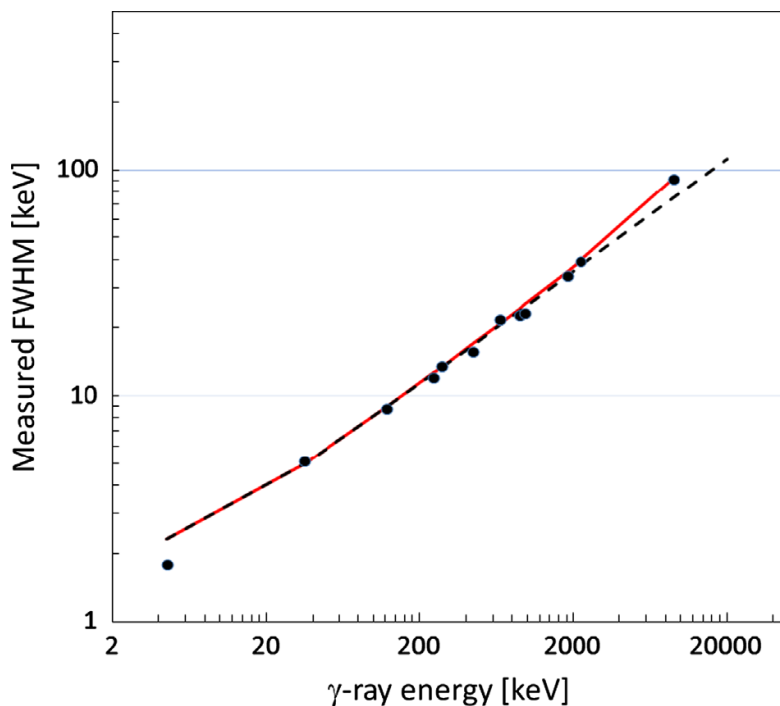


Figure 2.15: The FWHM energy resolution in the energy range between 5keV and 9 MeV measured with the a 3.5'' x 8'' LaBr3:Ce detector using digital electronics. The dashed line represent the best trend using the 'classic' FWHM formula ($\text{FWHM} = \sqrt{(a + bE)}$) which takes into account the electronic noise (a) and the statistical contribution (b). while the solid line takes into account also a third contribution which causes the energy resolution saturation ($\text{FWHM} = \sqrt{(a + bE + cE^2)}$). Taken from [93].

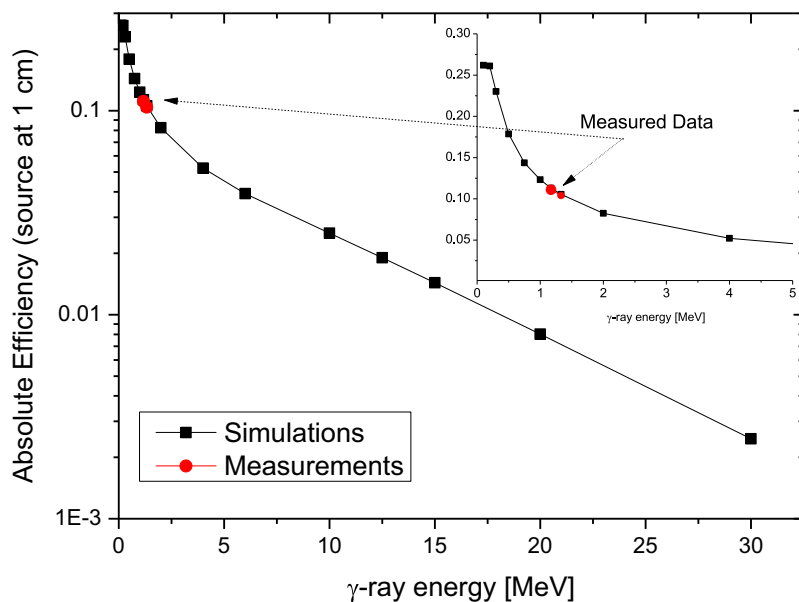


Figure 2.16: Simulated and experimentally measured values of absolute full-energy peak efficiency for a large volume 3.5" x 8" LaBr₃:Ce detector, with a ⁶⁰Co source positioned 10mm away from the detector surface. The inset plot shows a magnified portion of them in a graph up to 5MeV energy range. Taken from [93]

2.4 Data Acquisition (DAQ) system

Each of the 36 signals coming from a crystal of AGATA was digitalized using a sampling frequency of 100 MHz at 14 bits precision. For each segment, a pulse trace of 60 samples is recorded. In order to have an on-line analysis of the acquired data, the PSA needs to work on the single trace in real time and the tracking algorithm must reconstruct the detected γ rays.

Therefore, the Data Acquisition software (DAQ) has to handle a large amount of data, control a computing farm for the PSA and tracking algorithms, and coordinate the flow of information between the digitizers, the computing farm, and the disk server where all the data are written. All of this is performed by a NARVAL-based DAQ software [94].

The ancillary detectors (as Hector⁺) are controlled by an independent data acquisition system, which works in a KMAX framework [95], which communicates with NARVAL using a TPC/IP protocol.

In NARVAL every actions is operated by an *actor*, which is a process running on a Linux machine. Three different *actors* exist:

- *producer*: they interface with the hardware and read out the data;
- *intermediary*: they perform operations on the data, receiving input and sending output from/to one or more other actors;
- *consumer*: they can only receive input from the other actors, and store the data to disk.

For NARVAL each crystal of AGATA is considered as a separate entity and the whole detector as a set of data synchronized between each other. The data synchronization is guaranteed by the Global Trigger and Synchronization (GTS) hardware using a common digital clock.

For each AGATA detector there is a producer actor reading the pulse traces from the front-end electronics; the traces are sent (together with the timestamp information) to an intermediary that performs the PSA and to a consumer that writes them to disk; the PSA data from all detectors are sent to an intermediary that acts as event builder, matching the data from different detectors through the timestamp information.

For the ancillary detectors (as HECTOR⁺ in this analysis), there is a producer actor that receives the data from the KMAX acquisition, kept synchronized to the GTS via the AGAVA (AGATA Ancillary VME Adapter) module. The producer sends the VME

data to a consumer that writes them to disk and to an intermediary that decodes the VME words and sends only the actual data words to the event builder, discarding VME header and trailer words. The builder then matches the ancillary data to the AGATA data and sends the event to another intermediary that performs the online tracking, for AGATA Demonstrator only.

2.4.1 Trigger conditions and event selection

When a γ -ray is detected in an AGATA crystal, a trigger request is formed and sent via the GTS to the trigger processor, which can validate the request, meaning that all the traces for the event are acquired, written and processed, or reject it. This software trigger can be used to make multiplicity requirements on the AGATA crystals, or to make a coincidence between AGATA and the ancillary detectors via the AGAVA module.

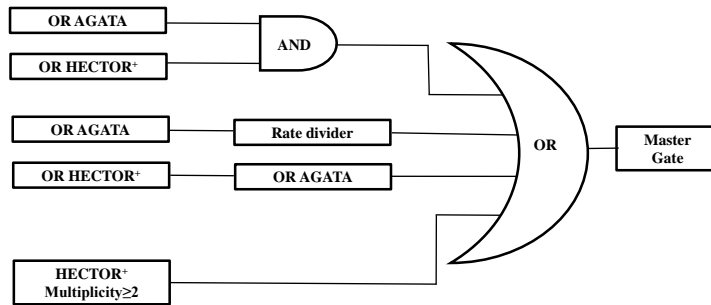


Figure 2.17: Schematic representation of the trigger conditions in the data acquisition system of the experiment.

This method, however, was not suitable for our experiment due to the complexity of our trigger condition. Therefore, we used standard NIM electronics to build the master gate, which was sent via AGAVA as a trigger request, and had the software trigger validate it. The master gate is schematically described in Fig.2.17 and is the logical "OR" of four conditions:

- coincidence between AGATA detector and HECTOR⁺ (marker AGATA& LaBr)
- Multiplicity detected larger or equal than two in HECTOR⁺ (marker LaBrM2)

- the AGATA scaled-down single (marker AGATA single)
- the HECTOR⁺ scaled-down single (marker LaBr single)

the logic signal "OR" of AGATA detector was made using the analogical output of each AGATA detector, sent to a standard CFD modules and then to a logical OR. The logical signal "OR" of HECTOR⁺ and the logical signal of the multiplicity were provided by the BaFPro module. In order to separate the different classes of event, four channels of the TDCs were used as markers as shown in Fig.2.18.

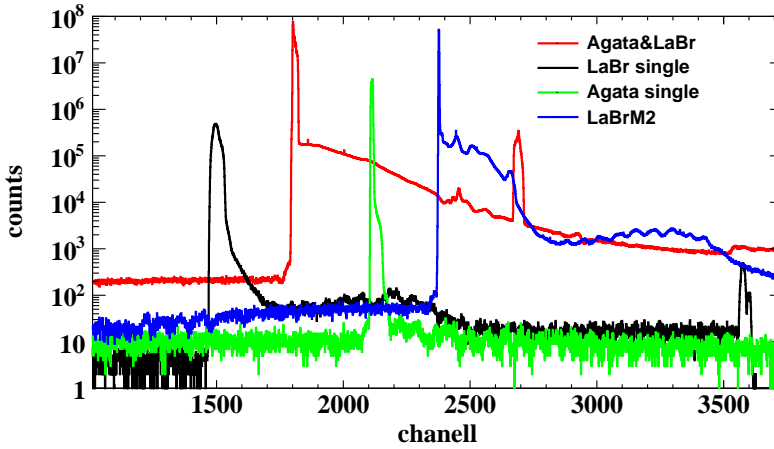


Figure 2.18: marker spectra for different trigger conditions. the larger part of the data is concentrated in narrow and separated peak.

Using the marker information, in the sort code we identified four classes of events:

- AGATA event: event with the coincidence between AGATA detector and HECTOR⁺, it characterized by the follow conditions in the sort:
 - marker AGATA& LaBr > 0;
 - marker AGATA single = 0;
- LaBr₃:Ce event: event with the coincidence between two LaBr₃:Ce and without any coincidence with AGATA, it characterized by the follow conditions in the sort:
 - marker LaBrM2 > 0;
 - marker marker AGATA& LaBr = 0;
 - marker LaBr single = 0;

- AGATA single event: event with only AGATA scaled-down single
- LaBr₃:Ce single event: event with only LaBr₃:Ce scaled-down single.

(a) $^{40}\text{Ca} + ^{40}\text{Ca}$			
Trigger	# events [%]	Events	# events [%]
Agata& LaBr	84%	Agata	81%
LaBrM2	20%	LaBr ₃ :Ce	11%
Agata single	4.3%	Agata single	4.3%
LaBr single	1.8%	LaBr ₃ :Ce single	1.8%

(b) $^{37}\text{Cl} + ^{44}\text{Ca}$			
Trigger	# events [%]	Events	# events [%]
Agata& LaBr	83%	Agata	76%
LaBrM2	21%	LaBr ₃ :Ce	12%
Agata single	5%	Agata single	1.8%
LaBr single	1.8%	LaBr ₃ :Ce single	5%

Table 2.4: number of events for each trigger and for each class of event is reported. An acquired event more than one marker could be activated; this is the reason because the sum of the trigger events is larger than 100%.

In Table 2.4 the number of events for each trigger and for each class of event is reported. It is worth to note that for an acquired event more than one marker could be activated; this is the reason because the sum of the trigger events in Table 2.4 is larger than 100%. A half of the events with trigger LaBrM2 are detected also with AGATA and then are considered as Agata events in the sort code.

A small part of the total events is rejected during the sort code because the time information or the energy information were corrupted; this is the reason because the sum of events is not 100%.

Experimental setup: data analysis

This chapter reports the first steps of the data analysis: the performances of the AGATA Demonstrator and HECTOR⁺ were studied (energy resolution, linearity, time resolution) as well as their response functions. All these informations were used in the next step of the analysis, where the physical informations were extracted.

For testing the performances of the detectors and to have a high-energy calibration point, a $^{11}\text{B} + \text{D} = ^{13}\text{C}^*$ ($E_{\text{beam}} \approx 20 \text{ MeV}$) fusion reaction was also studied. Indeed, $^{13}\text{C}^*$ emits a 15.1 MeV γ ray in flight. Therefore, this reaction can be used for testing the detector response to a high-energy γ -ray (at an energy similar to the γ -ray emitted by the GDR).

Unfortunately, for a problem in the acquisition system during the experiment, only the AGATA Demonstrator data were available for this reaction.

3.1 AGATA Demonstrator

As described in Chapter 2, the performances of the AGATA Demonstrator are based on the principles of PSA and γ -ray tracking. During the experiment, these operations are performed in real time by the NARVAL Data Acquisition (DAQ) system, but they also can be performed again after the experiment with a C++ emulator of NARVAL. This process is possible because the DAQ writes a list-mode file with the digitalized signals and the time informations of each crystal of AGATA.

The NARVAL emulator can process all files, performing again the PSA and merging the informations from different crystals. This is the so-called *replay* procedure, because, in a sense, it is a repetition of the experiment. The data replay is divided in two phases: in the first phase, the PSA is made and all the informations are written on the disk; in

the second phase, the γ -ray tracking is implemented. The PSA is a very low process and it occupies a lot of memory and CPU: 6 computers worked in parallel for 1 week to perform the PSA of 180 hours of measurement. On the other hand, the γ -ray tracking is a fast process and it can be easily repeated changing the algorithm parameters.

After the PSA and the γ -ray tracking the data are saved in a ROOT tree structure [96], containing, for each event, all the relevant informations (γ -ray energy, position and time), provided by each detector. A sort code was developed for the analysis of the data.

3.1.1 Time resolution

For each γ -ray reconstructed, a *timestamp* is associated by the tracking algorithm. This is the measurement of the absolute time from the start of the GTS clock in 10 ns steps. A more precise information is provided by the PSA, which calculates the starting point of the signal using a linear interpolation.

The sum of these two values gives the detection time of the γ ray relative to the start time of the GTS. To obtain an useful physical information, however, the detection time in AGATA must be correlated with the detection time in the ancillary detectors (LaBr₃:Ce detectors in this experiment). The latter time information is given by the GTS timestamp of the ancillary, in step of 10 ns; a better precision is obtained by adding to the timestamp the so-called "phase shift", which is acquired by one channel of the TDCs and measures when the VME master gate was opened relative to the GTS clock.

Therefore, the time associated to an event is defined as:

$$t_{\gamma} = T_{AGATA} - T_{AGAVA} + T_{PSA} - T_{phaseshift} \quad (3.1)$$

where T_{AGATA} and T_{AGAVA} are the AGATA timestamp and the ancillary timestamp respectively. In Fig. 3.1, it is plotted the AGATA time spectrum for the reaction $^{40}\text{Ca} + ^{40}\text{Ca}$ obtained using the Eq.3.1. Several structures are visible. They correspond to the different trigger conditions in the acquisition process (see Fig.3.2).

As already noted in the previous chapter, the larger part of the data are events related to a coincidence between AGATA Demonstrator and HECTOR⁺ (AGATA&LaBr event, as defined in Chapter 2). The time distribution associated to these events has a FWHM of ≈ 25 ns. This time resolution is not good enough to distinguish temporally the detection of neutrons or γ in the array.

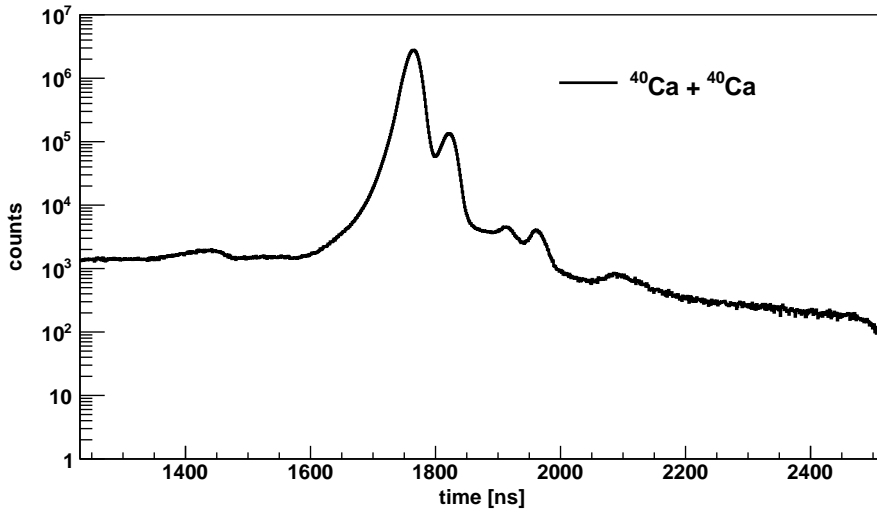


Figure 3.1: Time spectrum of AGATA Demonstrator obtained using Eq.3.1, without any condition in the sort. Several structure are visible.

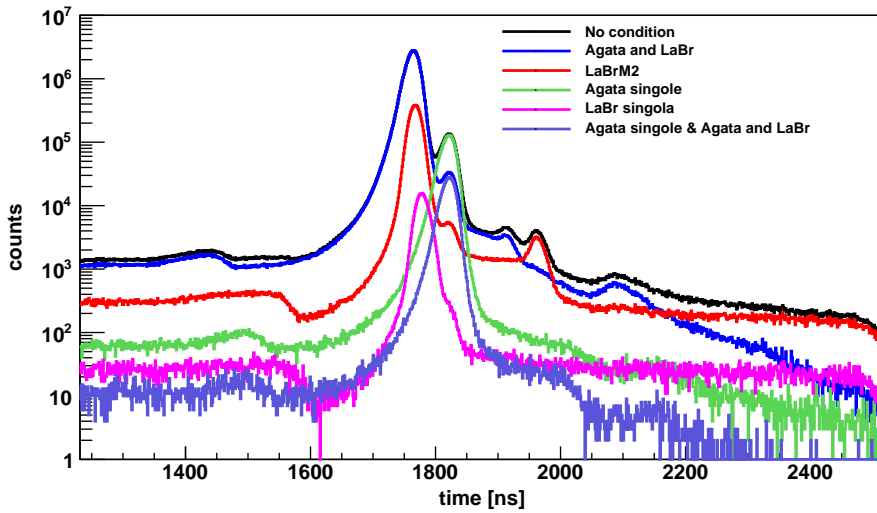


Figure 3.2: Time spectra of AGATA correspond to different trigger conditions. In this way, it is clear the origin of the structure in Fig 3.1.

3.1.2 Energy resolution and linearity

The energy calibration of AGATA was performed during the PSA. The calibration coefficients were calculated using a ^{60}Co source (1173 keV and 1332 keV). Since the γ -rays are emitted in flight, a Doppler correction is necessary to have the γ -ray energy spectrum in the Center of Mass (CM) system.

The relation between the energy detected (E_{LAB}) and the energy emitted (E_{CM}) is:

$$E_{CM} = E_{LAB} \frac{(1 - \beta \cos \theta)}{\sqrt{1 - \beta^2}} \quad (3.2)$$

where $\beta = v/c$ is the velocity of the nucleus, while θ is the angle between the nucleus direction (which can be considered the same as the beam direction) and the γ -ray emitted. The latter quantity can be obtained with a good precision using the position information of AGATA Detector as explained in Chapter 2.

Using Eq. 3.2, therefore, it is possible to recalibrate the spectrum, and using the CM reference system. The angular uncertainty ($\Delta\theta$) of the γ -ray emitted introduce a bias in the energy calculation (ΔE), which is responsible to the Doppler broadening, equal to:

$$\Delta E = 2E_{CM}\beta \sin \theta \Delta\theta \quad (3.3)$$

Thanks to the PSA, however, the position resolution of the γ -ray detected in AGATA (namely $\Delta\theta$) is good and thus ΔE is expected to remain small, as $E_{CM}, \theta, \Delta\theta$ are known.

In Eq.3.2 only the β value remains to determine. This value can be obtained by the experimental data searching for the value which maximizes the intensity and minimizes the width (i.e. smaller Doppler broadening) of a low-energy transition peak in the energy spectrum. In the case of $^{11}\text{B} + \text{D}$ we can only use the 15.1 MeV as reference peak, because no low-energy transitions were present. Another way to determine the β value is using a statistical code.

In the Table 4.2 the experimental values are compared with the values obtained using the statistical code PACE4. In general β_{EXP} are smaller than β_{SIM} . A possible explanation is that β_{SIM} is the v/c value when the compound nucleus is formed, while β_{EXP} is the value at the moment of the γ decay.

In the analysis, the β value obtained from the experimental data was used in the sort code to perform the Doppler correction

Fig.3.3 shows the $^{11}\text{B} + \text{D}$ spectrum before and after the Doppler correction. Without the Doppler correction (black line) only a bump is visible. On the other hand, thanks to

reaction	β_{SIM}	β_{EXP}
$^{40}\text{Ca} + ^{40}\text{Ca}$	0.042	0.038
$^{37}\text{Cl} + ^{44}\text{Ca}$	0.035	0.028
$^{11}\text{B} + \text{D}$	0.05	0.046

Table 3.1: β_{SIM} and β_{EXP} for all reactions are reported. The simulated values were obtained using the PACE4 code, while the experimental value were obtained studying the low-energy peaks of the reactions as explained in the text.

the Doppler correction (red line) and using the PSA technique, the photo-peak is visible (FWHM \approx 130 keV) and it is located at the correct energy (\approx 15.1 MeV), the first-escape peak is clearly visible. The width of the 15.1 MeV peak is in good agreement with that reported in Ref. [89]

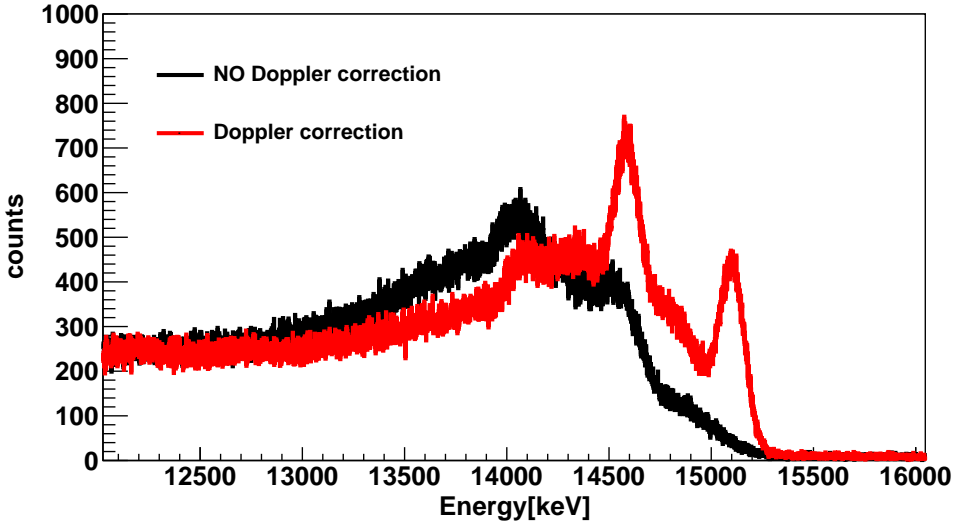


Figure 3.3: $^{11}\text{B} + \text{D}$ spectrum before and after the Doppler correction. The black line was obtained without the Doppler correction. The red line was obtained performing the Doppler correction. The FWHM = 130 keV of the photo-peak is in good agreement with that found in Ref.

The low-energy part of the AGATA spectrum is characterized by the last γ -ray transitions of the residual nuclei populated in the CN particle decay. In Fig. 3.4 ($^{40}\text{Ca} + ^{40}\text{Ca}$ reaction) and Fig. 3.5 ($^{37}\text{Cl} + ^{44}\text{Ca}$ reaction) the low-energy spectrum of AGATA is shown before (black line) and after (red line) the Doppler correction. Thanks to the Doppler correction all peaks transitions are clearly visible, separated and placed in the

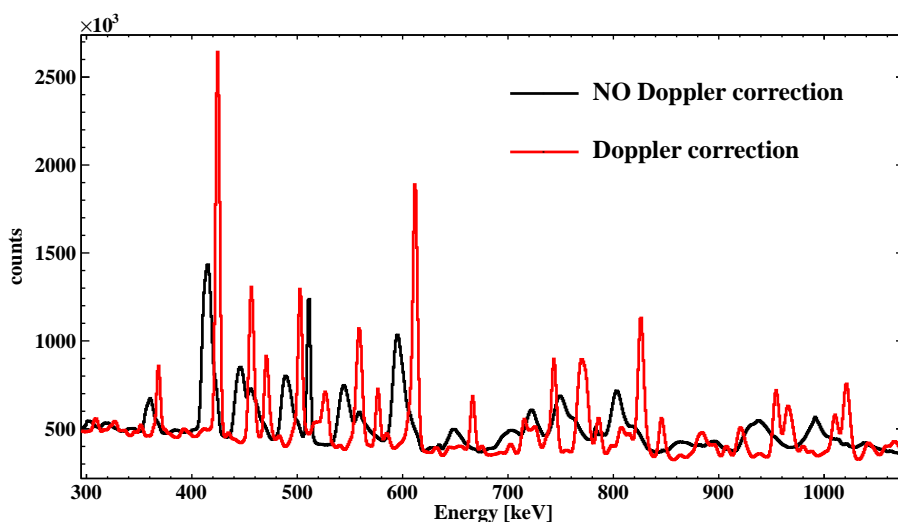


Figure 3.4: Energy spectrum of AGATA demonstrator in the reaction $^{40}\text{Ca} + ^{40}\text{Ca}$. The black line was obtained without the Doppler correction. The red line was obtained performing the Doppler correction.

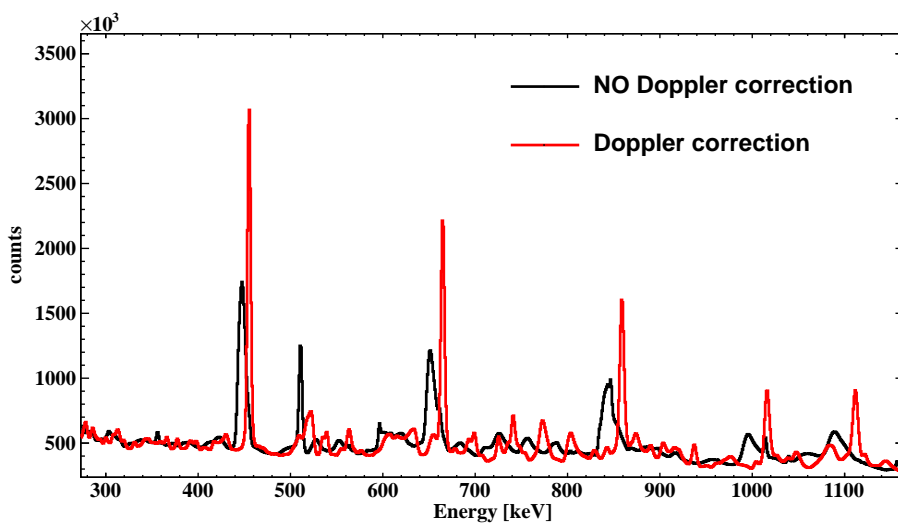


Figure 3.5: Energy spectrum of AGATA demonstrator in the reaction $^{37}\text{Cl} + ^{44}\text{Ca}$. The black line was obtained without the Doppler correction. The red line was obtained performing the Doppler correction.

right energy position. This allows to recognise all the transitions and to identify the residual nuclei populated. As we will discuss in the next chapter, this information is used in the next steps of the analysis for checking the validity of the statistical model calculations.

In Fig. 3.6 and 3.7 the energy resolution (defined as FWHM/E_γ) trend for both reactions is shown. It is evident that the measured energy resolution follow the expected $1/\Delta E$ trend, corresponding to the red solid curve in the plots.

In Fig.3.8 the deviation between measured γ -ray energies (E_{measured}) and the tabulated values is shown ($E_{\text{tabulated}}$, taken from Ref.). This quantity was calculated as $(E_{\text{measured}} - E_{\text{tabulated}})/E_{\text{tabulated}}$ and the values are all less than 1%.

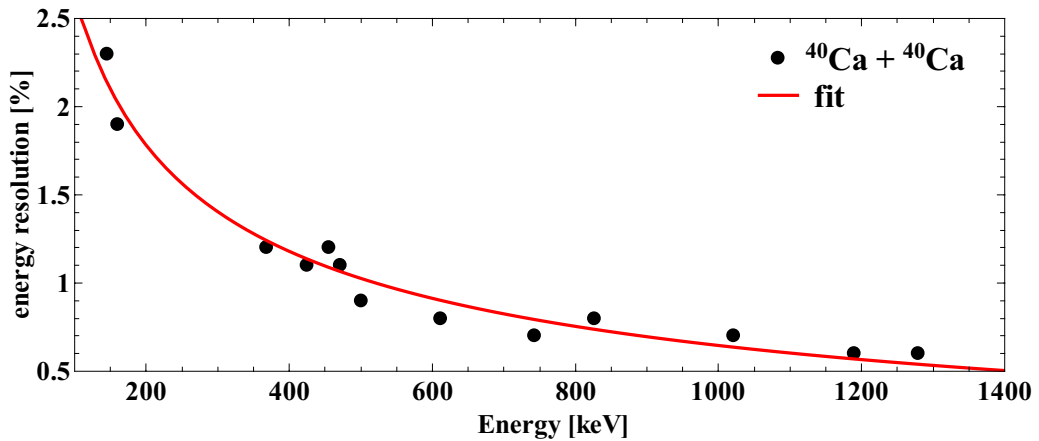


Figure 3.6: Energy resolution trend obtained in the reaction $^{40}\text{Ca} + ^{40}\text{Ca}$ studying the much more intense low-energy γ transitions. The experimental data follow the expected $E^{-1/2}$ trend (red line).

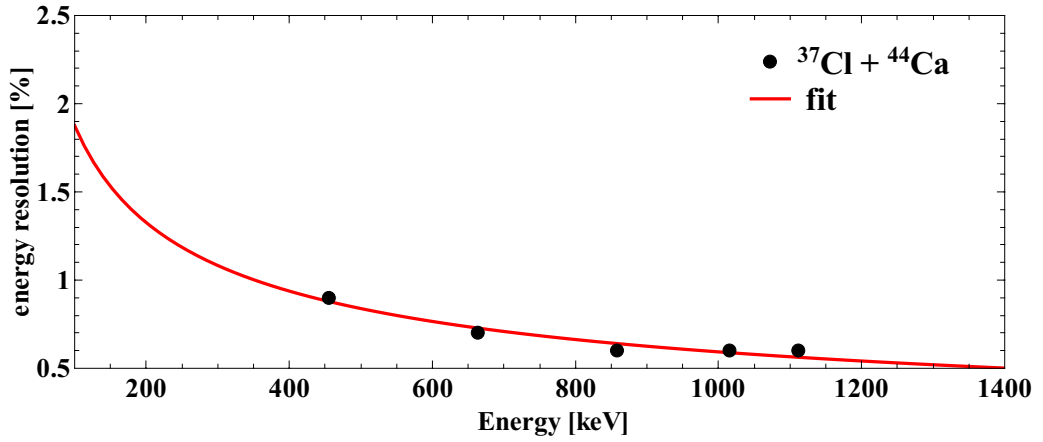


Figure 3.7: Energy resolution trend obtained in the reaction $^{37}\text{Cl} + ^{44}\text{Ca}$ studying the much more intense low-energy γ transitions. The experimental data follow the expected $E^{-1/2}$ trend (red line).

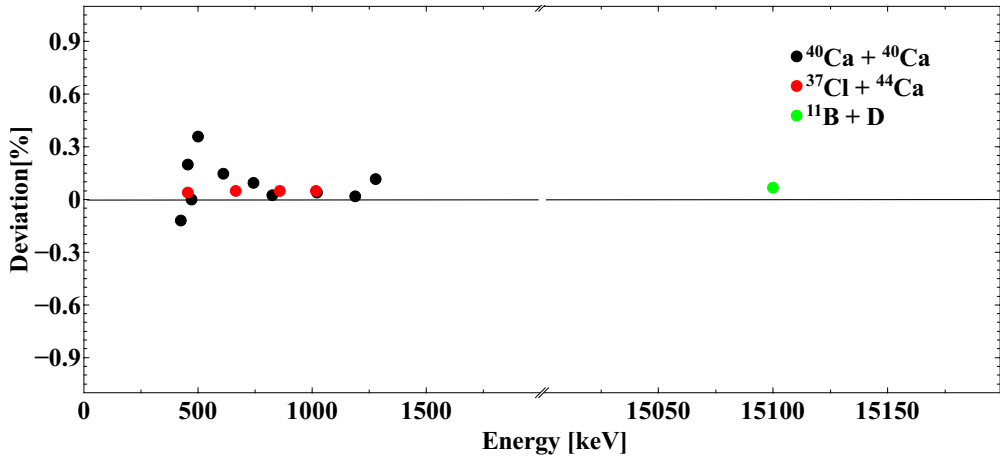


Figure 3.8: Deviation between measured γ -ray energy and the tabulated values is shown. The dots are related to $^{40}\text{Ca} + ^{40}\text{Ca}$ (black dots), $^{37}\text{Cl} + ^{44}\text{Ca}$ (red dots) and $^{11}\text{B} + \text{D}$ (green dot) reaction.

3.2 HECTOR⁺

3.2.1 Time resolution

For each LaBr₃:Ce detector a time spectrum was acquired during the experiment. The time information was provided to a TDC (*Time to Digital Converter*) by a CFD (*Constant Fraction Discriminator*). All TDC had as START signal the Master-Gate signal (as defined in Chapter 2), while as STOP signal they had the CFD signal (after a delay). The time calibration was performed using a ⁶⁰Co source.

In Fig.3.9, it is shown the time spectrum of one LaBr₃:Ce detector without any condition on the data. It is clear that the spectrum is composed by the superposition of several structures, which can be easily identify adding the trigger conditions in the sort procedure (as shown in Fig.3.10).

The main structure of the spectrum (FWHM \approx 20 ns) was originated by the events with the AGATA& LABR trigger condition (the width is so large because the START signal came from the AGATA detector). The narrow peaks (FWHM \approx 2 ns), at around 75 ns and 85 ns, were originated by the LaBrM2 trigger condition. These events were characterized by an optimum time resolution. The spike presents at 70 ns is the auto-coincidence peak.

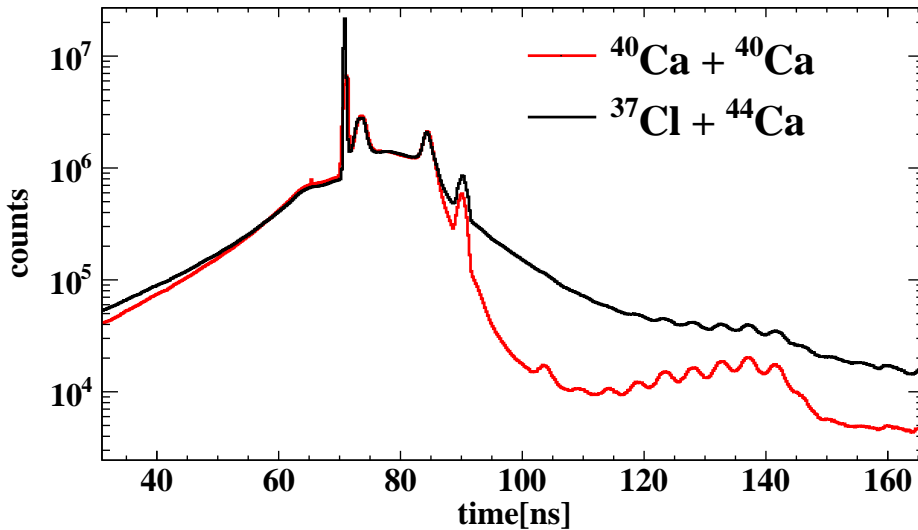


Figure 3.9: Time spectrum of one LaBr₃:Ce obtained without any condition in the sort. Several structure are visible.

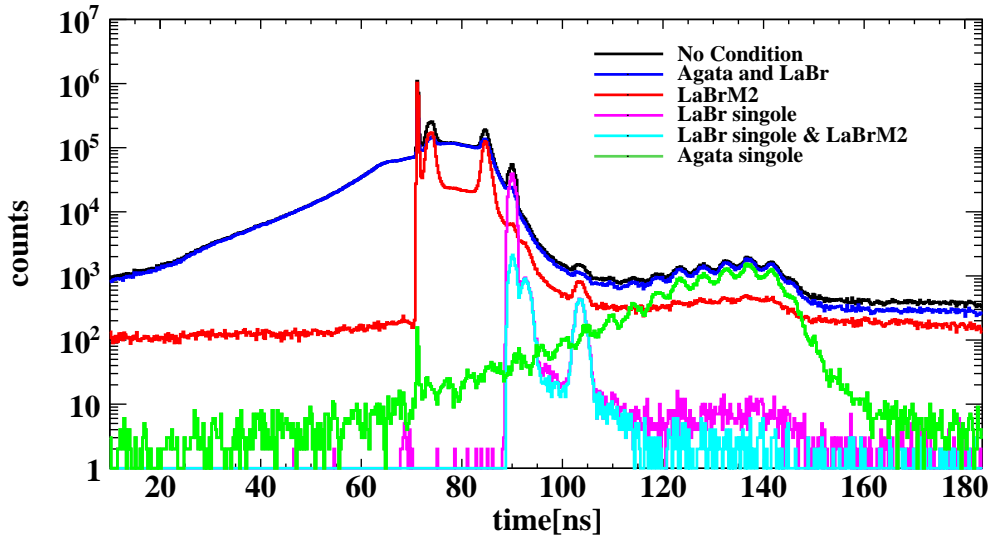


Figure 3.10: Time spectra of one $\text{LaBr}_3\text{:Ce}$ correspond to different trigger conditions. In this way, it is clear the origin of the structure in Fig 3.1.

3.2.2 Energy resolution and linearity

$\text{LaBr}_3\text{:Ce}$ detectors are calibrated using γ -ray sources (^{60}Co , ^{137}Cs , ^{133}Ba , ^{188}Y) and the data acquisition was performed before and after the experiment. Thanks to this double check, it was possible to verify that the detectors remained stable along to all the experiment.

The Doppler correction was performed in order to have the energy spectra in the center of mass system. The detector positions were measured before the experiment, while the β value was the same as the value found with AGATA. Fig.3.11 and Fig.3.12 show the spectra before and after Doppler correction. The energy resolution follows the expected $E^{-1/2}$ trend (see Fig.3.13 and Fig.3.14) and the deviation remain smaller than 1% (see Fig.3.15).

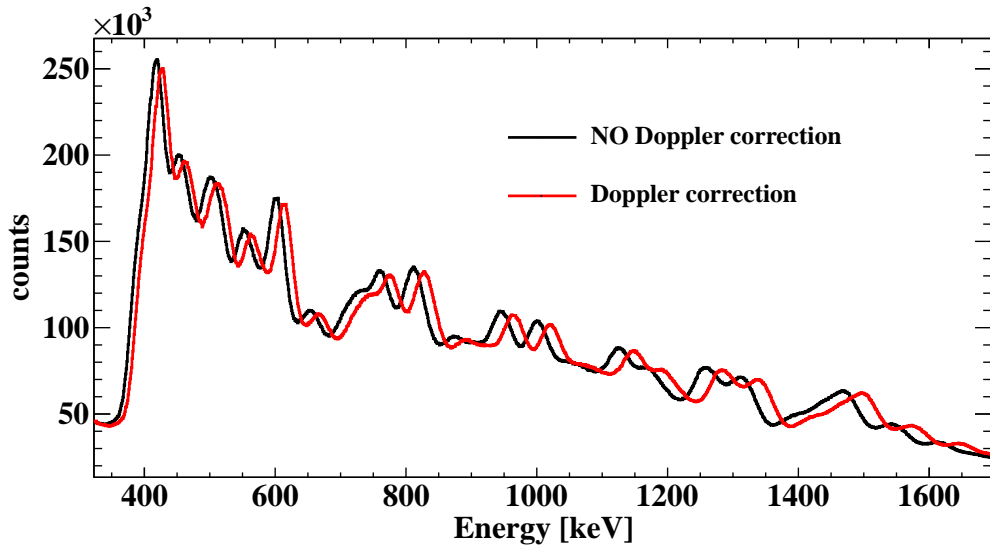


Figure 3.11: Energy spectrum of all LaBr₃:Ce in the reaction $^{40}\text{Ca} + ^{40}\text{Ca}$. The black line was obtained without the Doppler correction. The red line was obtained performing the Doppler correction.

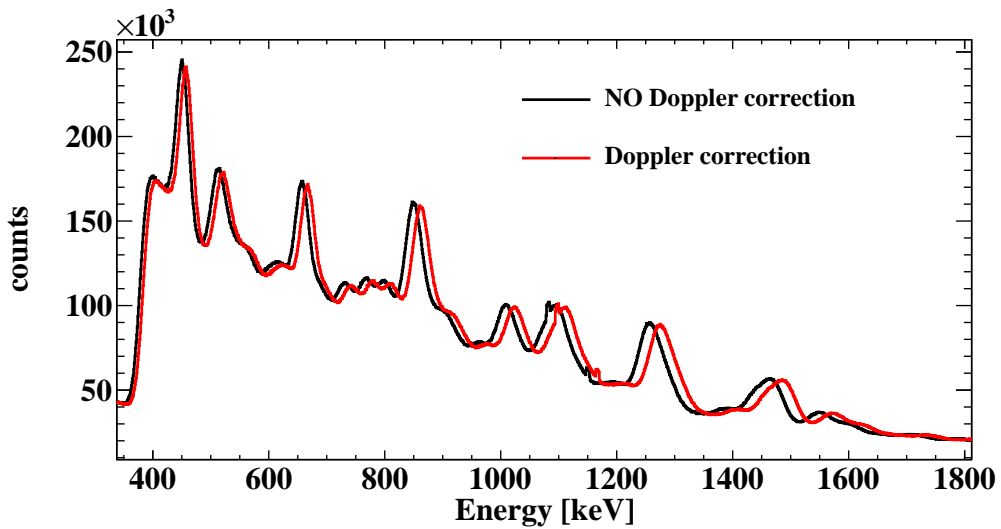


Figure 3.12: Energy spectrum of all LaBr₃:Ce in the reaction $^{37}\text{Cl} + ^{44}\text{Ca}$. The black line was obtained without the Doppler correction. The red line was obtained performing the Doppler correction.

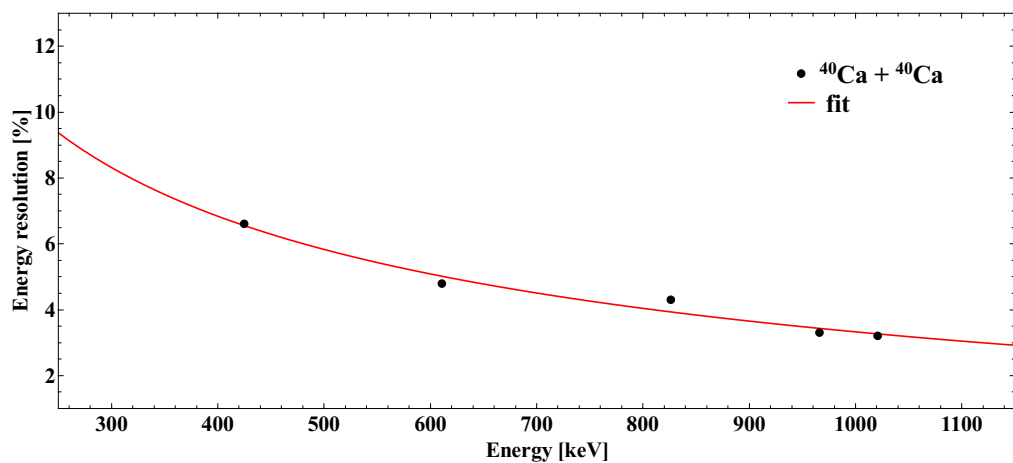


Figure 3.13: Energy resolution trend obtained in the reaction $^{40}\text{Ca} + ^{40}\text{Ca}$ studying the much more intense low-energy γ transitions. The experimental data follow the expected $E^{-1/2}$ trend (red line).

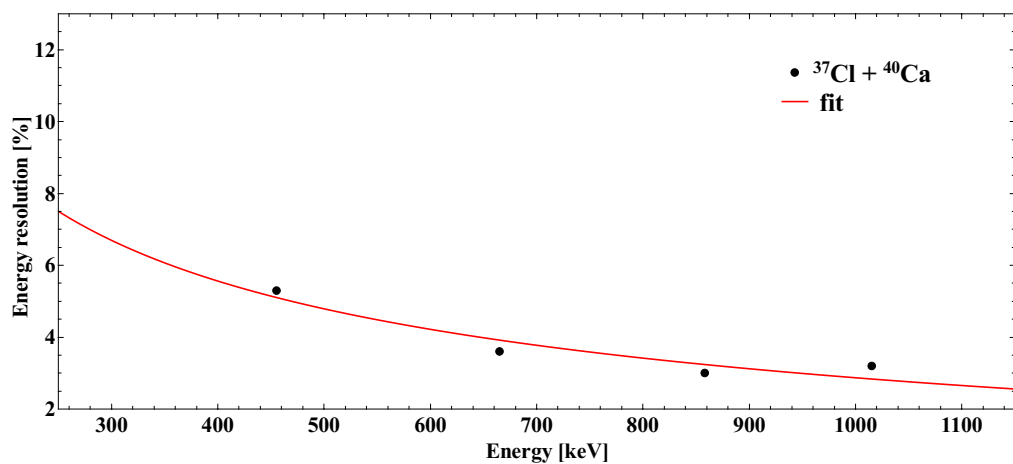


Figure 3.14: Energy resolution trend obtained in the reaction $^{37}\text{Cl} + ^{40}\text{Ca}$ studying the much more intense low-energy γ transitions. The experimental data follow the expected $E^{-1/2}$ trend (red line).

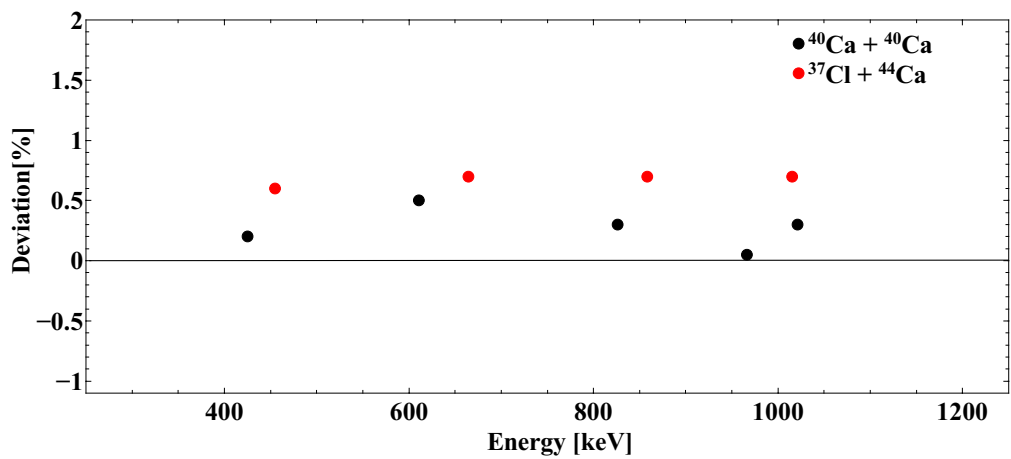


Figure 3.15: Deviation between measured γ -ray energy and the tabulated values is shown. The dots are related to $^{40}\text{Ca} + ^{40}\text{Ca}$ (black dots), $^{37}\text{Cl} + ^{44}\text{Ca}$ (red dots) reaction.

3.3 Multiplicity response

As explained in Chapter 1, in a fusion reaction, the CN spin distribution can be measured counting the number of γ -rays emitted in the decay, the so-called γ -ray multiplicity (M_γ). Obviously, the number of γ -rays measured in the apparatus (the so-called γ -ray fold, F_γ) is always less than M_γ , because of the efficiency of the apparatus. Different F_γ correspond to a different M_γ distribution and thus to a different CN spin distribution. Since the spin distribution is a fundamental input for the statistical model used in the analysis, it is important to know the conversion between F_γ and M_γ of the apparatus.

The relation between M_γ and F_γ was calculated using a simple recursive algorithm proposed by Holm [98]. This algorithm calculates the probability $P(F_\gamma, M_\gamma)$ of measuring F_γ γ -rays using N detectors and with a cascade of M_γ γ -rays. As input, it is used the experimentally pre-determined total efficiency Ω of the apparatus and the intra-detector scattering probability ξ :

$$P(F_\gamma, M_\gamma) = a_F P(F_\gamma, M_\gamma - 1) + b_F P(F_\gamma - 1, M_\gamma - 1) + c_F P(F_\gamma - 2, M_\gamma - 1) \quad (3.4)$$

with:

$$a_F = 1 - (N - F_\gamma)\omega(1 + \xi \frac{F_\gamma}{N - 1}) \quad (3.5)$$

$$b_F = (N - F_\gamma + 1)\omega(1 - \xi \frac{N - 2F_\gamma + 1}{N - 1}) \quad (3.6)$$

$$c_F = (N - F_\gamma + 2)\omega\chi \frac{N - F_\gamma + 1}{N - 1} \quad (3.7)$$

$$(3.8)$$

$P(F_\gamma, M_\gamma) = 0$ for $F_\gamma < 0$ or $M_\gamma < 0$, $P(0, 0) = 0$. The efficiency of each detector of the apparatus is ω , i.e. $N\omega = \Omega$. In our case we neglected the scattering probability ξ , i.e. $\xi = 0$.

$P(F_\gamma, M_\gamma)$ was calculated for a γ -ray energy of ~ 1.2 MeV (which is the γ -transition energy of the ^{60}Co source). The efficiencies of AGATA Demonstrator and HECTOR⁺ were calculated in two ways: with a Monte-Carlo simulation (using GEANT4 libraries [97]) and with ^{60}Co source.

The latter method consisted in using AGATA Demonstrator as trigger and the events are considered only if the 1.33 MeV γ ray from the ^{60}Co source results in a full energy peak, ensuring that exactly one gamma-ray of 1.17 MeV is presented in the array.

Experiment			Simulation	
	AGATA	HECTOR ⁺	AGATA	HECTOR ⁺
ϵ_{ph}	3%	2%	4%	2%
ϵ_{riv}	7%	5%	9%	4%

Table 3.2: Values of photo-peak efficiency (ϵ_{ph}) and total efficiency (ϵ_{riv}) are reported in the table for both detectors. In the left side of the table the experimental value of the efficiencies are reported, while in the right side the values obtained with simulations are reported. See the text for the details.

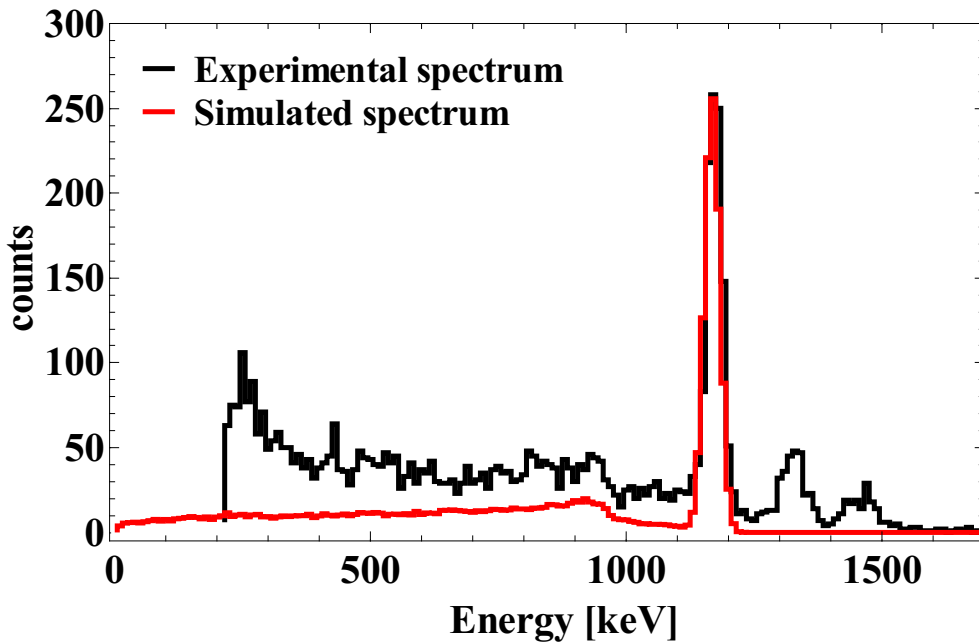


Figure 3.16: Simulated and experimental spectra for a 1.1 MeV γ -ray are shown. The experimental spectrum (obtained as explained in the text) has a visible background contribution at low energy.

In addition, the total number of measured 1.17 MeV γ rays is equal to the area of the 1.33 MeV full energy peak (we assumed that the efficiency for a γ ray of 1.17 MeV and 1.3 MeV could be the same). This trick is necessary when one does not know the activity of the source.

The results obtained with this method are reported in Table 3.2 in comparison with the simulated values. In the case of $\text{LaBr}_3 : \text{Ce}$ one should remember the presence of low-energy background: as shown in Fig.3.16, there is a difference in the low-energy

part of the spectrum between the simulated spectrum and the experimental spectrum. After a background subtraction the total efficiency value that we obtained is $\sim 5\%$, which is in agreement with the simulation.

In the analysis of this experiment, the experimental efficiency of AGATA Demonstrator was used as input of Formula 3.4; on the other hand the simulated efficiency of HECTOR⁺ was used in the calculations.

The $P(F_\gamma, M_\gamma)$ distributions are shown in Fig.3.17 (for AGATA) and in Fig.3.18 (for HECTOR⁺). To be noted that the granularity of the two detectors is very different: 12 HpGe detectors in AGATA and 7 detectors in HECTOR⁺.

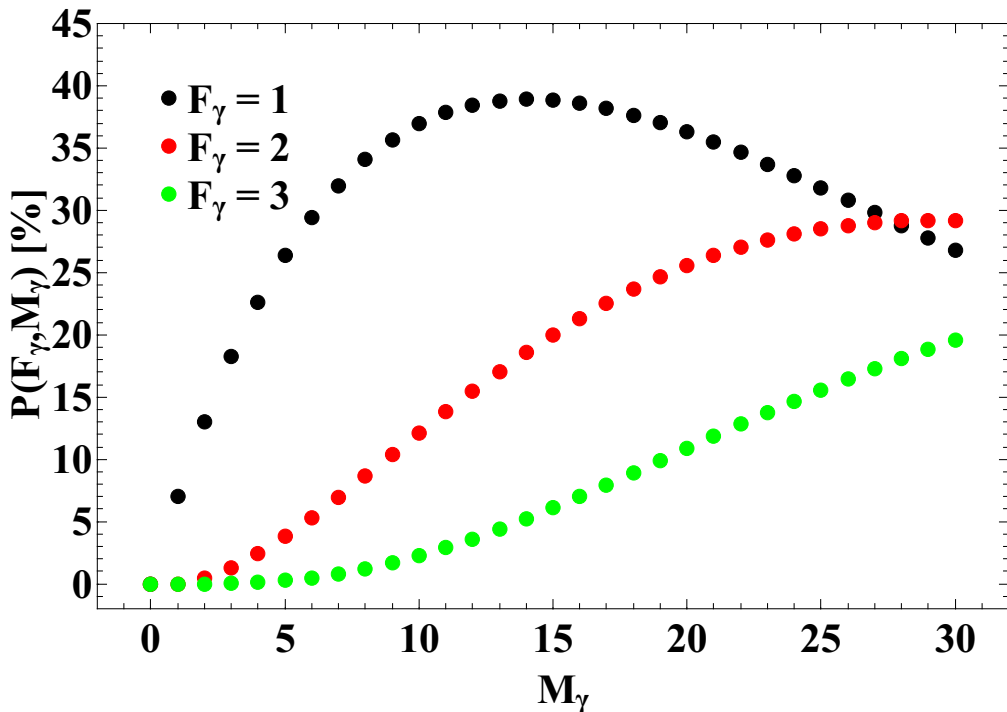


Figure 3.17: Probability distribution $P(F_\gamma, M_\gamma)$ of triggering F_γ in AGATA Demonstrator by a cascade of M_γ γ -rays. Three F_γ conditions are considered. A total efficiency $\epsilon_{riv} = 7\%$ was considered in the calculations.

Since the detection of a γ -ray in AGATA Demonstrator is statistically independent on the detection of another γ -ray in HECTOR⁺, the probability distribution $P(F_\gamma, M_\gamma)$ associated to a trigger condition corresponding to a coincidence between AGATA and HECTOR⁺ was obtained multiplying the $P(F_\gamma, M_\gamma)$ of the two detectors. In Fig. 3.19 the probability distribution for three different trigger conditions is shown.

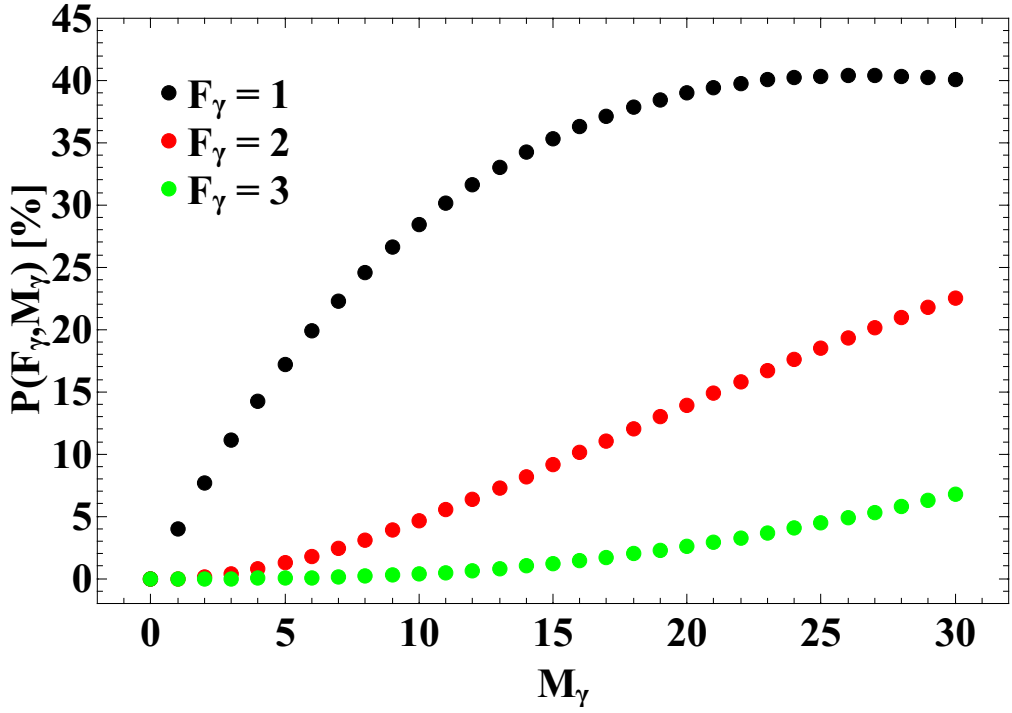


Figure 3.18: Probability distribution $P(F_\gamma, M_\gamma)$ of triggering F_γ in HECTOR⁺ by a cascade of M_γ γ -rays. Three F_γ conditions are considered. A total efficiency $\epsilon_{riv} = 4\%$ was considered in the calculations.

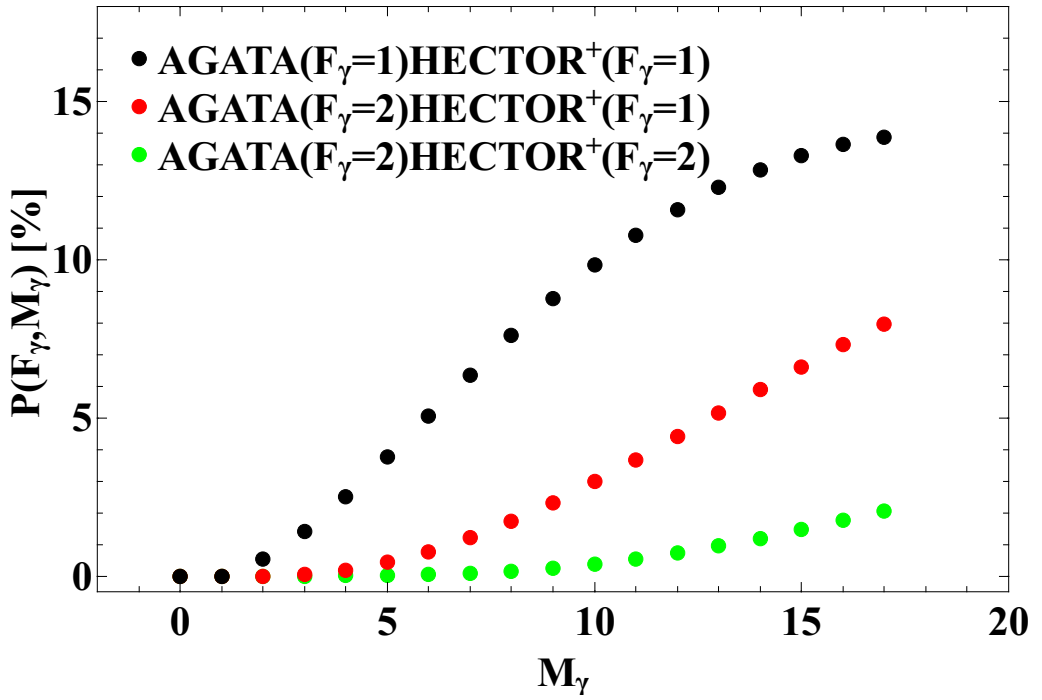


Figure 3.19: Probability distribution $P(F_\gamma, M_\gamma)$ of triggering a coincidence between AGATA Demonstrator and HECTOR⁺ by a cascade of M_γ γ -rays. Three trigger conditions are considered.

3.4 HECTOR⁺ response function

The absolute photo-peak efficiency of HECTOR⁺ array in this configuration is $\sim 2\%$ at 1 MeV, but it is $\sim 0.3\%$ at 15 MeV . The deformation of the γ -ray spectrum emitted by the CN induced by the detection process (i.e. response function) is shown in Fig.3.20. In order to have a correct comparison between the detected γ -ray spectrum and the simulated one, the latter must be folded with the response function of the detector, following a standard procedure as reported in [99].

For this purpose we simulated the γ -ray interaction in the detectors starting from 1 MeV γ ray up to 32 MeV, obtaining 32 simulated spectra. These spectra were considered as columns of a 32×32 matrix, where each element of the matrix (E_{det}, E_γ) is the number of γ detected with E_{det} energy when a γ ray with an energy of E_γ interacts.

This matrix (called A) represents the response function of the detector. Indeed, if v is the incoming γ ray spectrum and w is the real detected spectrum, it is possible write the relation:

$$w = A * v \quad (3.9)$$

where the symbol $*$ represent the vector product. The dashed curve in Fig.3.20 was obtained using this procedure.

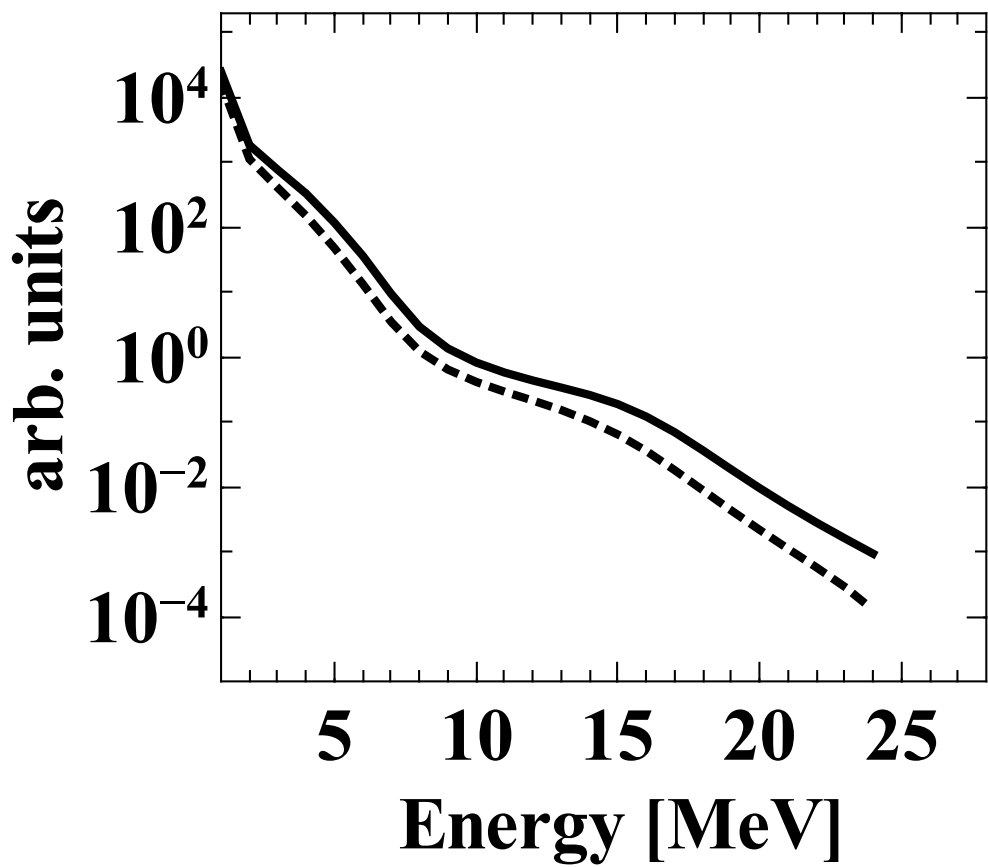


Figure 3.20: CN γ -decay spectrum obtained with CASCADE code before (solid line) and after (dashed line) the application of the response function.

Results and discussion I

The data analysis was mainly based on three steps: i) the first consists to check that the statistical model CASCADE [100,101] correctly reproduces the measured residual nuclei distribution; ii) the second concerns in the statistical model analysis of the ^{81}Rb γ -ray spectrum to deduce the GDR parameters; and iii) the last consists in the analysis of the ^{80}Zr spectrum to deduce the isospin mixing as the only free parameter.

As reported in the Chapter 1, the analysis method that we use is based on the assumption that the statistical model parameters used to describe the γ decay of ^{81}Rb and ^{80}Zr have the same features. The conditions that, if fulfilled, guarantee the validity of this assumption are that the average CN temperature, mass and shape are similar. As a consequence the GDR parameters used to describe the statistical decay (centroid, width and strength) will be the same. The condition on mass is satisfied by choosing two CN with $A=81$ and 80 , respectively, that can be assumed as equal in the description of statistical decay from hot nuclei.

In this Chapter, we will present preliminary calculations showing that the conditions on temperature and shape are satisfied to a very good extent by the systems we have chosen, i.e. the GDR parameters of ^{81}Rb and ^{80}Zr are expected to be practically the same.

Since the largest part of the data is characterized by a coincidence between AGATA and HECTOR⁺, the data analysis was concentrated on this class of events.

4.1 Kinematics of reaction

The internal energy of the CN can be calculated according to Eq. 4.2:

$$E_{int}(E^*, J) = E^* - E_{rot}(J) = \quad (4.1)$$

$$= \frac{A_{target}}{A_{pro} + A_{target}} E_{beam} + Q - E_{rot}(J) \quad (4.2)$$

where A is the mass number of nucleus (projectile or target), E_{beam} is the beam energy corrected for energy loss in the target, Q is the Q -value of the reaction and $E_{rot}(J)$ is the rotational energy after the formation of the CN.

In the discussed experiment the beam energies have been chosen in order to match E_{int} (calculated with Eq. 4.2) after correcting E_{lab} for energy loss in the target, as shown in Tab. 4.2. The beam was delivered by the TANDEM accelerator.

reaction	E_{lab} (MeV)	E_{loss} (MeV)	t ($\mu g/cm^2$)	Q (MeV)	E^* (MeV)	σ (mb)
$^{40}\text{Ca} + ^{40}\text{Ca}$	136	7	500	-14	54	500
$^{37}\text{Cl} + ^{44}\text{Ca}$	95	6	500	2	54	250

Table 4.1: E_{lab} is the energy of the incoming beam, E_{loss} is the energy loss in the target of thickness t , calculated with LISE++ code, Q is the Q -value of the reaction calculated with PACE4, E^* is the excitation energy calculated with Eq. 4.2, σ is the fusion cross section calculated according to Bass Model with PACE4 code.

As explained in Chapter 1, the nuclear temperature (T) is a fundamental quantity for the description of the CN system. Moreover, the GDR width depends on this quantity and thus it is important to verify if the temperature is the same for both reactions. The temperature of the CN is defined as:

$$T(J) = \sqrt{\frac{E_{int}(J)}{a(A, E_{int}, J)}} \quad (4.3)$$

where $E_{int}(E^*, J) = E^* - E_{rot}(J)$ is the internal energy of the system and $a(A, E_{int}, J)$ is the level density parameter, calculated using the Reisdorf parametrization.

In order to calculate $E_{rot}(J)$ and, therefore, the internal energy of the CN, one has to perform an average on the rotational energy as a function of spin J (the yrast line displayed in Fig.4.1 in our systems) using the spin distribution as a weight (see Fig.4.2).

In our calculation we have adopted the Rotating Liquid Drop Model yrast line used within GEMINI++ Statistical Model calculation. Since the CN can be formed at different angular momenta, it fills different temperatures. For this reason, it is useful to introduce

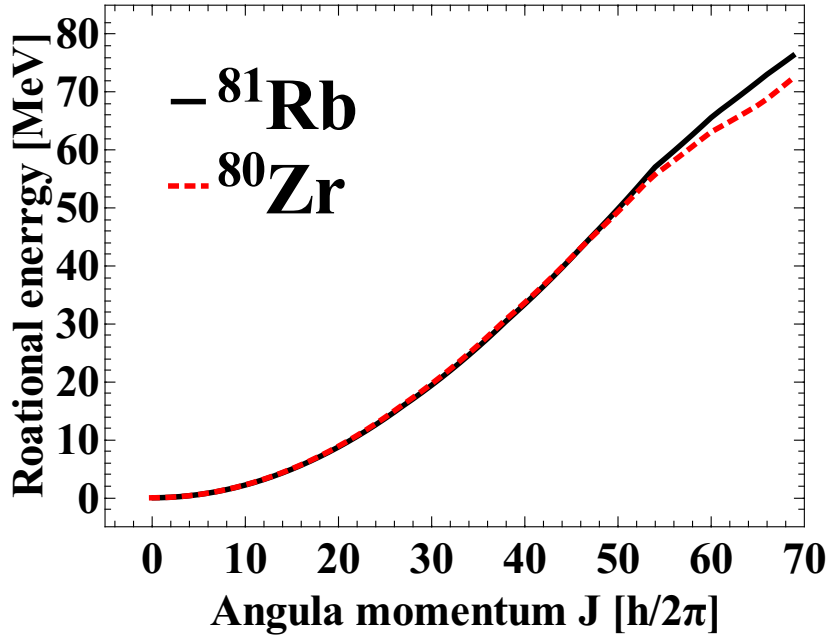


Figure 4.1: Yrast-line calculated with the GEMINI++ Statistical Model, using the Lublin-Strasbourg Liquid Drop (LSD) model.

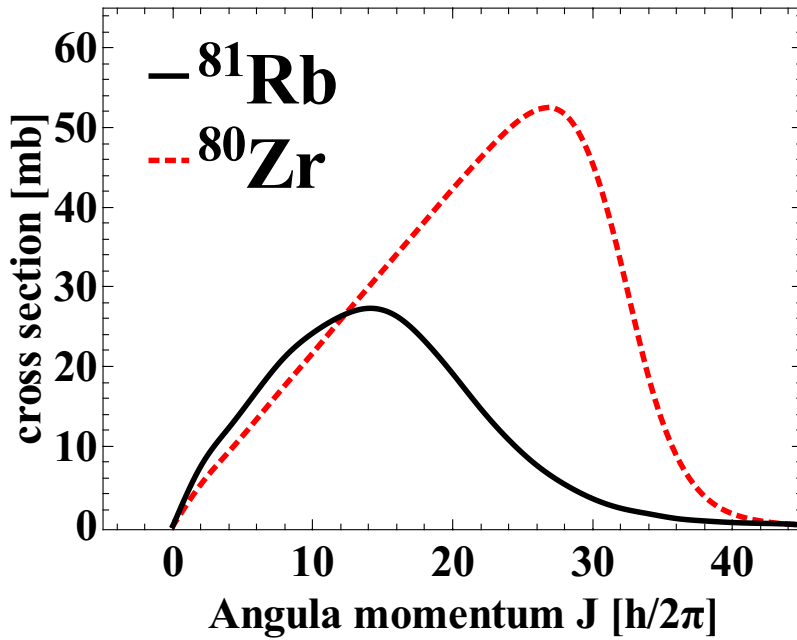


Figure 4.2: spin distribution of the fusion cross section for both nuclei.

a mean value of the temperature $\langle T(J) \rangle$, corresponding to the temperature value at the mean value of the angular momentum distribution $\langle J \rangle$. It means that $\langle T(J) \rangle = T(\langle J \rangle)$.

In Table 4.2 the mean value of the temperature and the angular momentum are reported.

Although the spin distributions are different, the kinematic of the reaction allow to have similar temperature for both reactions.

CN	$\langle J \rangle (\hbar)$	$\langle E_{rot} \rangle (\text{MeV})$	$\langle T \rangle (\text{MeV})$
^{80}Zr	21	10	2.0
^{81}Rb	15	5	2.1

Table 4.2: mean values of angular momentum $\langle J \rangle$, rotational energy $\langle E_{rot} \rangle$ and temperature $\langle T \rangle$ are reported.

As explained in the previous chapter, the spin distribution changes with the number of γ -rays detected (F_γ) in the array (therefore also the rotational energy changes). The larger part of the acquired events are related to $F_\gamma = 2$ (1 γ -ray detected in AGATA and 1 γ -ray detected in HECTOR⁺). For this reason our analysis was concentrated on this class of events. The spin distributions associated to this fold condition are shown in Fig.4.3. These spin distributions were obtained using the $P(F_\gamma, M_\gamma)$ distributions obtained in the previous chapter.

Since the rotation energy changes with the F_γ , the temperature felt by the CN changes as well. In Table 4.3 the features of this class of events are summarised. Also in this case the temperature values are similar.

CN	$\langle J \rangle (\hbar)$	$\langle E_{rot} \rangle (\text{MeV})$	$\langle T \rangle (\text{MeV})$
^{80}Zr	25	13	1.9
^{81}Rb	17	6	2.1

Table 4.3: mean values of angular momentum $\langle J \rangle (\hbar)$, $\langle E_{rot} \rangle$ and temperature of $F_\gamma = 2$ events are reported.

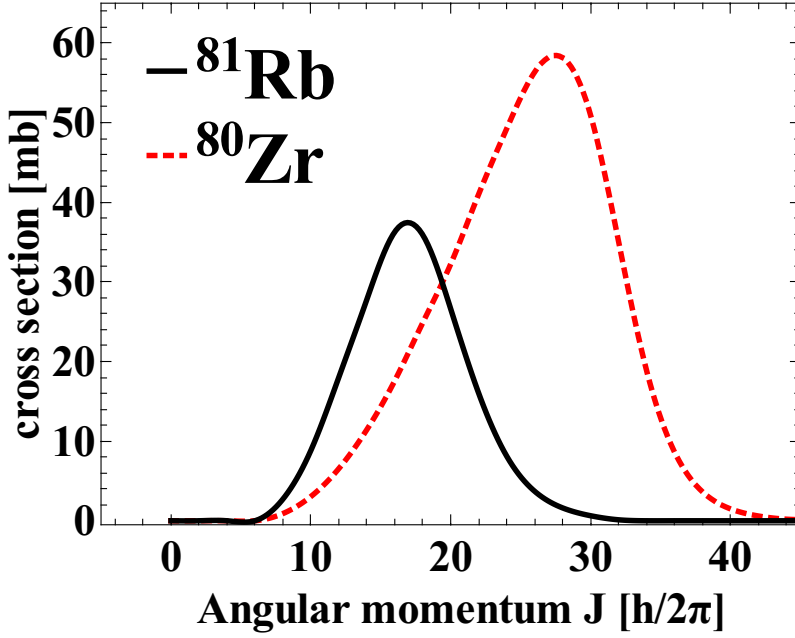


Figure 4.3: spin distribution related to $F_\gamma = 2$ events.

4.2 CN particle decay

4.2.1 Neutron emission

The neutrons interact in the crystal via several reactions, which can distort the γ -ray spectra detected and thus they must be rejected in the analysis, especially when the physical observable is small (as in the case of the isospin mixing in $^{40}\text{Ca} + ^{40}\text{Ca}$ reaction).

The ^{80}Zr nucleus lies in the neutron-deficient region of the Segrè chart, while the ^{81}Rb is in the stability valley (see Fig.4.4). For ^{80}Zr the neutron separation energy is so high (~ 16 MeV) that the neutron emission is strongly inhibited. On the other hand, ^{81}Rb nucleus is far to the proton drip-line and the neutron emission is expected to be dominant.

The presence of neutrons can be observed in the time spectrum. Indeed, the neutron events are delayed because the neutrons have a smaller velocity than the γ rays.

The neutron contribution is clearly visible in the time spectrum of $^{37}\text{Cl} + ^{44}\text{Ca}$ reaction (black line) at ≈ 100 ns (the γ -ray peak is placed at ≈ 90 ns). On the other hand, no neutron peak is present in the $^{40}\text{Ca} + ^{40}\text{Ca}$ time spectrum, as expected.

In Fig.4.6 it is shown the energy spectrum and the associated time spectrum of the

neutrons emitted by ^{81}Rb . The energy spectrum was obtained using the PACE4 code. The time spectrum was obtained converting the neutron kinetic energy in the neutron velocity and considering the time needed to a neutron to travel 25 cm (distance of HECTOR⁺) respect to a γ -ray. The energy distribution is peaked at ≈ 3 MeV, while the associated time distribution is peaked at ≈ 10 ns. The latter value is in good agreement with that we found observing the time spectrum in Fig.4.5.

It is worth to be noted that the absence of neutrons in the reaction means that no neutron background is present. As the evaporated charge particles are stopped by the scattering chamber, we do not expect particles induced background in ^{80}Zr γ -ray spectrum. This is an important point when one wants to measure a small effect as the isospin mixing.

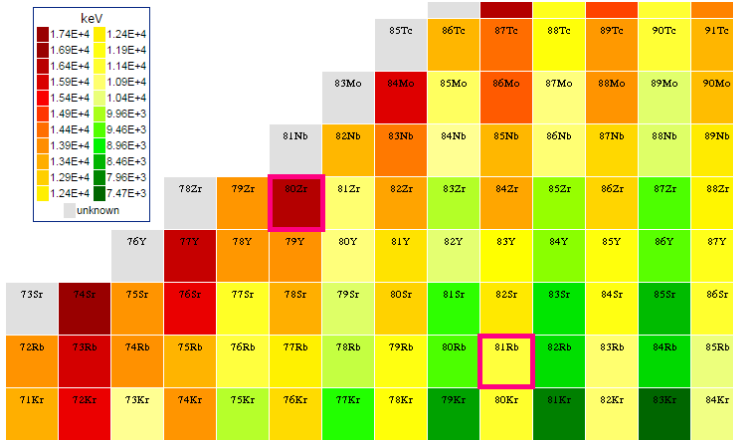


Figure 4.4: Region of nuclear chart where ^{80}Zr and ^{81}Rb lies. The color code represent the neutron separation energy. The large separation energy should inhibit the neutron decay of ^{80}Zr

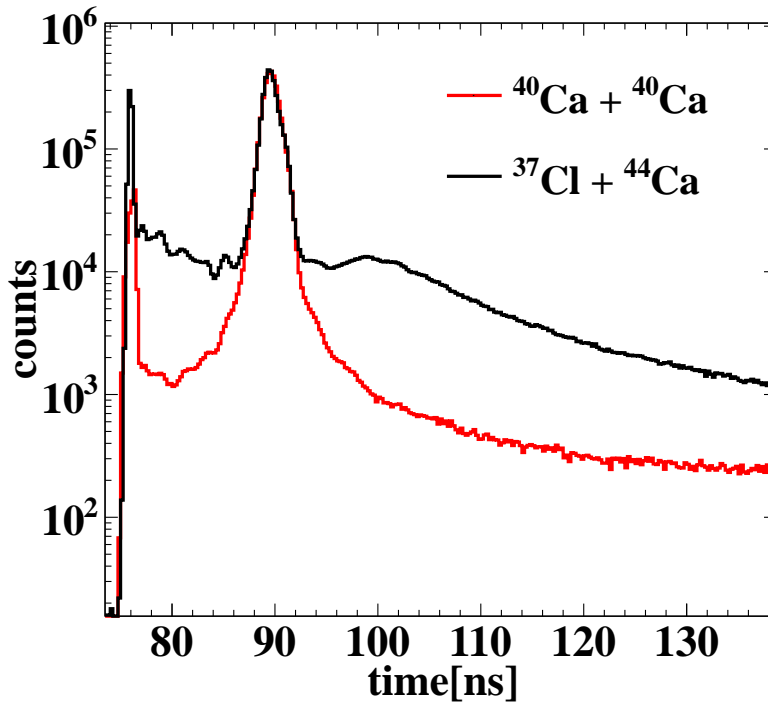


Figure 4.5: Time spectra of LaBr₃:Ce detector for both reactions, in the case of LaBr events. In $^{37}\text{Cl} + ^{44}\text{Ca}$ reaction the neutron contribution is clearly visible. On the other hand, in $^{40}\text{Ca} + ^{40}\text{Ca}$ reaction there is not evidence of the presence of neutrons.

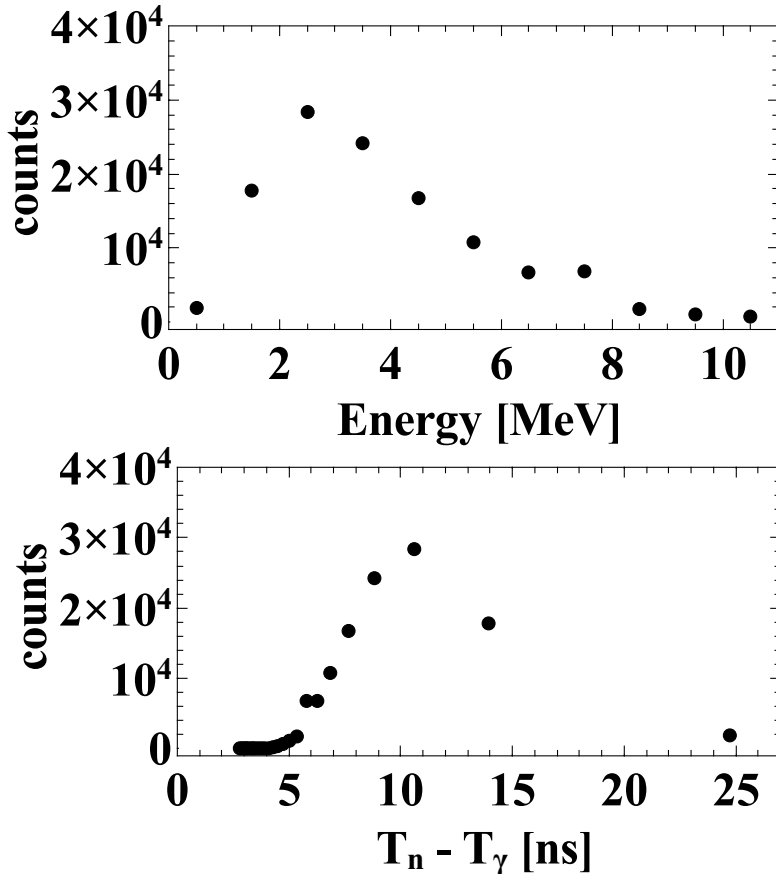


Figure 4.6: Top panel: simulated energy spectrum of neutrons emitted by ^{81}Rb in the cooling process. Bottom panel: time spectrum of neutrons emitted by ^{81}Rb and detected by HECTOR⁺. In the x-axis it is plotted the difference between the detection time of neutrons and γ .

4.2.2 Residues population

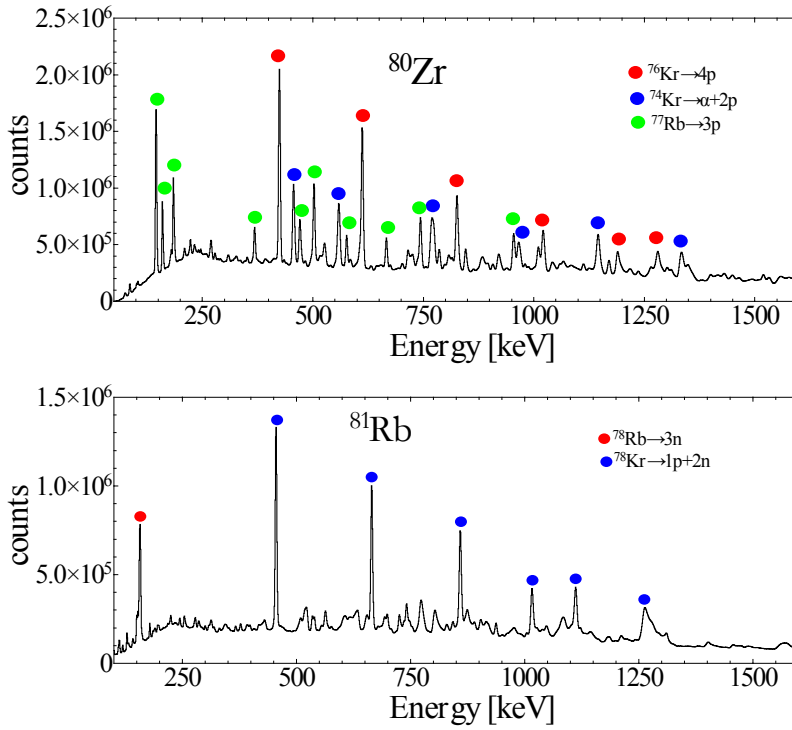


Figure 4.7: The low-energy spectra of the AGATA Demonstrator are shown. The top panel is related to the ^{80}Zr decay, while the bottom panel is related to the ^{81}Rb decay. The circles represent the transitions of the more populated residues. The spectra were obtained without any conditions in the sort code.

The compound nucleus emits mainly particles until the the excitation energy remains above the particle separation energy, then it can decay only via γ -ray emission. The nuclei populated after the particle decay process are called residue nuclei.

The γ rays associated to the low-energy transitions of the residue nuclei were detected using the AGATA Demonstrator. These discrete transitions were used to identify the residue and to extract, using their intensity, the CN populated residue population.

In Fig.4.7 the γ -ray spectra of the AGATA Demonstrator are shown. The main intense peaks were identified, using the RADWARE archive as reference. The residue population can be extracted also using the statistical model. The comparison between the experimental and the simulated population distribution is an excellent tool to check the validity of the statistical model predictions.

In particular, we have preformed two different checks: i) evaluation of the variation

of the residue population as a function of coincidence fold (and thus for different spin distribution, as explained in Chapter 3); ii) the evaluation of the residues distribution as a function of the γ -ray energy detected in HECTOR⁺. In both cases the variation of the residues population is originated by the change of the phase-space available for particle emission.

The residue population extracted using the AGATA Demonstrator as a function of the γ -ray energy detected in HECTOR⁺ is shown in Fig. 4.8. The experimental data were corrected by the AGATA Demonstrator efficiency. The statistical model calculation was performed using a Monte-Carlo version of the CASCADE code. In Fig. 4.8 and Fig.4.9, one can clearly see that the ⁷⁷Rb residue (3p emission) is strongly populated in coincidence with a high-energy γ ray (in the GDR region); on the other hand the ⁷⁶Kr residue is mainly populated in coincidence with the emission of low-energy γ rays. This fact reflects two different regions of the phase space; indeed, gating on an high-energy γ -ray less phase-space is available for particle emission and thus the residue with less particles emitted is favorite. In general the three most strongly populated residual nuclei (⁷⁶Kr, ⁷⁴Kr and ⁷⁷Rb) are found to be rather well reproduced by the statistical model.

The variation of the residues population as a function of the F_γ detected in HECTOR⁺ and AGATA Demonstrator is shown in Fig. 4.8. The spin distribution used in the statistical model calculation was corrected using the response function calculated in Chapter 3. From Fig. 4.8 and Fig.4.11, one can clearly see that the ⁷⁷Rb residue (3p emission) is strongly populated in coincidence with a high-energy γ ray (in the GDR region); on the other hand the ⁷⁶Kr residue is mainly populated in coincidence with the emission of a low-energy γ ray. Also in this case, this fact reflects the population of different regions of the phase space; indeed, the $F_\gamma = 4$ trigger request corresponds to a higher mean spin value than $F_\gamma = 2$ and thus the phase-space is smaller in the latter case.

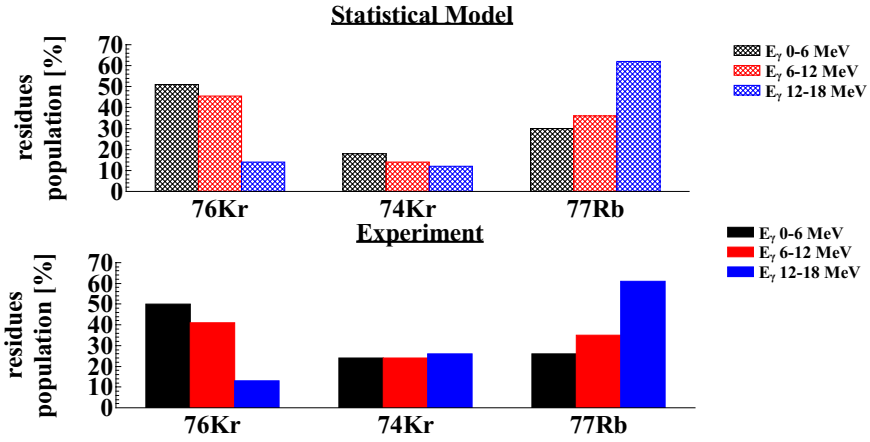


Figure 4.8: Residues population obtained from the analysis of the AGATA Demonstrator spectrum as a function of the energy detected in HECTOR⁺ array. The experimental data was corrected by the AGATA Demonstrator efficiency. The statistical model calculation was performed using a Monte-Carlo CASCADE code.

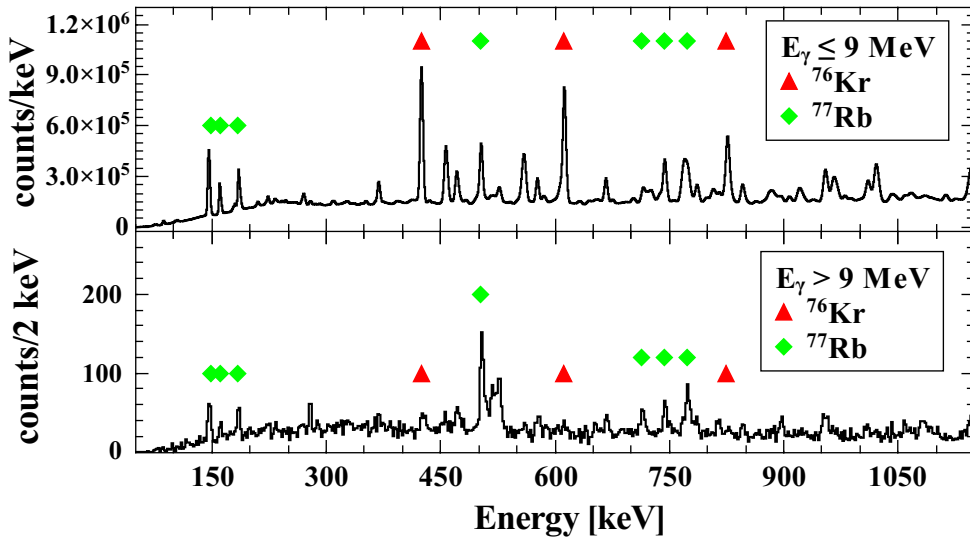


Figure 4.9: Energy spectra of AGATA Demonstrator in the reaction $^{40}\text{Ca} + ^{40}\text{Ca}$ related to two different conditions: (top panel) when a $E_\gamma < 9$ MeV γ -ray was detected in HECTOR⁺; (bottom panel) when a $E_\gamma > 9$ MeV γ -ray was detected in HECTOR⁺.

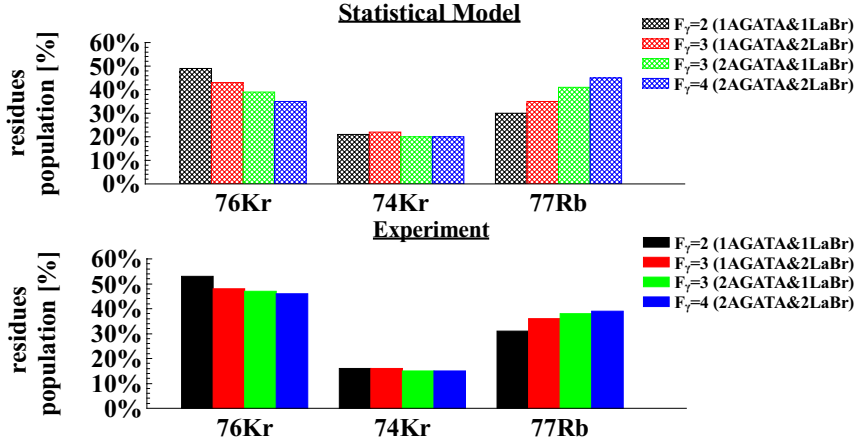


Figure 4.10: Residues population obtained from the analysis of the AGATA Demonstrator spectrum as a function of the fold request. The experimental data was corrected by the AGATA Demonstrator efficiency. The statistical model was performed using a CASCADE code, where the spin distribution in input was weighed by the associated response function.

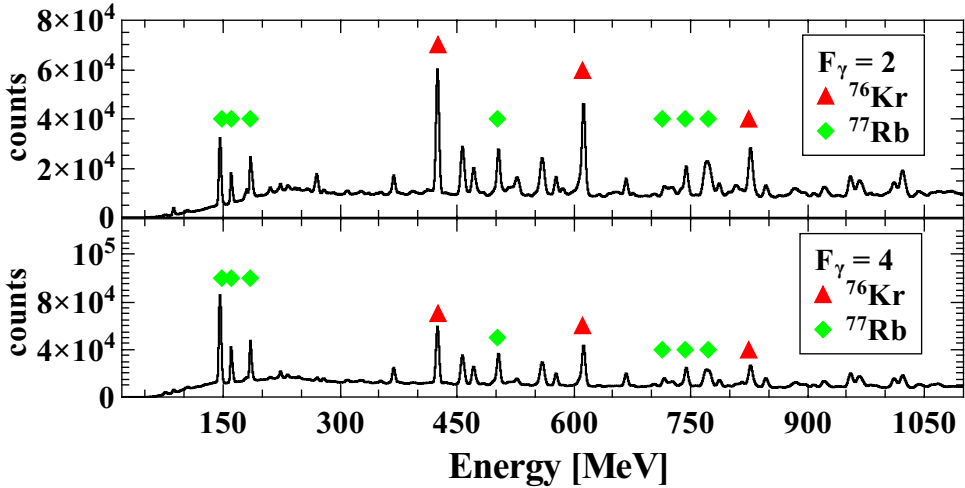


Figure 4.11: Energy spectra of AGATA Demonstrator in the reaction $^{40}\text{Ca} + ^{40}\text{Ca}$ related to two different conditions: (top panel) when a $F_\gamma = 2$ event was detected in HECTOR⁺; (bottom panel) when a $F_\gamma = 4$ event was detected.

4.3 High-energy spectra

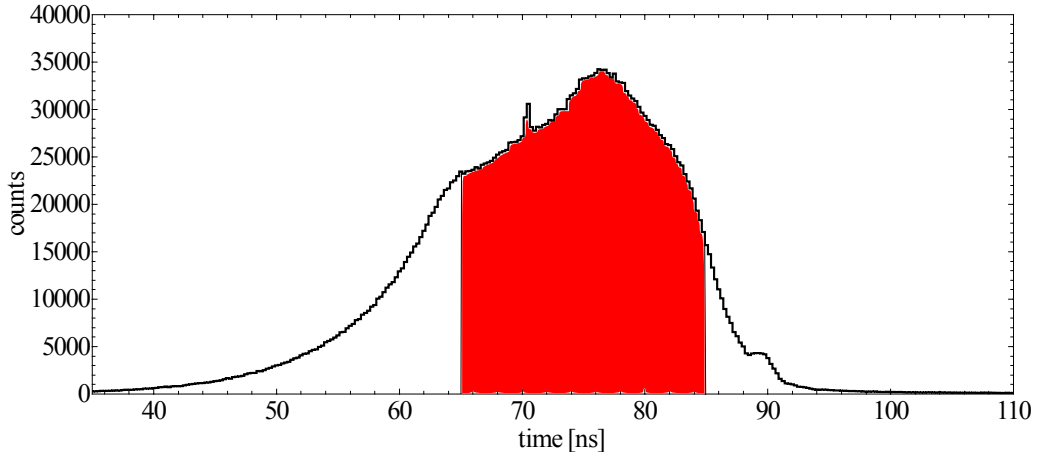


Figure 4.12: Time spectrum of HECTOR⁺. The red region is the time gate condition applied in the sort code.

The high-energy γ rays emitted in the CN decay were detected by the HECTOR⁺ array. The largest part of data was detected with a coincidence between HECTOR⁺ and AGATA Demonstrator. In order to reject background events, a gating condition on the time of the events was applied (see Fig.4.12).

It is important to note here that the time selection of this class of events is not exclusive enough to reject the neutron background. Nevertheless, since we verified the absence of neutrons in the ^{80}Zr (see Fig.4.5), we are sure to do not introduce a background with our time condition.

In Fig. 4.13 the γ -ray spectra detected in HECTOR⁺ are shown. In spite the time condition, in the high-energy part of the spectrum there is a strong background, which can be originated by N-N Bremsstrahlung or cosmic rays. This high-energy γ -rays can interact with the neighbouring material and the pair-production is the favourite reaction mechanism. Indeed, no γ -ray transitions were observed in AGATA Demonstrator in coincidence with $E_\gamma > 20\text{MeV}$ in HECTOR⁺, the only strong contribution seems to be the 511 keV peak (see Fig. 4.14).

In the E_γ - E_γ matrix of the energy detected in AGATA Demonstrator versus the energy detected in HECTOR⁺ (see the matrix in Fig.4.15), it is clearly visible a region ($E_\gamma \approx 18\text{MeV}$ in AGATA) due to the pre-amplifier saturation of the AGATA Demonstrator.

In addition, it is visible that many events were characterized by the coincidence be-

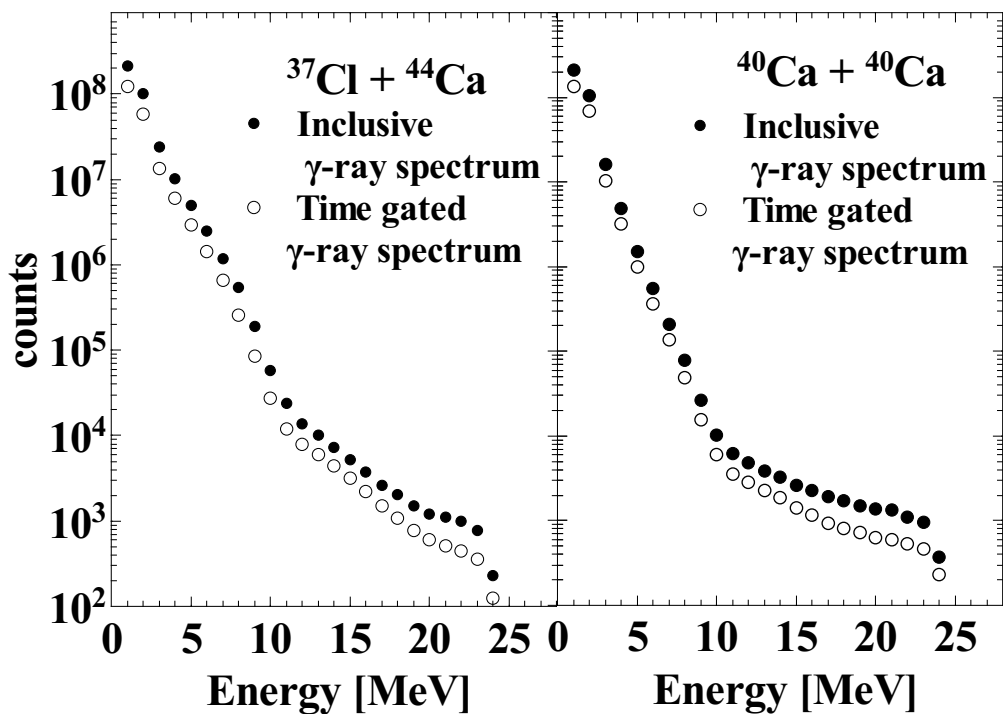


Figure 4.13: Comparison between the inclusive γ -ray spectra (filled dots) and the time gated γ -ray spectra (empty dots). The $^{37}\text{Cl} + ^{44}\text{Ca}$ spectra are plotted on the left, whereas the $^{40}\text{Ca} + ^{40}\text{Ca}$ spectra are plotted on the right.

tween two high-energy γ -rays.

In the CN decay, this kind of events are very unlucky, because, in general, only one high-energy γ -ray is emitted in the cooling process. Therefore, we considered these events as background, which must be subtracted.

As a proof of our considerations, in Fig.4.16 is shown the comparison between the HECTOR⁺ spectrum in coincidence with a high-energy γ -ray ($E_\gamma \geq 10\text{MeV}$) and a low-energy γ -ray ($E_\gamma \leq 4\text{MeV}$) detected in AGATA. As expected, the high-energy spectra in coincidence with another high-energy γ -ray exhibit a flat shape, on the other hand the other spectra exhibit a change in the slope at $\sim 10\text{ MeV}$, typical of the presence of the Giant Dipole Resonance. Moreover, the background spectra of both reactions are very similar, as shown in the left panel of Fig.4.16, and this is an additional proof that these events are independent by the reactions and no physical information is present in these data.

Since the background contribution in the high-energy part of the spectrum is the

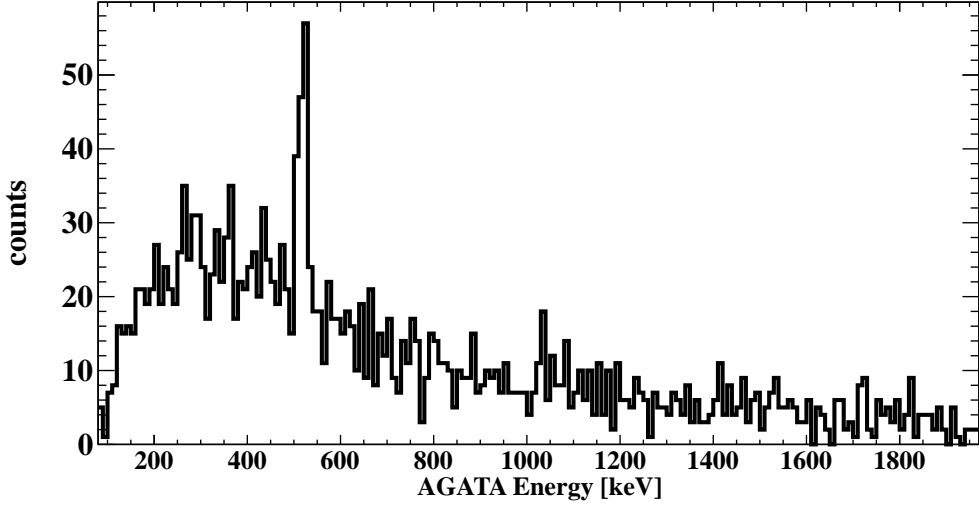


Figure 4.14: Low-energy spectrum of AGATA Demonstrator in coincidence with a high-energy γ ray ($E_\gamma \geq 20 \text{ MeV}$) detected in HECTOR⁺. No residue transitions are visible and only the 511 keV peak is present.

same for both reactions, the average of the spectra obtained in coincidence with a high-energy γ ray detected in AGATA was taken as the best parametrization of the background and a linear function was used to fit the data (see Fig.4.17). The spectra obtained after a background subtraction are shown in Fig.4.18 with empty dots and the typical GDR shape is clearly visible in the region between 10 MeV and 20 MeV.

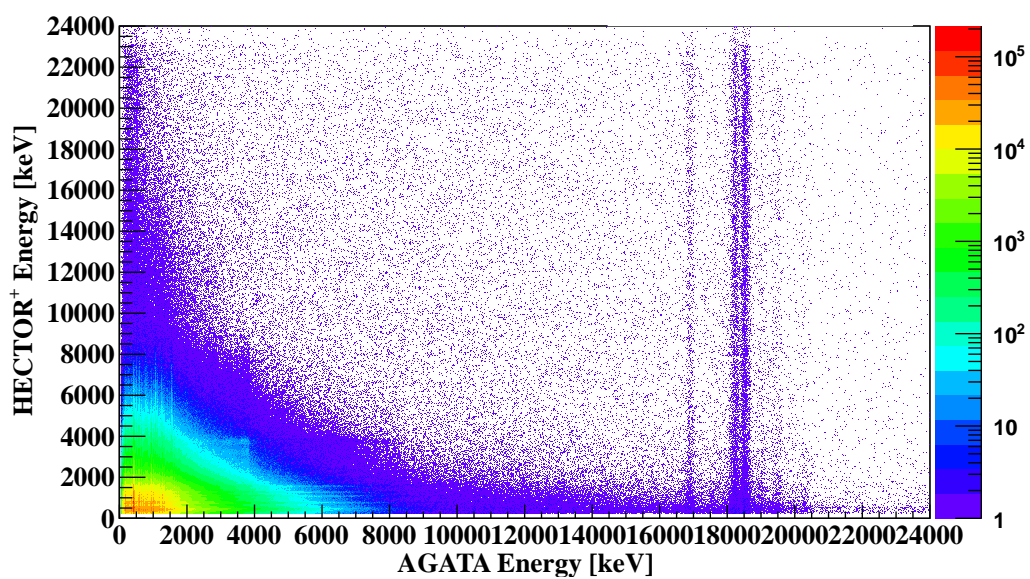


Figure 4.15: E_γ - E_γ matrix for the reaction $^{40}\text{Ca} + ^{40}\text{Ca}$. In the x-axis the energy detected in AGATA is plotted, whereas in the y-axis the energy detected in HECTOR⁺ is plotted.

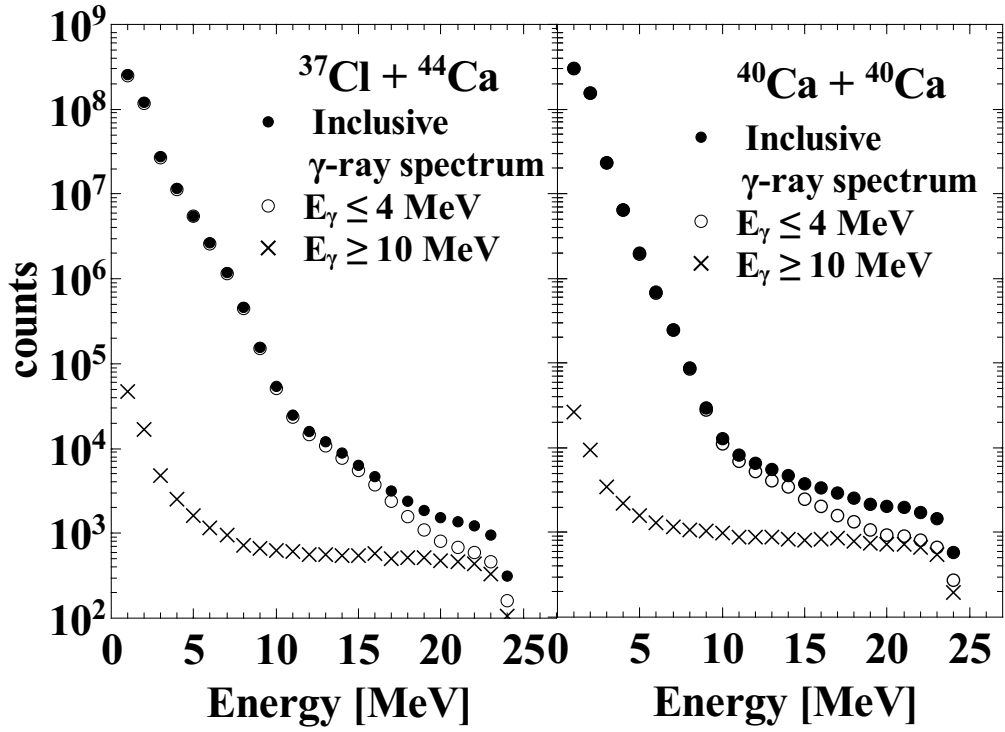


Figure 4.16: Comparison between the inclusive γ -ray spectra (filled dots) and the γ -ray spectra obtained with two conditions: $E_\gamma < 4$ MeV γ ray detected in AGATA (empty dots), $E_\gamma > 10$ MeV γ ray detected in AGATA (crosses).

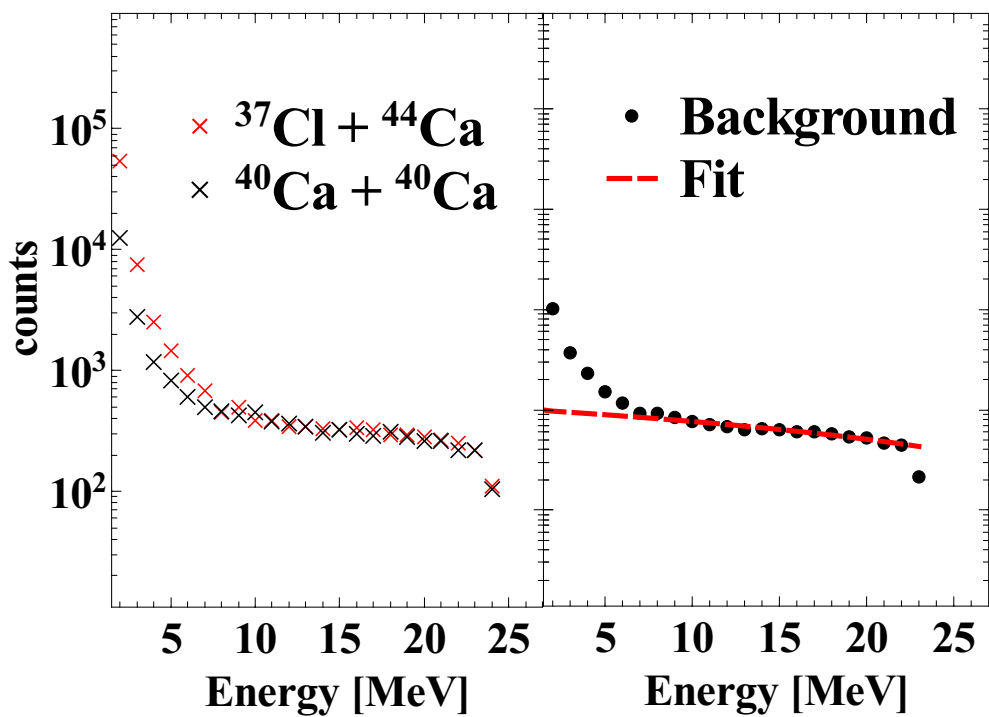


Figure 4.17: On the left: Background spectrum of $^{40}\text{Ca} + ^{40}\text{Ca}$ reaction (black crosses) and $^{37}\text{Cl} + ^{44}\text{Ca}$ (red crosses) obtained using a high-energy gate condition in AGATA as explained in the text. On the right: average spectrum of the background and the linear fit (red dashed line).

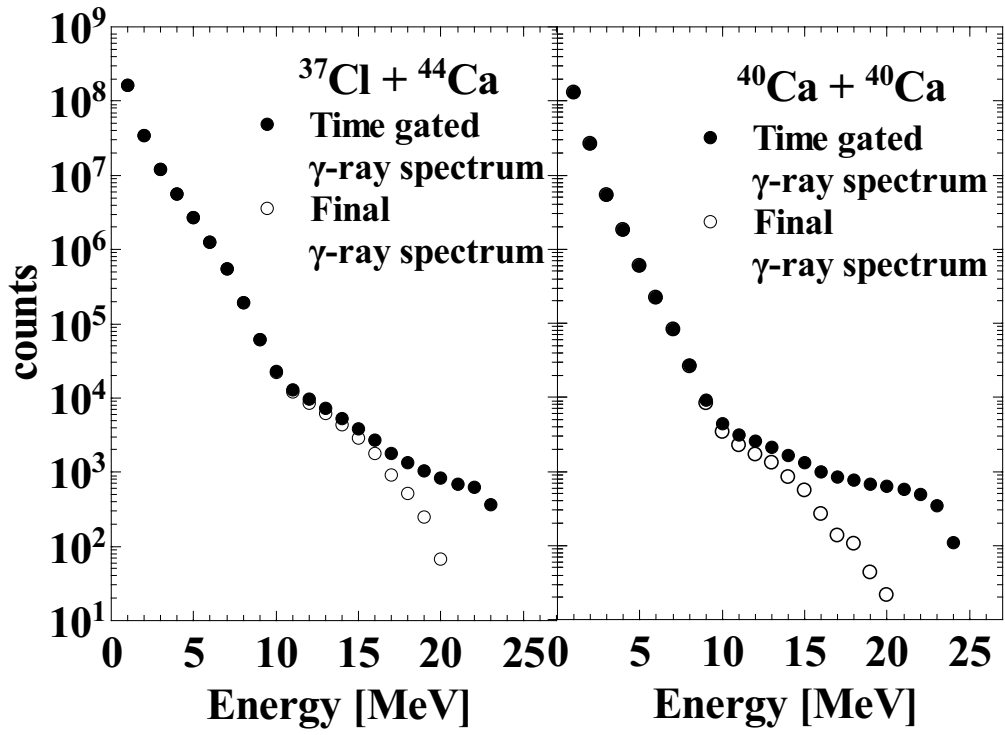


Figure 4.18: Comparison between the time gated γ -ray spectra (filled dots) and the γ -ray spectra after the background subtraction (empty dots).

In this chapter is reported the statistical model analysis of the γ -ray spectra detected with HECTOR⁺. The analysis of the spectrum of ^{81}Rb provided the GDR parameters, while the analysis of ^{80}Zr provided the value of the isospin mixing probability.

As already discussed, the AGATA coincidence spectra were used to validate the statistical model calculations, not to extract the high-energy γ -ray spectra.

The temperature dependence of the isospin mixing was obtained and the zero-temperature value deduced using the theoretical parametrisation reported in Ref. [52].

The isospin-symmetry-breaking correction δ_C used for the Fermi super-allowed transitions was extracted using the result of the present analysis.

All these results were published in Ref. [102].

5.1 Isospin in the statistical model

The statistical model analysis was performed using the CASCADE code [100, 101] in which the isospin formalism was included, in order to be sensitive to the isospin mixing effect. The original version of the CASCADE code was modified first by M.N. Harakeh and later on by the Washington University group, according to the formalism of Harney, Ritch, Weidenmuller reported in Ref. [61].

Three features are relevant for including the isospin in the statistical model:

- The population cross section matrices and level densities are labelled with the quantum number for isospin (in addition to excitation energy, angular momentum and parity).
- The states with different isospin are mixed before any type of decay (according to the CN hypothesis).

- The transmission coefficients are multiplied by isospin Clebsch-Gordan coefficients

In the statistical model two classes of isospin are considered: $I_< = I_z$ and $I_> = I_z + 1$. The initial compound nucleus is populated in the state $I_< = I_z$ according to the isospin conservation in nuclear reactions. States with $I > I_z$ correspond to configurations with a lower binding energy and, therefore, a higher excitation energy.

To calculate the isospin dependence of the level density, we equate the $I_>$ level density with the total level density of the isobaric analogue nucleus, shifted appropriately to the energy of the $I_>$ state in the parent nucleus (see Ref. [70] for a clear dissertation of the problem). Therefore, the energy of the $I_>$ state is calculated as the energy of the equivalent state in the isobaric analogue nucleus with the same mass A but $Z = Z-1$ and $N = N+1$, using the formula [48]:

$$\Delta_{I_<, I_>} = M(A_{Analog}) - M(A) + \Delta E_C - (m_n - m_p) \quad (5.1)$$

where ΔE_C is the difference due to the Coulomb energy, while the quantity $(m_n - m_p)$ takes into account the difference in mass between neutrons and protons. In the case of ^{80}Zr $\Delta_{I_<, I_>}$ is equal to 5.4 MeV. The level density ρ is calculated as:

$$\rho(E^*, J) = \frac{2J+1}{12\Theta^{3/2}(U+T)^2} \sqrt{a} e^{2\sqrt{a}U} \quad (5.2)$$

where Θ is the moment of inertia, T is the temperature, U is the internal energy of the system and a is the level density parameter. In the statistical model the internal energy U for the state $I_<$ is calculated as $U = E^* - E_{rot} - E_{GDR} = aT^2$, while for the state $I_<$ is calculated as $U = E^* - E_{rot} - E_{GDR} - \Delta_{I_<, I_>}$. This means that $\rho(I_>) < \rho(I_<)$. The level-density parameter a was chosen equal to $a = A/8$. It is important to note that in the calculation of U we subtracts also the GDR energy contribution.

The use of the statistical model to reproduce measured γ -ray spectra allows to extract the values of the Coulomb spreading width, $\Gamma_{\gtrless}^{\downarrow}$, and the isospin mixing, α_{\gtrless}^2 for both states.

5.2 Data analysis

The statistical model provides the γ -ray spectrum of the CN, which was compared (after the folding with the detector response function and normalizing to the data at around 5 MeV) with the experimental data. The GDR parameters were derived from the best fit to the data in the region between 8 and 15 MeV. Because of the exponential nature of the

spectra, the standard χ^2 is not a suitable quantity because of its weak sensitivity to the low yield part of the spectrum. For this reason, the fit minimization was applied to a Figure Of Merit (FOM) defined as:

$$FOM = \sum_{E=8MeV}^{E=15MeV} \frac{(Y_i - M_i)^2}{Y_i^2} \quad (5.3)$$

where Y_i and M_i are the experimental and simulated counts per bin respectively. Eq. 5.3 was obtained dividing the standard χ^2 over the number of counts for each bin. In this way, the sensitivity to the low yield part of the spectrum is increased.

The statistical errors were calculated performing a Monte-Carlo simulation: 10^4 spectra were created adding to the number of the experimental counts a fluctuation randomly extracted from a Gaussian distribution centred at zero and with a standard deviation equal to the statistical error on the number of counts per bin ($\sigma = \sqrt{Y_i}$). For each spectrum the best fitting parameter (obtained from the minimum of the FOM) was extracted. The 10^4 parameter values are distributed following a Gaussian. The statistical error of the parameter values is taken as the standard deviation of the Gaussian distribution. This procedure was used for the analysis of ^{81}Rb .

The error in the isospin mixing value has two sources of errors:

- The first comes from the propagation of the GDR parameter errors in ^{81}Rb .
- The second comes from the statistical fluctuations of the experimental data as in the case of ^{81}Rb .

We decided to take the sum of the square deviations as the best estimation of the error.

5.3 Fit results

For ^{81}Rb the best-fitting values of the centroid, width and strength of GDR were found to be: $E_{GDR} = 16.4 \pm 0.2 \text{ MeV}$, $\Gamma_{GDR} = 7.0 \pm 0.2 \text{ MeV}$ and $S_{GDR} = 90 \pm 5 \%$, as summarized in Table 5.1. The data and the corresponding statistical model calculations are shown in the left top panel of Fig.5.2; in the right top panel of the same figure the Γ_{GDR} FOM is plotted.

To extract the isospin mixing in ^{80}Zr the Coulomb spreading width was treated as the only free parameter to fit the ^{80}Zr data. The best fit of the ^{80}Zr data was obtained when the Coulomb spreading width is equal to $\Gamma_{>}^{\downarrow} = 12 \pm 3 \text{ keV}$. The plot of the corresponding

CN	E_{GDR} [MeV]	Γ_{GDR} [MeV]	S_{GDR} [%]	Γ^\downarrow [keV]
^{81}Rb	16.4 ± 0.2	7.0 ± 0.2	90 ± 5	-
^{80}Zr	16.4	7.0	90	12 ± 3

Table 5.1: Best fitting values are reported for both CN. For the statistical model analysis of the spectrum associated to ^{80}Zr the isospin mixing plays a role while all the other parameters were fixed from the ^{81}Rb analysis.

FOM is shown in the bottom-right panel of Fig. 5.2. The statistical error coming from the statistical fluctuation of the experimental data was estimated equal to 2 keV, using the same procedure of ^{81}Rb . Moreover the propagation of the ^{81}Rb GDR parameters uncertainty was estimated equal to 2 keV. Therefore, the total error in the value of the Coulomb spreading width is of the order of 3 keV. In Fig.5.1 the Γ^\downarrow best-fitting distribution is shown as example.

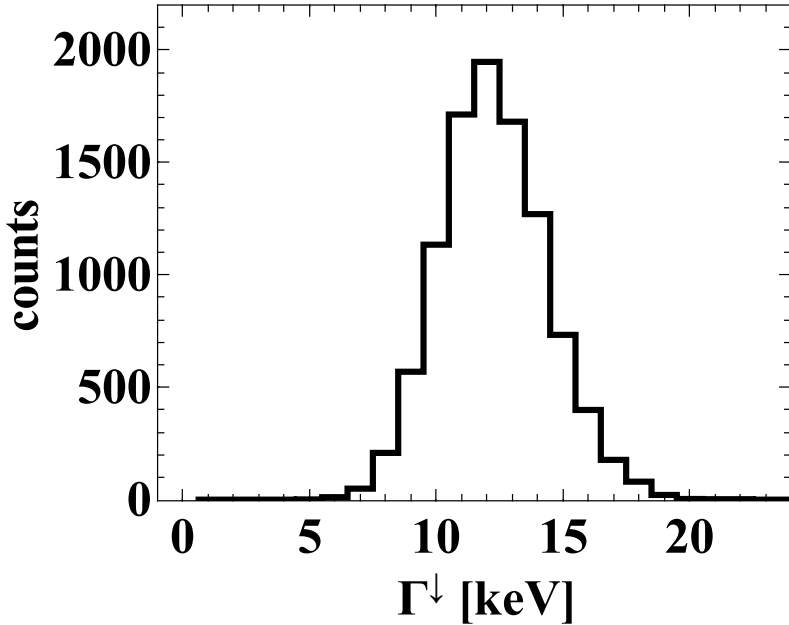


Figure 5.1: Γ^\downarrow distribution obtained from the fit procedure of the simulated 10^4 spectra, as explained in the text. the standard deviation represents the statistical error (≈ 2 keV).

It is worth to be noted that the fitting procedure is sensitive mainly in the 10-17 MeV region of the spectrum (where the GDR strength is concentrated). Indeed (see e.g. Ref. [26]) the gamma yield in region below 9 MeV is mainly originated by the emission in the

final steps of the de-excitation process after neutron, proton evaporation. The CN is not in a $I = 0$ state after the neutron, proton evaporation and thus it has lost the sensitivity to the isospin mixing. Only the first step of the GDR γ decay, before proton and neutron emission, is sensitive to the selection rule for E1 decay.

In order to emphasize the GDR region, the experimental and simulated data were divided by an exponential curve, obtaining a linearized spectrum. The exponential curves of both CN were obtained performing a statistical model calculation with a constant $B(E1)$ (i.e. no GDR strength). This procedure allows to see clearly the effect of the isospin mixing in the GDR region. In Fig.5.3 calculations were also made assuming full mixing (the dashed blue line) and no mixing (the green dashed line).

As explained before, the fit procedure of the ^{80}Zr data was made fixing the GDR parameters and varying only the isospin mixing contribution. Obviously, in this analysis, the presence of the isospin mixing was assumed. To be noted that the ^{80}Zr experimental data could be well reproduced by the statistical model also without the isospin mixing contribution, using a smaller GDR width. Indeed, if in the fit procedure the Γ^\downarrow is fixed to 0, the fit procedure converges at $\Gamma_{GDR} = 5.8$ MeV (see Fig. 5.4). Although the ^{80}Zr data are well reproduced, the GDR width is completely different than the value obtained in ^{81}Rb . This is an indirect proof of the presence of the isospin mixing effect in ^{80}Zr data.

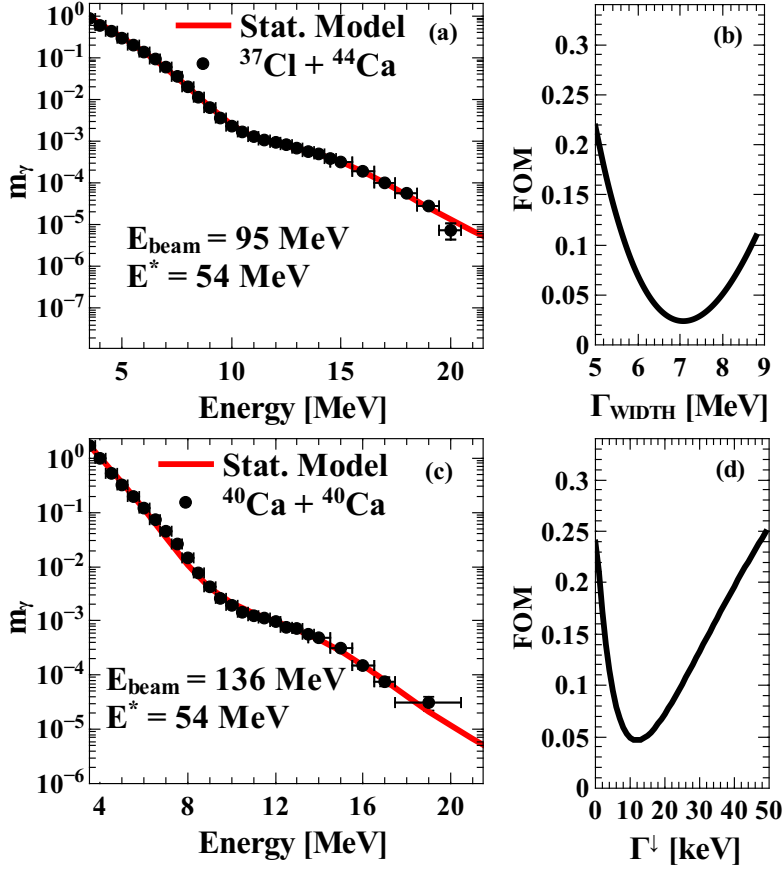


Figure 5.2: Left panel: high energy γ -ray spectra for the reactions $^{37}\text{Cl} + ^{44}\text{Ca}$ (a) and $^{40}\text{Ca} + ^{40}\text{Ca}$ (c). The data, measured with LaBr₃:Ce detectors, are shown with full circles in comparison with the best fitting statistical model calculations (red lines). Right panels: Figure Of Merit (FOM) obtained by varying the GDR width for $^{37}\text{Cl} + ^{44}\text{Ca}$ (b) and by varying the Coulomb spreading width for $^{40}\text{Ca} + ^{40}\text{Ca}$ (d). The FOM is the χ^2 value divided by the number of counts. Taken from Ref. [102].

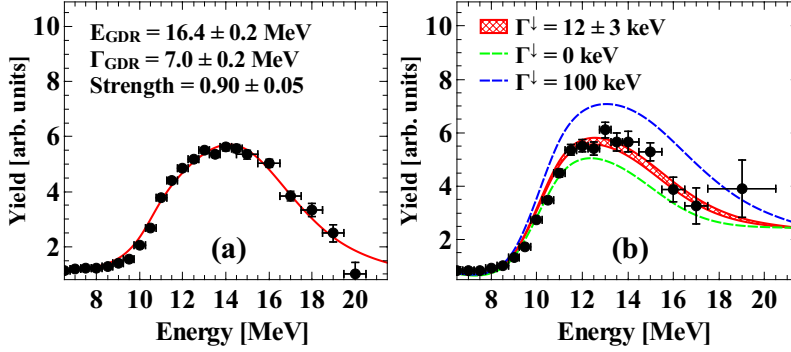


Figure 5.3: Linearized measured and calculated γ -ray spectra for $^{37}\text{Cl} + ^{44}\text{Ca}$ (a) and for $^{40}\text{Ca} + ^{40}\text{Ca}$ (b) in the GDR region. In (b) the statistical model calculations are shown corresponding to different values of the Coulomb spreading width: $\Gamma_{\text{C}}^{\downarrow} = 12$ keV (red line), for no mixing $\Gamma_{\text{C}}^{\downarrow} = 0$ keV (green dashed line), and for full mixing $\Gamma_{\text{C}}^{\downarrow} = 100$ keV (blue dashed line). Taken from Ref. [102].

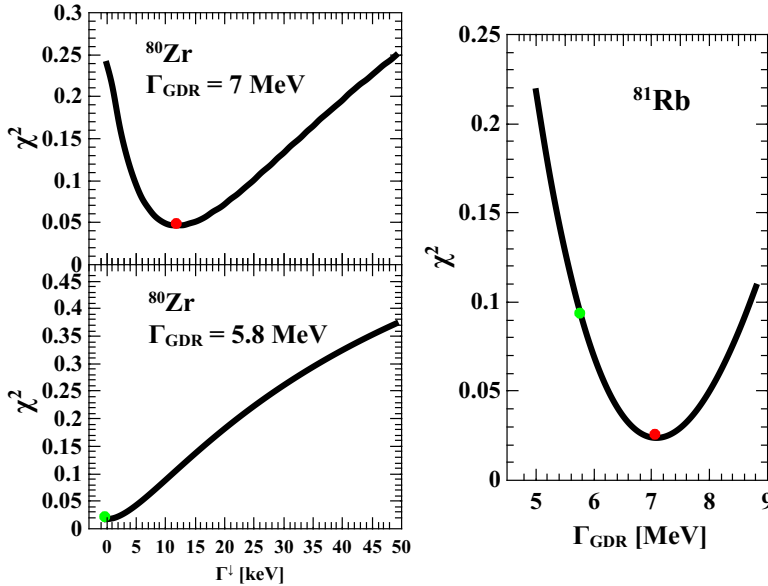


Figure 5.4: In the left panel, the FOMs correspond to the fitting procedure with isospin mixing (top panel) and without it (bottom panel). The minimum of the FOMs is signed with a red and green dots respectively. In the right panel, the FOM minimum for ^{81}Rb Γ_{GDR} (green dot) is clearly in disagreement with the GDR width of ^{80}Zr obtained without mixing (red dot).

5.4 Coulomb spreading width Γ^\downarrow in ^{80}Zr

The statistical analysis of the ^{80}Zr allowed to extract the value of the Coulomb spreading width. The value found was $\Gamma^\downarrow = 12 \pm 3$ keV. This value is in good agreement with that found by A. Corsi $\Gamma^\downarrow = 10 \pm 3$ keV. It means that the Coulomb spreading width is an intrinsic property of the system and it does not depend on its excitation energy.

In addition, our value is consistent with that found in the ^{80}Se studying the width of the IAS $\Gamma^\downarrow_{IAS} = 9.9 \pm 1.6$ keV [57]. This result supports the idea that the Coulomb spreading width of the CN and the IAS are the same quantities because they are originated by the isospin mixing.

In the Fig.5.5, our value of Γ^\downarrow is compared with the values available in literature. Our datum (blue diamond) is in good agreement with the experimental trend: the Γ^\downarrow values increase with the mass of the nucleus. This trend can be caused by the increases of the Coulomb interaction effects in the nucleus.

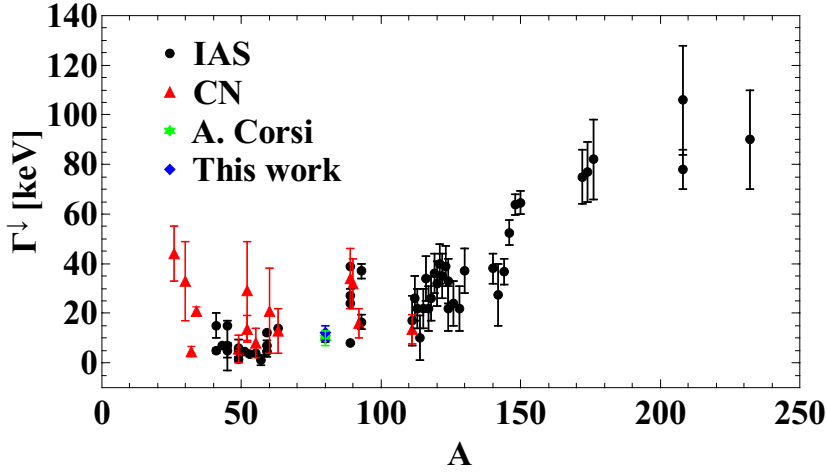


Figure 5.5: Values of the Coulomb spreading width obtained in the IAS (black dots) and in the CN (red triangle) [56,61]. The blue diamond is the value obtained in this work, while the green star is the value obtained in the Ref. [68].

5.5 Isospin mixing in ^{80}Zr at $T = 2 \text{ MeV}$

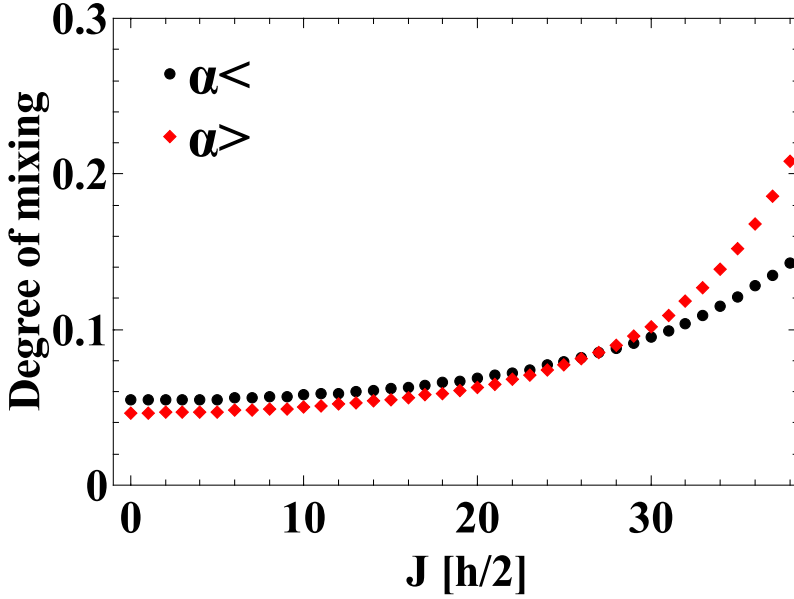


Figure 5.6: Degree of mixing $\alpha_{>}$ (red diamond) and $\alpha_{<}$ (black dots) along to the CN angular momentum.

In the statistical model the value of $\Gamma_{>}^{\downarrow}$ is kept fixed while the corresponding value is obtained using the detailed balance (Eq. 1.54). Using the values $\Gamma_{>}^{\downarrow}$, the statistical model provides as output the value of $\alpha_{>}^2(J)$ distribution. The spin dependence of the isospin mixing (see Fig.5.9) is due to the fact the internal energy of the system (and thus the nuclear temperature) depends on the rotational energy of the system. The increase of the degree of mixing along to J of the system, reflects the stronger effect of isospin-breaking interaction on colder and longer-lived CN. In order to obtain the average value $\langle \alpha_{>}^2 \rangle$, one has to weigh the $\alpha_{>}^2(J)$ values with the CN cross section and the γ -ray branching for each J . The mean values obtained were $\langle \alpha_{>}^2 \rangle = 8.5\% \pm 2\%$ and $\langle \alpha_{<}^2 \rangle = 8.0\% \pm 2\%$.

Our values are sensitively larger than those obtained by A. Corsi in Ref. [68] (see Table 5.2 for a comparison). The reason is that in this work we formed a nucleus at smaller internal energy and thus smaller(larger) decay width(lifetime). These differences can be viewed in Fig.5.7 where the lifetimes and the internal energies of the CN ^{80}Zr in both experiments are shown. This supports the concept that the mixing probability is a dynamical mechanism in the nucleus, governed by the lifetime of the system and thus it decreases with the excitation energy.

Ref.	$\langle U \rangle$ [MeV]	$\langle \Gamma_{CN}^\dagger \rangle$ [MeV]	$\langle \tau_{CN} \rangle$ [s]	$\langle \alpha_z^2 \rangle$
[68]	36	0.5	$1.4 \cdot 10^{-21}$	0.05 ± 0.01
This work	24	0.13	$5 \cdot 10^{-21}$	0.08 ± 0.02

Table 5.2: Comparison of the compound nucleus average features (internal energy $\langle U \rangle$, decay width $\langle \Gamma_{CN}^\dagger \rangle$ and lifetime $\langle \tau_{CN} \rangle$) between this work and Ref. [68]. The value of $\langle \alpha_z^2 \rangle$ is also reported in the last column.

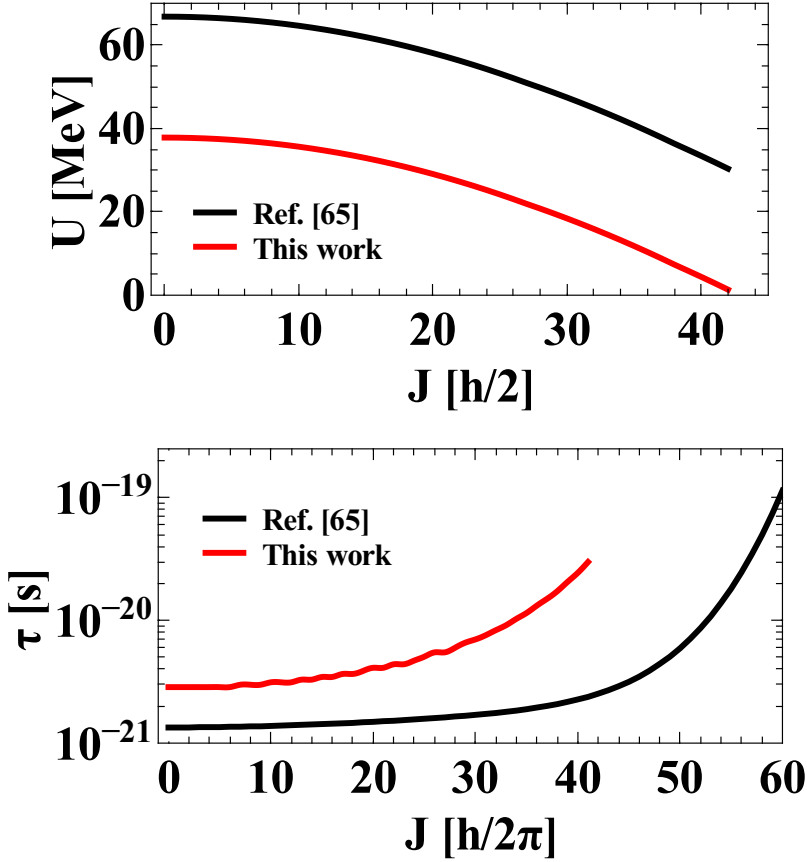


Figure 5.7: Top panel: internal energy of the compound nucleus ^{80}Zr in this experiment (red line) and in the experiment of Ref. [68] (red line). Bottom panel: lifetime of the compound nucleus in this experiment (red line) and in the experiment of Ref. [68] (black line).

In Fig.5.8 the value of $\langle \alpha_z^2 \rangle$ is plotted together with the available data present in literature obtained using the GDR γ decay technique.

All these data were analysed using the same statistical model approach. Although

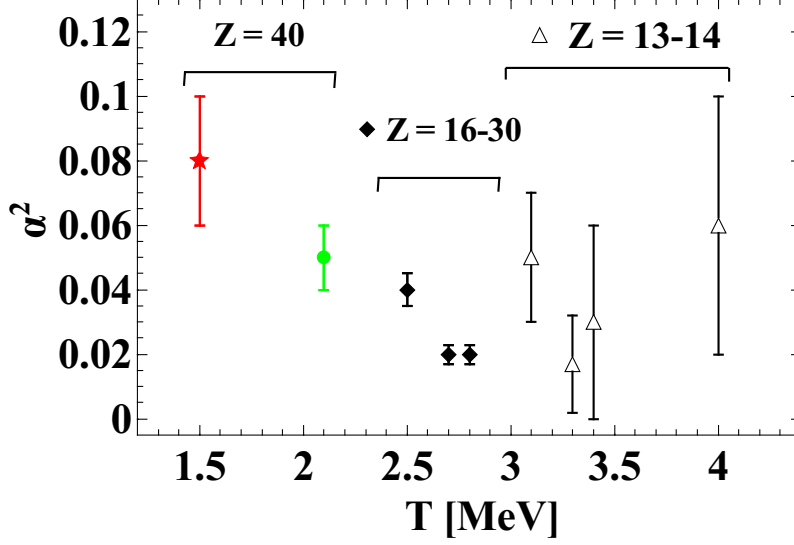


Figure 5.8: Comparison between $\alpha_{<}^2$ values obtained using the GDR γ decay. The red star is the value obtained in this analysis, the green dot is the value from Ref. [68], the black diamonds are the values from Ref. [66] and empty triangle are the value from Ref. [62]

the experimental data correspond to different nuclei (and some of them have large error bars), the experimental data exhibit the expected temperature dependence. This trend is a clear confirmation to the Wilkinson's hypothesis.

5.6 Isospin mixing in ^{80}Zr at $T = 0$

Using the γ decay of the GDR technique we extracted the value of isospin mixing at $T \approx 1.5$ MeV. However, since most of the theoretical calculations regard the isospin mixing in the ground state and its influence on nuclear structure, it is important to find a way to extrapolate the $T = 0$ value starting from the data at $T > 0$.

To compare the two data for ^{80}Zr at finite T with the predictions for the ground state, we used the model of Ref. [52], which describes the variation of the mixing probability with T . The isospin mixing probability for a nucleus at a finite temperature is defined as

$$\alpha_{>}^2(T) = \frac{1}{I_0 + 1} \frac{\Gamma_{\text{IAS}}^{\downarrow}}{\Gamma_{\text{CN}}(T) + \Gamma_{\text{IVM}}(\text{IAS})} \quad (5.4)$$

where $\Gamma_{\text{IAS}}^{\downarrow}$ is the Coulomb spreading width of the IAS, considered equal to $\Gamma_{>}^{\downarrow}$, $\Gamma_{\text{IVM}}(\text{IAS})$ is the width of the Isovector Monopole Resonance (IVM) at the excitation energy of the IAS, which is expected to be constant with T .

This model does not take into account the nuclear angular momentum and thus the effect of the rotational energy on the degree of mixing. Since the $\alpha_{>}^2$ depends on the angular momentum, we followed Ref. [68] and we expressed the degree of mixing at angular momentum $J = 0$ and we obtained a value of $\alpha_{>}^2 = 4.6\% \pm 0.7\%$. Neglecting the rotational energy the temperature of the system increases and $T(J=0) \approx 1.8$ MeV.

Using Eq. 5.4 it is possible to compare the experimental data with the theoretical ones. According to the systematic for the present case one has $\Gamma_{\text{IVM}}(\text{IAS}) = 240$ keV [51, 53]. $\Gamma_{\text{CN}}(T)$ is the CN decay width increasing with T .

In Fig. 5.9 the values of $\alpha_{>}^2$ calculated using Eq. 5.4 are shown as a function of T . The red line is obtained with a value of $\Gamma_{>}^{\downarrow} = 11.0 \pm 2.1$ keV, corresponding to the average of the two experimental values (the lower and upper curves corresponding to 8.9 and 13.1 keV, respectively).

This calculation gives at $T = 0$ $\alpha_{>}^2 = 4.6\% \pm 0.9\%$, in rather good agreement with the prediction in Ref. [49]. Following the discussion in Ref. [52], we also considered a weak linear dependence on T of the Coulomb spreading width given by $\Gamma_{>}^{\downarrow}(T) = \Gamma_{>0}^{\downarrow}(1 + cT)$. In this expression the chosen slope parameter $c = 0.1 \text{ MeV}^{-1}$ is such that the value of $\Gamma_{>}^{\downarrow}$ stays within the experimental error bar. The blue band in Fig. 5.9 displays the dependence of $\alpha_{>}^2$ with T when such weak dependence of $\Gamma_{>}^{\downarrow}$ is considered (the limiting curves correspond to $\Gamma_{>0}^{\downarrow} = 8.9$ and 13.1 keV).

We performed also two calculations using $\Gamma_{>}^{\downarrow} = 11.0$ keV and $\Gamma_{\text{IVM}}(\text{IAS}) = 220$ and 260 keV (see Fig. 5.10) and we found that these two curves are well within the two coloured bands of Fig. 5.9.

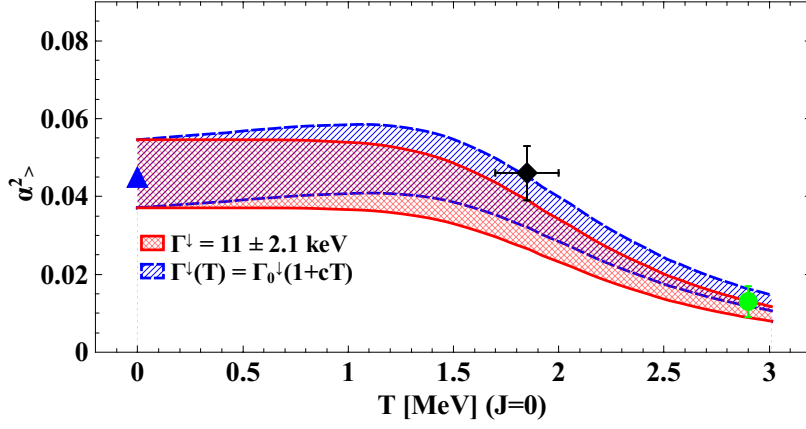


Figure 5.9: The isospin mixing $\alpha^2_{>}$ as a function of T obtained with the procedure of [52] corresponding to $\Gamma^\downarrow_{>} = 11.0 \pm 2.1$ keV (red region), constant with T . For the blue band $\Gamma^\downarrow_{>}$ was assumed to vary mildly and linearly with T . The blue triangle is the theoretical value at $T = 0$ from [49], the green circle is the datum from [68], the black diamond is the datum of this work. Taken from Ref. [102].

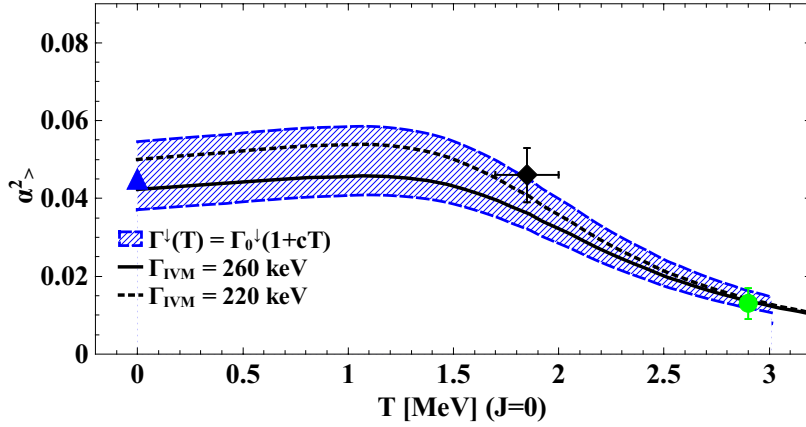


Figure 5.10: The isospin mixing $\alpha^2_{>}$ as a function of T obtained with $\Gamma_{IVM} = 220$ keV (blue band), $\Gamma_{IVM} = 240$ keV (dashed black line) and $\Gamma_{IVM} = 260$ keV (solid black line).

5.7 δ_C in ^{80}Zr

The value of the isospin mixing at $T = 0$ obtained in this analysis can be used to estimate the isospin mixing breaking correction term δ_C for the V_{ud} calculation. As already reported in Chapter 1, the δ_C is not a measurable quantity and its relation with the degree of mixing can be written as [76]:

$$\delta_C = 4(I + 1) \frac{V_1}{41\xi A^{2/3}} \alpha^2 \quad (5.5)$$

where $V_1 = 100$ MeV and $\xi = 3$, while α^2 is the isospin impurity in the ground state and I is the isospin of the nucleus. Using Eq. 5.5 the value $\delta_C = 0.81(16)\%$ was obtained for ^{80}Zr .

Usually the δ_C value is calculated using the β -decay ft value [72,73] or a very precise Q -value measurement (as in the case of ^{74}Rb [77]).

It is important to note that in these works these experimental values were obtained assuming that the ft value is constant and finding the best δ_C term which satisfies this assumption. On the other hand, in our case, we can give an experimental estimate of the δ_C starting from the physical observable which originates this phenomenon, i.e. the isospin mixing probability.

The value of δ_C obtained in this analysis is shown in the Fig. 5.11 in comparison with two different theoretical calculations from Ref. [72] and other experimental values of δ_C at lower Z obtained from β -decay [72] and mass measurement data [77]. The present result is consistent (within the error bars) with data for ^{74}Rb and the trend of predictions is also in agreement with the present new point. No calculations of the type of Ref. [72] are available for $A = 80$ and the δ_C data for ^{74}Rb are the only existing ones close to $N = Z = 40$.

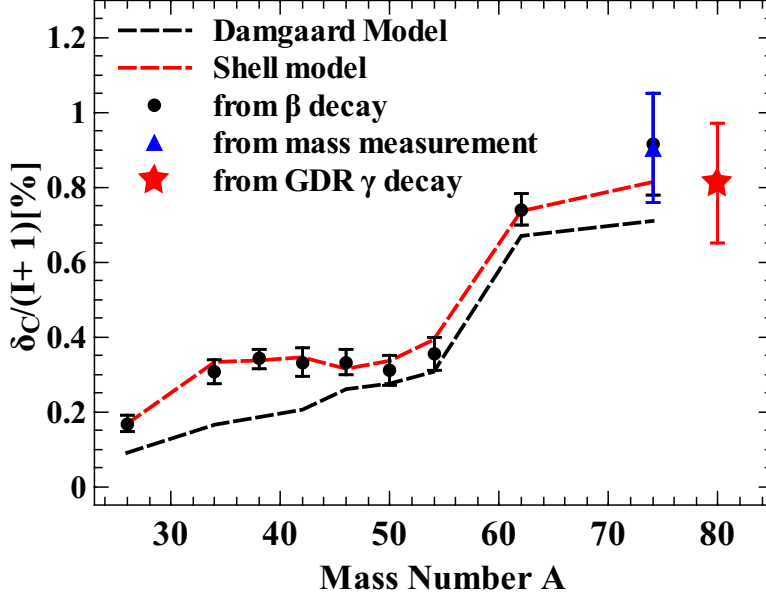


Figure 5.11: The isospin mixing correction δ_C as a function of the nuclear mass number A . The dashed black line is the prediction from the Damgaard model [78], while the red line is a shell model with Saxon-Woods radial wave function prediction [79]. Black circles are the experimental points extracted from β decay as reported in Ref. [72], the blue triangle is the value obtained from the mass measurement in Ref. [77]. The red star is the value of δ_C extracted in this work. It is plotted the quantity $\delta_C/I+1$ since β -decay measurements are for $I = 1$ nuclei, while that for ^{80}Zr is $I = 0$. Taken from Ref. [102].

Conclusions

In this thesis, we studied the GDR γ -decay in the CN ^{81}Rb and ^{80}Zr at $T \approx 2$ MeV. The statistical model analysis allowed to extract the ^{81}Rb GDR parameters and the isospin mixing probability in ^{80}Zr , which is the heaviest nucleus available using a fusion reaction with stable beam and target.

The comparison between our result and the values obtained with the same approach and for systems with $Z = 13-40$ at $T = 2-4$ MeV, allowed to test the temperature dependence of the degree of mixing, as suggested by Wilkinson. In particular the comparison with the value of A. Corsi [68] obtained in the same CN but with a larger excitation energy, show clearly the key role of the lifetime in this process.

In addition, in this analysis, we extracted the value of the Coulomb spreading width $\Gamma_{\gamma}^{\downarrow}$ which is in good agreement with that found by A. Corsi and the value obtained studying the IAS of ^{80}Se by Kailas [57]. This means that: i) the Coulomb spreading width is an intrinsic property of the nucleus and it does not depend on the excitation energy ii) The value obtained in the statistical analysis of the CN is the same of that obtained in the IAS, because it is originated by the same process.

Using our result and that obtained by A. Corsi, we studied the temperature dependence of the isospin mixing using the theoretical model reported in Ref. [52]. The value extrapolated at $T = 0$ is in good agreement with the theoretical calculation available in ^{80}Zr . This result suggests that using two or more experimental data at finite temperature is possible to deduce the value at $T = 0$.

This could open the way for a intense study of the isospin mixing in different mass region, with a systematic comparison between experimental and theoretical data, which

now is missing in literature.

In addition, The isospin-symmetry-breaking correction δ_C used for the Fermi super-allowed transitions was extracted in ^{80}Zr . No experimental or theoretical data are available for this nucleus. Nevertheless, our result is in good agreement with the theoretical and experimental mass-trend.

In conclusion, for the first time the T dependence of the isospin mixing was obtained for the ^{80}Zr nucleus, the heaviest that can be formed with stable nuclei. The T=0 value was deduced and provides a stringent test to theory. The isospin correction term used in the β -decay analysis was also extracted for the first time for A = 80 and found to be consistent with systematics from β -decay and mass measurements. This result supports the validity of the method based on the GDR at finite T to obtain isospin mixing in regions of Z not directly accessible at T = 0.

Part of the work reported in this thesis was published in the following papers:

S. Ceruti et al., "Isospin Mixing in ^{80}Zr : From Finite to Zero Temperature", Physical review letters 115 (22), 222502.

S. Ceruti et al., "Isospin mixing in ^{80}Zr at finite temperature", Acta Physica Polonica B 46 (3).

A. Bracco, S. Ceruti and L. Pellegrini, "Nuclear Structure aspects of gamma decay from giant resonances", EPJ Web of Conferences 78, 06002.

Bibliography

- [1] N. Bohr, Nature **137**, 344 (1936).
- [2] N. Bohr and F. Kalckar, Danske Vidensk. Selsk, Mat. Fys. Meddr. **14**, 10 (1937).
- [3] H. A. Bethe, Rev. Mod. Phys. **9**, 69 (1937).
- [4] V. F. Weisskopf, Phys. Rev. **52**, 295 (1937).
- [5] V. F. Weisskopf and P. H. Ewing, Phys. Rev. **57**, 472 (1940).
- [6] W. Hauser and H. Feshbach, Phys. Rev. **87**, 366 (1952).
- [7] H. Feshbach , A. K. Kerman and S. E. Koonin, Ann. Phys. **125**, 429 (1980).
- [8] C. Mahaux and H. A. Weidenmüller, Ann. Rev. Nucl. Sci. **29**, 246 (1979).
- [9] P. E. Hodgson, Rep. Prog. Phys. **50**, 1171 (1987).
- [10] R. J. Charity, Phys. Rev. C **82**, 014610 (2010).
- [11] P. F. Bortignon, A. Bracco and R. A. Broglia, Giant Resonances, Nuclear Structure at Finite Temperature, Contemporanay Concepts in Physics Volume 10, Harwood Academic Publisher (1998).
- [12] J. M. D'Auria et al., Phys. Rev. **174**, 1409 (1968).
- [13] P. Wong et al., Nucl. Phys. A **151**, 549 (1970).

- [14] E. Gadioli and P. E. Hodgson, *Pre-Equilibrium Nuclear Reactions*, Clarendon Press, Oxford (1992).
- [15] A. Corsi et al., *Phys. Lett. B* **679**, 197 (2009).
- [16] R. Bass, *Nuclear Reactions with Heavy Ions*, Springer-Verlag, 1980.
- [17] J. R. Grover and J. Gilat, *Phys. Rev.* **157**, 802 (1967).
- [18] M. N. Harakeh and A. van der Woude, *Giant Resonances, Fundamental High-Frequency Modes of Nuclear Excitation*, Oxford Science Publications, 2006.
- [19] M. Goldhaber, E. Teller, *Phys. Rev.* **74**, 1046 (1948).
- [20] H. Steinwedel and J. H. D. Jensen, *Z. Naturforsch.* **5a**, 413 (1950).
- [21] B. L. Berman and S. C. Fultz, *Rev. Mod. Phys.* **47**, 713 (1975).
- [22] P. Carlos et al., *Nucl. Phys.* **A219**, 61 (1974).
- [23] D. M. Brink, PhD Thesis, Oxford University (1955).
- [24] P. Axel, *Phys. Rev.* **126**, 671 (1962).
- [25] J. O. Newton et al., *Phys. Rev. Lett.* **46**, 1383 (1981).
- [26] J. J. Gaardhøje et al. *Phys. Lett. B* **139B**, 273 (1984).
- [27] J. J. Gaardhøje, *Ann. Rev. Nucl. Part. Sci.* **42**, 483 (1992).
- [28] K. Snover, *Ann. Rev. Nucl. Part. Sci.* **36**, 545 (1986).
- [29] A. Bracco et al., *Mod. Phys. Lett.* **A97**, 2479 (2007).
- [30] M. Mattiuzzi et al., *Nucl. Phys.* **A612**, 262 (1997).
- [31] D. Kusnezov et al., *Phys. Rev. Lett.* **81**, 542 (1998).
- [32] O. Wieland et al., *Phys. Rev. Lett.* **97**, 012501 (2006).
- [33] D. Kusnezov et al., *Phys. Rev. Lett.* **90**, 042501(4) (2003).
- [34] H. Hofmann et al. *Nucl. Phys.* **A571**, 301 (1994).
- [35] M. P. Kelly et al., *Phys. Rev. Lett.* **82**, 3404 (1999).
- [36] A. Schiller et al., *Nucl. Phys.* **A788**, 231c (2007).

- [37] W. Heisenberg, Z. Phys. **77**, 1 (1932).
- [38] E. Wigner, Phys. Rev. **51**, 106–119 (1937).
- [39] R. Machleidt, Phys. Rev. C **63**, 024001 (2001).
- [40] R. Machleidt and H. Mütter, Phys. Rev. C **63**, 034005 (2001).
- [41] F. Sammarruca, L. White, and B. Chen, Eur. Phys. J. **A48**, 181 (2012).
- [42] Sz. Borsanyi et al., Science **347**, 1452 (2015).
- [43] M. A. Bentley and S. M. Lenzi, Prog. Part. Nucl. Phys. **59**, 497 (2007).
- [44] D. D. Warner, M. A. Bentley and P. Van Isacker, Nature Physics **2**, 311–318 (2006).
- [45] R. Orlandi, Phys. Rev. Lett. **103**, 052501 (2009).
- [46] N. Auerbach, Phys. Rep. **98**, 273–341 (1983).
- [47] J. Ekman et al., Phys. Rev. C **70**, 057305 (2004).
- [48] D. H. Wilkinson, Isospin in Nuclear Physics, North-Holland Publishing Company (1969).
- [49] W. Satuła, J. Dobaczewski, W. Nazarewicz, and M. Rafalski, Phys. Rev. Lett. **103**, 012502 (2009).
- [50] W. Satuła, J. Dobaczewski, W. Nazarewicz, and M. Rafalski, Phys. Rev. C **81**, 054310 (2010).
- [51] T. Suzuki, H. Sagawa, and G. Colo, Phys. Rev. C **54**, 2954 (1996).
- [52] H. Sagawa, P. F. Bortignon, G. Colò, Phys. Lett. B **444**, 1 (1998) and private communication.
- [53] G. Colo, M. A. Nagarajan, P. Van Isacker, and A. Vitturi, Phys. Rev. C **52**, R1175 (1995).
- [54] I. Hamamoto and H. Sagawa, Phys. Rev. C **48**, R960 (1993).
- [55] J. Dobaczewski and I. Hamamoto, Phys. Lett. B **345**, 181 (1995).
- [56] J. Jänecke, M. N. Harakeh and S. Y. Van der Werf, Nucl. Phys. A **463**, 571 (1987).
- [57] S. Kailas et al., Nucl. Phys. A **315**, 157 (1979).

- [58] H. Orihara et al., Phys. Rev. Lett. **81**, 3607 (1998).
- [59] D. H. Wilkinson, Phil. Mag. **1**, 379 (1956).
- [60] H. Morinaga, Phys. Rev. **97**, 444 (1955).
- [61] H. L. Harney, A. Ritcher and H. A. Weidenmüller, Rev. Mod. Phys. **58**, 607 (1986).
- [62] J. A. Behr, PhD thesis, University of Washington, (1991).
- [63] E. Farnea et al., Phys. Lett. B **551**, 56 (2003).
- [64] J.A. Behr et al., Phys. Rev. Lett. **70**, 3201 (1993).
- [65] M. N. Harakeh et al., Phys. Lett. B **176**, 297 (1986).
- [66] M. Kicińska-Habior et al., Nucl. Phys. A **731**, 138 (2004).
- [67] E. Kuhlmann, Phys. Rev. C **20**, 415 (1979).
- [68] A. Corsi et al., Phys. Rev. C. **84**, 041304(R) (2011).
- [69] N. Severijns et al., Phys. Rev. C. **71**, 064310 (2005).
- [70] A. S. Jensen, Phys. Lett. B **68**, 105 (1977).
- [71] N. Cabibbo, Phys. Rev. Lett. **10**, 531 (1963).
- [72] I. S. Towner and J.C. Hardy, Phys. Rev. C. **82**, 065501 (2010).
- [73] I.S. Towner and J.C. Hardy, Phys. Rev. C. **77**, 025501 (2008).
- [74] H. Sagawa, Nguyen Van Giai and Toshio Suzuki, Phys. Rev. C **53**, 2163 (1996).
- [75] W. Satuła, J. Dobaczewski, W. Nazarewicz, and M. Rafalski, Phys. Rev. Lett. **106**, 132502 (2011).
- [76] N. Auerbach, Phys. Rev. C. **79**, 035502 (2009).
- [77] A. Kellerbauer et al., Phys. Rev. Lett. **93**, 072502 (2004).
- [78] J. Damgaard, Nucl. Phys. A **130**, 233 (1969).
- [79] I. S. Towner, J. C. Hardy, and M. Harvey, Nucl. Phys. A **284**, 269 (1977).
- [80] A. Gavron, Phys. Rev. C **21**, (1980) 230-236.

- [81] LISE++, <http://lise.nscl.msu.edu/lise.html>
- [82] A. Gadea et al., Nuclear Instruments and Methods in Physics Research A **654**, 88 (2011).
- [83] AGATA Collaboration, Nuclear Instruments and Methods in Physics Research A **668**, 26 (2012).
- [84] D. Bazzacco, Nuclear Physics A **746**, 248 (2004).
- [85] E. Farnea et al., Nuclear Instruments and Methods in Physics Research A **621**, 331 (2010).
- [86] N. Lalovic et al., Nuclear Instruments and Methods in Physics Research A **806**, 258 (2016).
- [87] J. Simpson, Zeitschrift für Physik A Hadrons and Nuclei **358**, 139 (1997).
- [88] A. Georgiev, W. Gast, and R. M. Lieder, IEEE Transactions on Nuclear Science **41**, no. 4, pp. 1116-1124 (1994).
- [89] F. C. L. Crespi et al., Nuclear Instruments and Methods in Physics Research A **705**, 47 (2013).
- [90] G. F. Knoll, Radiation Detection and Measurement, Fourth Edition, Wiley, 2010.
- [91] J. van der Marel and B. Cederwall, Nuclear Instruments and Methods in Physics Research A **437**, 538 (1999).
- [92] R. Nicolini et al., Nuclear Instruments and Methods in Physics Research A **582**, 554 (2007).
- [93] A. Giaz et al., Nuclear Instruments and Methods in Physics Research A **729**, 910 (2013).
- [94] X. Grave, R. Canedo, J.-F. Clavelin, S. Du, and E. Legay, Real Time Conference, 2005. 14th IEEE-NPSS, 2005.
- [95] <http://www.sparrowcorp.com/products/software>, "Kmax - Advanced Tools for Industry, Education and Research."
- [96] ROOT, A Data Analysis Framework, <http://root.cern.ch/drupal/>.
- [97] S. Agostinelli et al., Nucl. Instrum. Methods A **506**, 250 (2003).

- [98] A. Holm, unpublished, internal report NBI.
- [99] S. Lodetti, Bachelor thesis.
- [100] F. Pühlhofer, Nucl. Phys. A **280**, 267 (1977).
- [101] I. Diószegi, Phys. Rev. C **64**, 019801 (2001).
- [102] S. Ceruti et al., Physical Review Letters **115** (22), 222502.
- [103] A. Bohr and B. Mottelson, Nuclear Structure I. W.A. Benjamin, Inc., New York, (1969).